Laser cooling of an optomechanical crystal resonator to its quantum ground state of motion

Thesis by

Jasper Chan

In Partial Fulfillment of the Requirements

for the Degree of

Doctor of Philosophy

California Institute of Technology

Pasadena, California

2012

(Defended May 25, 2012)

In the pursuit of happiness.

Acknowledgments

To Mom and Dad, who never prescribed a future for me, and instead loved, encouraged, and supported me while I forged my own, thank you. To my sisters, thank you for putting up with me as a brother. 親愛的公公、婆婆、阿公、大伯父：多謝您們 的關懷和支持。

To my labmates/cohorts in the Painter group, Jeff Hill, Amir Safavi-Naeini, and Alex Krause, you have been constant companions and instrumental in all of my Science successes for the last several years. A science high five, for Science. Of course, to my irreplaceable Brazilian friend, Thiago Alegre, who regularly stayed up past his weirdly early bedtime taking cooling spectra with me and giving me a ride home afterwards, thank you for being so hilariously incoherent at two in the morning. The experiment would not have succeeded without you. Remember, *we are on the cavity now.* To my Viennese friend, Simon Gröblacher, thank you for the Christkindlmarkt group meeting experience. It was magical. To Matt Eichenfield, my mentor who started it all, thank you.

To Richard Li and Jimmy Hao, I could not ask for better friends and travel companions. I sorely needed those trips when I took them. WSA? To Kevin Mak, I could not have guessed how much we would accomplish together. To my roommate, Henry Kozachkov, thank you for the novel life experiences. See you on the playa. To my friends that I have not mentioned by name, thank you for filling my life with warmth and laughter, and for shaping me into who I am today.

And to Oskar Painter, thank you for showing me the way.

Abstract

Quantum mechanics continues to intrigue us with bizarre predictions that seemingly run counter to our everyday classical intuition. Superposition, zero-point motion, entanglement, and inescapable bounds on measurement precision are just a few purely quantum mechanical effects that come to mind. The promise of observing such effects in mesoscale mechanical resonators some orders of magnitude larger than the systems these effects had once been confined to, has resulted in surging interest in the field of cavity electro- and optomechanics. In these systems, the strong interaction of light and matter allows radiation pressure forces to provide significant damping to the mechanical motion, and serves as a means to mitigate the quantum-destroying, decohering effects of the pervasive thermal bath. However, for this backaction cooling to reduce the phonon occupation of a mechanical mode below unity, the confluence of the device and experimental setup must conform to a very strict set of conditions characterized by high optical and mechanical cavity quality factors, low optical absorption, low drive noise, and sufficiently sensitive detection.

In this work, we describe the first optomechanical device and all-optical experimental setup to simultaneously satisfy these conditions, realizing the quantum ground state cooling of a 3.7 GHz mechanical mode (final phonon occupation $\bar{n} = 0.85 \pm 0.08$) in a picogram and micron-scale patterned nanobeam structure from a bath temperature of approximately 20 K. In context, subunity occupation of a mechanical mode in a similar-sized object had previously only been achieved by electromechanical devices operating in millikelvin dilution refrigerator environments. We also discuss the numerical simulation efforts involved in designing and optimizing these novel, coupled optical and mechanical resonators, and the fabrication procedure to realize them in silicon microchips. We recognize that this cooling result represents only an initial step toward the complete optical control of mesoscale mechanical oscillators in the quantum regime. To this end, we summarize an experiment we performed to detect the quantum zero-point motion of a nanobeam via scattering sideband asymmetry. We further show work in improving the optomechanical coupling and quality factors of these devices, as well as devising more efficient coupling schemes to improve measurement sensitivity.

Contents

List of Figures

List of Tables

Chapter 1

Background

That light can exert a force—radiation pressure—is an idea typically thought to originate from Kepler in the 17th century as a natural consequence of the (ironically incorrect) corpuscular theory of light, and was supported by Newton as an explanation for the relative tilt of comet tails [1]. Later, Euler showed the existence of a repulsive force in the context of the longitudinal wave theory of light (credited to Huygens). Attempts to measure the strength of this force in the 18th century however, proved inconclusive [2]. The development of the unified theory of classical electromagnetism provided the correct basis for Maxwell to predict the existence of radiation pressure in 1873 [3], but the experimental proof by Crooke and his radiometer in the same year was later shown to be flawed and instead due to molecular scattering [4, 5]. Proper experimental verification for radiation pressure finally came in 1901, by Lebedev using a carefully calibrated torsion balance [6], with independent verification by Nichols and Hull in 1903 [7, 8]. With the rise of quantum mechanics in the 20th century, Saha published one of the first papers suggesting the quantization of light momentum in relation to radiation pressure [9], and was vindicated in 1923 by Compton's scattering experiments [10]. Circa 1970, Braginsky et al. noticed the increasing sensitivity of measurements made by coupled optical and mechanical (optomechanical) cavities. In a series of pioneering papers, he explored the radiation pressure effects of light confined to such optomechanical cavities, imposing limits to measurement sensitivity due to the quantization of light [11] and predicting that the finite cavity decay time would give rise to so-called dynamic backaction effects, leading to the amplification or damping of the mechanical oscillations [12]. This sparked a flurry of papers discussing radiation pressure forces in optomechanical cavities, such as its role as a quantum noise source in gravitational wave detection interferometers [13, 14], and experimental proposals for state squeezing [15, 16], quantum number nondemolition measurements [17, 18], and the generation of nonclassical states [19].

By the late 1990s, two forms of radiation pressure damping had been proposed as viable methods for bringing massive objects into the quantum regime: an active, feedback cooling scheme [20] operating on the principle of utilizing sensitive position measurements of the oscillator to effect

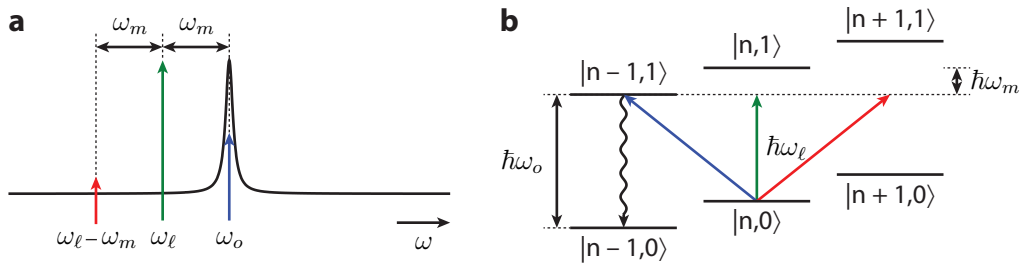

Figure 1.1: **Truncated level diagram for an optomechanical system.** **a**, Optical frequency response of the cavity, with the red-detuned pump beam at $\omega_\ell = \omega_o - \omega_m$ schematically shown as a green arrow, with mechanics induced scattering sidebands at $\omega_\ell \pm \omega_m$. The $\omega_\ell + \omega_m$ sideband is resonantly enhanced by the optical cavity. **b**, The corresponding energy level diagram for **a**. The kets, $|n, \ell\rangle$, represent a combined mechanical/optical state with m phonons and ℓ photons. The pump beam at $\omega_\ell = \omega_o - \omega_m$ drives a transition to the set of optical excited states, heavily favoring the $|n-1, 1\rangle$ state which decays to $|n-1, 0\rangle$ by the emission of a photon with energy $\hbar\omega_o$ (corresponding to the $\omega_\ell + \omega_m = \omega_o$ sideband in **a**), with the net effect of reducing the mechanical occupation by one. The converse, a net increase in mechanical occupation, is exceedingly unlikely.

real-time modifications of the oscillator motion, and a passive, "self" cooling scheme utilizing a red-detuned drive as originally proposed by Braginsky et al. In the latter, the radiation pressure force is enhanced by coupling the motion of a mechanical object to the light field in an optical cavity. Pumping of the optical cavity by a single-frequency electromagnetic source produces a coupling between the mechanical motion and the intensity of the electromagnetic field built up in the resonator. As the radiation pressure force exerted on the mechanical object is proportional to the field intensity in the resonator, a form of dynamical backaction results, which for a lower frequency (red) detuning of the laser from the cavity, leads to damping and cooling of the mechanical motion. This is easily understood with the energy level diagram in Figure 1.1, and is very similar to the successful technique used in atom and ion cooling [21]. Both schemes showed promise as a means to achieve quantum ground state cooling in optomechanical systems, defined as the reduction of the *average* mechanical mode occupation below unity, representing a ground state occupation probability of >50%.

The active scheme was demonstrated experimentally in 1999, showing a factor of 40 reduction in the effective temperature of a gram-scale Fabry-Perot cavity end mirror [22]. The passive scheme, the focus of this work, was demonstrated nearly simultaneously in 2006 by three different groups. From room temperature, both Arcizet et al. and Gigan et al. showed "self" cooling to an effective temperature of ∼10 K in a silicon micromirror [23, 24]. On the other hand, Schliesser et al. used instead a toroid cavity at room temperature and showed similar cooling to an effective temperature of 11 K [25], but with an average phonon occupation two orders of magnitude lower as a result of the higher mechanical mode frequency (∼60 MHz compared to <1 MHz).

The variety of physical realizations for optomechanical cavities can already be seen from these

early radiation pressure cooling experiments. Indeed, optomechanical cavities span the length–mass spectrum, from the kilometer–kilogram scale gravitational wave detector at LIGO [26] to diminutive nanometer–femtogram scale nanowire cavities [27]. However, despite their differences, they can be characterized using an identical set of rate parameters (expressed in angular units; to be explored in greater detail in the following chapter):

- ω_o and ω_m, respectively the optical and mechanical cavity resonance frequencies.
- κ, the total loss rate of the optical cavity (with related optical quality factor, $Q_o \equiv \kappa/\omega_o$).
- γ_i, the intrinsic loss rate of the mechanical cavity (with related intrinsic mechanical quality factor, $Q_m \equiv \gamma_i/\omega_m$), crucially representing the coupling rate to the thermal bath.
- g, the coupling rate between the optics and the mechanics (optomechanical coupling rate), physically representing the change in the optical cavity mode frequency resulting from the zero-point motion of the mechanical system. The amplitude of the zero-point motion is given by $x_{\mathrm{zpf}} = \sqrt{\hbar/2m_{\mathrm{eff}}\omega_m}$, where $\hbar = 1.054571726(47)\times10^{-34}$ J$\cdot$s is the reduced Planck constant [28] and m_{eff} is the effective motional mass of the mechanical resonator.

A significant amount of effort has been devoted to understanding the limits of the radiation pressure cooling schemes and the requirements for achieving quantum ground state cooling in relation to these rate parameters [29–33]. Most notably, the use of backaction (passive) cooling with the goal of reducing the mechanical mode occupation below the unity threshold *requires* operation in the so-called sideband-resolved regime, characterized by an optical loss rate much lower then the mechanical frequency of the system ($\kappa/4\omega_m < 1$). In the converse, sideband *un*resolved regime ($\kappa/4\omega_m > 1$), the rate of the off-resonance transition (red arrow in Figure 1.1) is sufficient to induce significant mode heating, rendering the quantum ground state of the mechanical mode beyond reach [29, 31, 32]. This is again very similar to atom and ion cooling [21, 34].

In the last several years, numerous experiments attempting to reach the quantum ground state via these radiation pressure cooling schemes have been performed, with their results summarized in Table 1.1. However, the first demonstration of a mesoscopic resonator in its ground state did not use radiation pressure cooling at all, but instead direct environmental cooling of a 6 GHz mechanical mode to millikelvin temperatures, resulting in a phonon occupation below 0.07 [48]. This was followed by the radiation pressure cooling of an electromechanical system to a phonon occupation of 0.34 ± 0.05 [51]. Within the optomechanics community however, the closest approach to the quantum regime in the mesoscale was a phonon occupation of 9 ± 1 in a microtoroid cavity [50]. In this work, we demonstrate the first all-optical quantum ground state cooling of a mechanical mode in a nanobeam-based optomechanical crystal, with a lowest achieved phonon occupation of 0.85 ± 0.08 [52]. This allows well-developed quantum optics techniques to be applied to manipulating the behavior of a

	T_b [K]	$\omega_m/2\pi$	Q_m	$\bar{n}_f$	Ref.
Cohadon et al. (1999)	300	1.86 MHz	40,000	8.2×10^5	[22]
Arcizet et al. (2006)	300	814 kHz	10,000	2.6×10^5	[23]
Gigan et al. (2006)	300	278 kHz	10,000	6×10^5	[24]
Schliesser et al. (2006)	300	57.8 MHz	2,890	4.0×10^3	[25]
Naik et al. (2006)	0.003	21.8 MHz	120,000	25	[35]
Kleckner and Bouwmeester (2006)	300	12.5 kHz	137,000	2.3×10^5	[36]
Corbitt et al. (2007)	300	2.2 kHz	3,200	8×10^6	[37]
Poggio et al. (2007)	2.2	2.6 kHz	–	2.3×10^4	[38]
Brown et al. (2007)	300	7 kHz	20,000	1.3×10^8	[39]
Gröblacher et al. (2008)	35	557 kHz	1,000	1×10^4	[40]
Schliesser et al. (2008)	300	73.5 MHz	30,000	5.2×10^3	[41]
Thompson et al. (2008)	300	134 kHz	1,100,000	1.1×10^3	[42]
Vinante et al. (2008)	4.2	914 Hz	880,000	4×10^3	[43]
Teufel et al. (2008)	0.05	1.5 MHz	300,000	140	[44]
Gröblacher et al. (2009)	5	945 kHz	30,000	32 ± 4	[45]
Schliesser et al. (2009)	1.65	65.3 MHz	2,600	63 ± 20	[46]
Park and Wang (2009)	1.4	99.2 MHz	3,700	37	[47]
O'Connell et al. (2010)	0.025	6.2 GHz	260	<0.07	[48]
Rocheleau et al. (2010)	0.146	6.3 MHz	1,000,000	3.8 ± 1.3	[49]
Riviére et al. (2011)	0.6	70 MHz	10,000	9 ± 1	[50]
Teufel et al. (2011)	0.015	10.6 MHz	330,000	0.34 ± 0.05	[51]
Chan et al. (2011)	**20**	**3.7 GHz**	**105,000**	$\mathbf{0.85 \pm 0.08}$	[52]
Verhagen et al. (2011)	0.65	78 MHz	22,000	1.7 ± 0.1	[53]

Table 1.1: **Radiation pressure cooling results.** Listed in chronological year order are the minimum achieved mechanical mode occupations, $\bar{n}_f$, in radiation pressure cooling experiments, along with the thermal bath temperature, T_b, mechanical mode frequency, ω_m, and the mechanical quality factor, Q_m. The results of this work are included and highlighted. While technically the work by O'Connell et al. did not utilize radiation pressure cooling, it is included for comparison.

picogram, micron-scale mechanical element quietly oscillating in its ground state, bringing about the long sought after transition from cavity optomechanics, to cavity *quantum* optomechanics.

For the interested reader, a more detailed overview of the development of quantum cavity optomechanics can be found in the excellent review papers [32, 54, 55].

1.1 Previous Work within the Painter Group

Before beginning the backaction cooling experiment, I worked extensively with Matt Eichenfield developing my numerical simulation knowledge and script library by helping design and optimize "zipper" double nanobeam cavities [56, 57]. This describes a pair of silicon nitride, doubly clamped, patterned nanobeam, linear optical cavities placed in the near field of each other, forming a supercavity sensitive to the differential motion of the beams (see Figure 1.2). The sensitivity scales exponentially with reducing slot gap between the nanobeams; the high contrast nitride–air–nitride interface in the gap significantly enhances the field intensity in the low-index region, resulting in large field gradients and drastically reduced mode volumes. On this platform we measured an

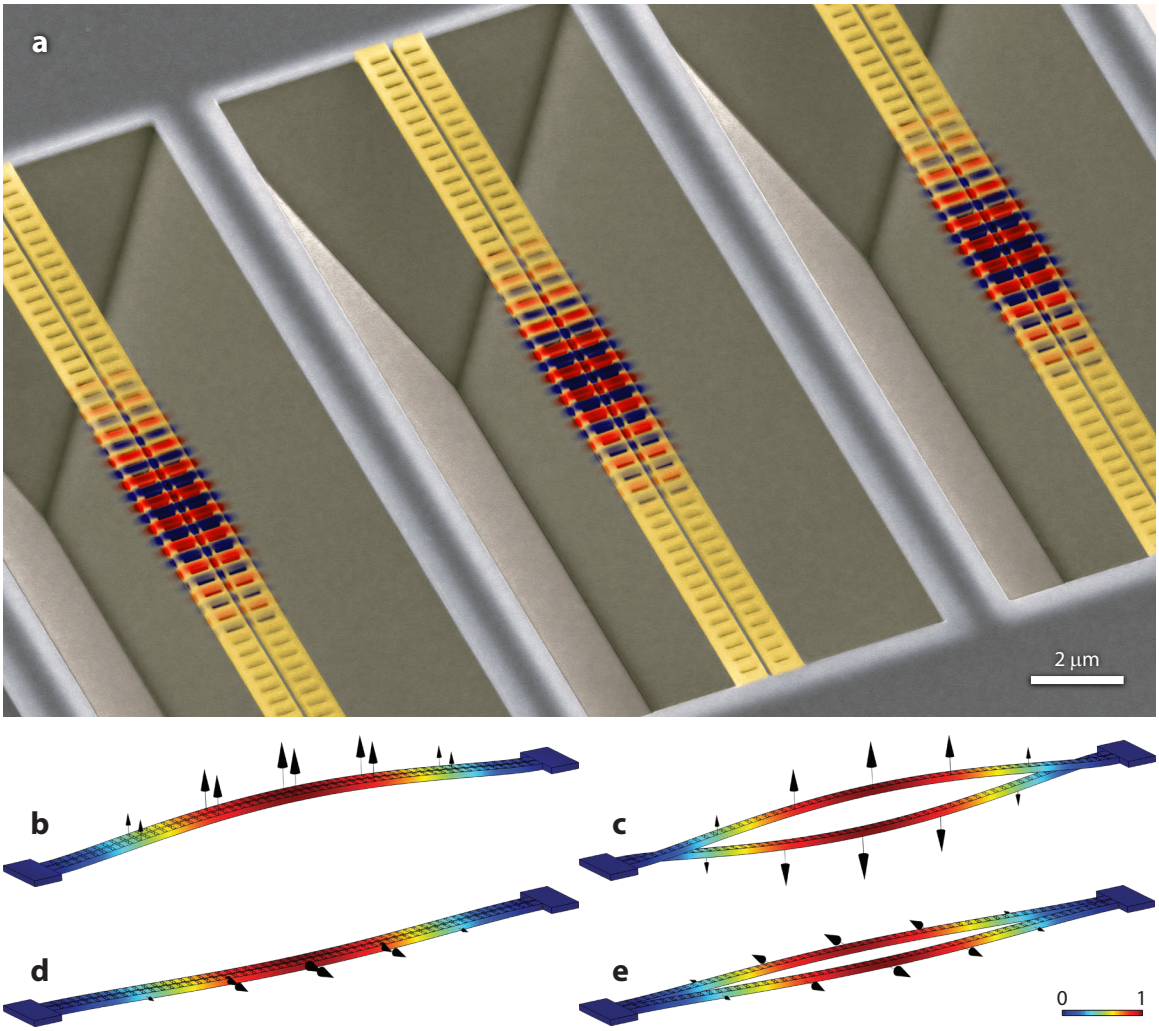

Figure 1.2: **"Zipper" double nanobeam cavities.** **a**, False-color scanning electron microscope (SEM) image of a fabricated zipper cavity with the transverse (to the long axis of the beam) electric field of the fundamental bonded optical mode superimposed (computed using finite element analysis, abbreviated FEM). The narrow slot between the two beams results in a large field concentration in the gap, leading to substantial field gradients and enhanced sensitivity to the motion of the beams. Below, FEM simulations of the fundamental double beam mechanical modes, represented by the normalized displacement field magnitude, $|\boldsymbol{Q}|/\max\{|\boldsymbol{Q}|\}$: **b**, the out-of-plane common mode, **c**, the out-of-plane differential mode, **d**, the in-plane common mode, and **e**, the in-plane differential mode (which we are most sensitive to as it directly modulated the slot gap).

optomechanical coupling rate (with respect to the slot gap) between the 8 MHz fundamental differential beam mode and the fundamental bonded optical mode of ∼600 kHz, with a corresponding photodetector-noise-limited displacement sensitivity of 5×10^{-17} m $\cdot$ Hz$^{-1/2}$. At high input powers (∼5 mW), we further observed a large optical stiffening effect, increasing the frequency of the mechanical mode to 19 MHz, representing a five-fold increase in the intrinsic mechanical stiffness of the beam. Double nanobeam designs have since been further refined for sensitive, large bandwidth force detection [58].

Following this, we began work on single silicon nanobeam optomechanical crystals [59, 60] (labeled G2 nanobeams for clarity; see Figure 1.3). These G2 nanobeams would eventually serve as the basis for the 5G and 5GHF nanobeam designs used in this work for quantum ground state cooling. Conceptually, optomechanical crystals originated in epitaxially grown vertical cavity structures [61], and utilize the principle of Bragg confinement for the simultaneous localization of the optical and mechanical mode to a small, optical wavelength scale volume, leading to enhanced light–matter interaction. Crucially for the prospects of quantum ground state cooling using the nanobeam optomechanical crystal platform, the realized frequencies of the optically coupled mechanical modes in G2 devices reached an upper limit of >2 GHz, entering the all-important sideband-resolved regime of operation ($\kappa/4\omega_m \approx 0.6$ for a fundamental optical mode with a quality factor of 38,000 coupled to a fundamental mechanical breathing mode at 2.2 GHz). In addition to spurring the development of the 5G and 5GHF devices, working on the G2 nanobeams further developed my numerical simulation knowledge to include phononic crystal design, and facilitated a gradual introduction to silicon fabrication, and optical and mechanical mode characterization.

Meanwhile, Safavi-Naeini et al. theorized and demonstrated a means to mitigate clamping losses in high-frequency mechanical modes of planar silicon structures, yielding improved mechanical quality factors [62, 63]. This concept, in conjunction with the device design knowledge from the double and single nanobeam experiments described above, produced large gains in the frequency–quality product ($f_m \cdot Q_m$) of the devices in this work; to $>10^{14}$ in the 5G design and to $>10^{15}$ in the 5GHF design.

Thus, my experiences, along with the availability of powerful numerical simulation tools [64, 65], the group's wealth of silicon fabrication experience [66, 67], and the ability to rapidly couple to, and characterize hundreds of devices via a dimpled fiber taper probe [68–70], provided a uniquely appropriate starting point for approaching the problem of quantum ground state cooling in cavity optomechanics.

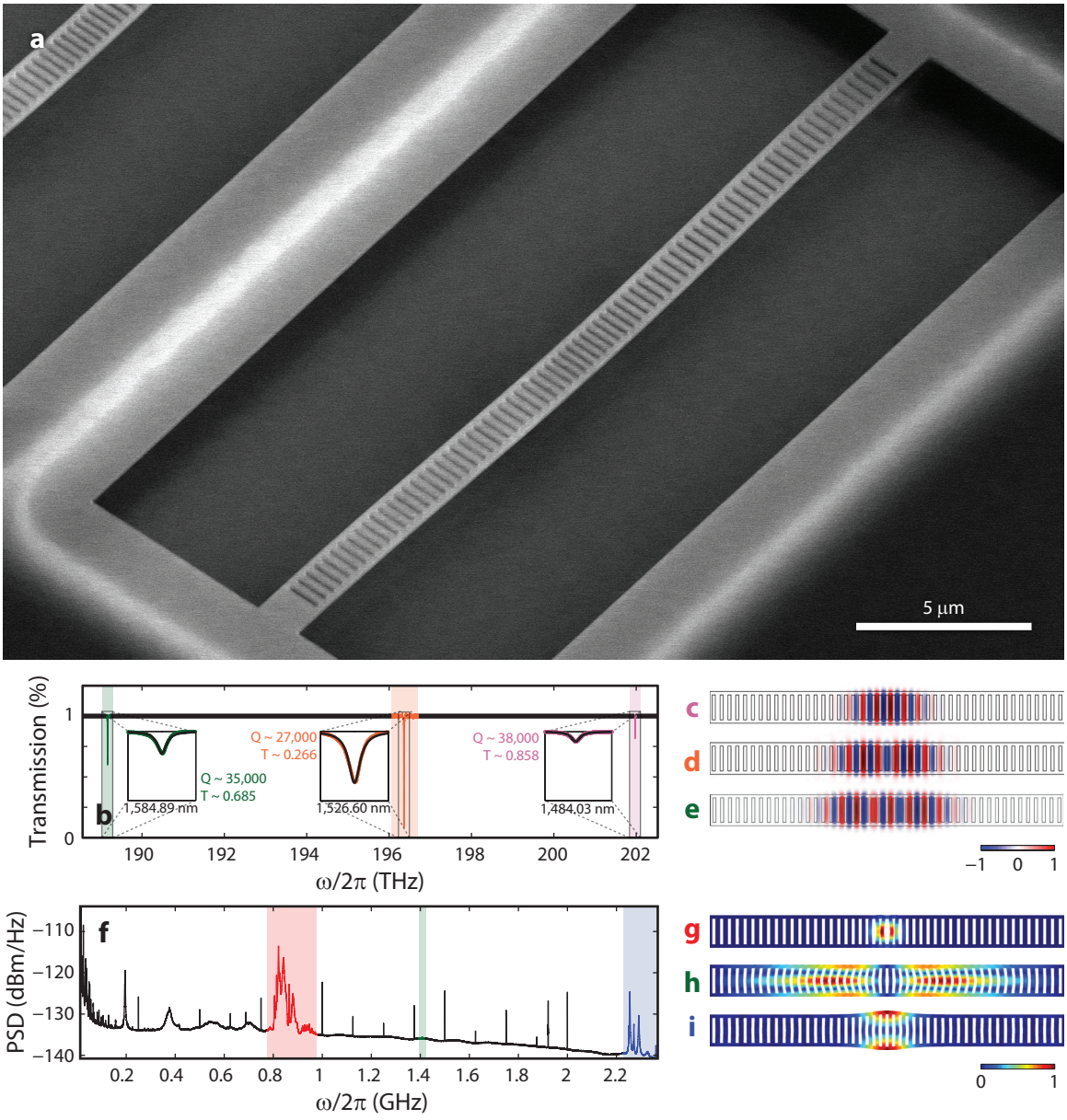

Figure 1.3: **Optomechanical nanobeam cavities.** **a**, SEM image of a fabricated optomechanical crystal cavity. The measured **b**, optical transmission response and **f**, power spectral density (PSD) of the mechanical fluctuations imprinted onto the optical signal (using a simplified version of the experimental setup in Figure 5.1). To the right are FEM simulations of the **c**, fundamental, **d**, 2nd order, and **e**, 3rd order optical modes (plotted as normalized transverse electric field amplitude), and the **g**, fundamental "pinch" mode, **h**, fundamental "accordion" mode, and **i**, fundamental breathing mode (plotted as normalized displacement field magnitude). Crucially, the ability to transduce high-frequency mechanical motion allows operation in the sideband-resolved regime of backaction cooling.

Chapter 2

Backaction Cooling Theory

An optomechanical system is canonically modeled as a Fabry-Perot cavity of length L_{eff} with one mirror fixed and the other mirror of mass m_{eff} mounted on a spring (Figure 2.1). We examine the dynamics of an optical cavity mode at frequency ω_o, coupled to the position of the mass-spring system oscillating at frequency ω_m. Modeling both modes as quantum simple harmonic oscillators with $\hat{a}$ ($\hat{a}^\dagger$) and $\hat{b}$ ($\hat{b}^\dagger$) respectively the annihilation (creation) operators of photons and phonons, the system Hamiltonian is simply

$$\hat{H}_{\text{sys}} = \hbar\omega_o \hat{a}^\dagger \hat{a} + \hbar\omega_m \hat{b}^\dagger \hat{b}. \tag{2.1}$$

The position operator of the mechanical quantum harmonic oscillator is

$$\hat{x} = x_{\text{zpf}}(\hat{b}^\dagger + \hat{b}), \tag{2.2}$$

where $x_{\text{zpf}} = \sqrt{\langle 0|\hat{x}^2|0\rangle} = \sqrt{\hbar/2m_{\text{eff}}\omega_m}$ is the zero-point fluctuation. A change in the position of the end mirror modifies the cavity length, shifting the optical cavity mode frequency by $\Delta\omega_o = \omega_o \hat{x}/L_{\text{eff}}$. We can generalize this to

$$\Delta\omega_o = \frac{\partial\omega_o}{\partial x}\hat{x}, \tag{2.3}$$

so the interaction Hamiltonian is

$$\hat{H}_{\text{int}} = \hbar\frac{\partial\omega_o}{\partial x} x_{\text{zpf}}(\hat{b}^\dagger + \hat{b})\hat{a}^\dagger\hat{a} \tag{2.4}$$

$$= \hbar g(\hat{b}^\dagger + \hat{b})\hat{a}^\dagger\hat{a}, \tag{2.5}$$

where

$$g = x_{\text{zpf}}\frac{\partial\omega_o}{\partial x} \tag{2.6}$$

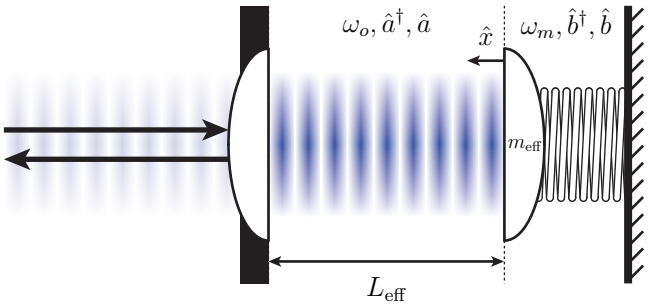

Figure 2.1: **Fabry-Perot cavity.** The canonical optomechanical system, a Fabry-Perot cavity of length $L_{\rm eff}$ with one mirror fixed and the other mounted on a spring with mass $m_{\rm eff}$. The intracavity optical field is described by a cavity mode frequency, ω_o, with associated photon creation/annihilation operators, $\hat{a}^\dagger$ and $\hat{a}$. The mechanical oscillator is described by a resonant frequency, ω_m, with associated phonon creation/annihilation operators, $\hat{b}^\dagger$ and $\hat{b}$. When the mirror moves by $\hat{x}$, the optical resonance condition changes to $\omega_o + \delta\omega_o = \omega_o(1 + \hat{x}/L_{\rm eff})$, resulting in an increased optical cavity energy of $\hbar\omega_o(1 + \hat{x}/L_{\rm eff})\hat{a}^\dagger\hat{a}$.

is the optomechanical coupling rate giving the optical frequency shift imparted by the zero-point motion of the mechanical system. The total Hamiltonian is thus

$$\hat{H} = \hbar\omega_o\hat{a}^\dagger\hat{a} + \hbar\omega_m\hat{b}^\dagger\hat{b} + \hbar g(\hat{b}^\dagger + \hat{b})\hat{a}^\dagger\hat{a}. \tag{2.7}$$

To move to an interaction picture rotating at a coherent drive frequency ω_ℓ, we apply the unitary transformation $\hat{U} = e^{i\omega_\ell\hat{a}^\dagger\hat{a}t}$ so that the Hamiltonian is now

$$\begin{aligned}\hat{H} \to \hat{U}\left(\hat{H} - i\hbar\frac{d}{dt}\right)\hat{U}^\dagger &= \hbar\omega_o\hat{a}^\dagger\hat{a} + \hbar\omega_m\hat{b}^\dagger\hat{b} + \hbar g(\hat{b}^\dagger + \hat{b})\hat{a}^\dagger\hat{a} - \hbar\omega_\ell\hat{a}^\dagger\hat{a} \\ &= \hbar\Delta\hat{a}^\dagger\hat{a} + \hbar\omega_m\hat{b}^\dagger\hat{b} + \hbar g(\hat{b}^\dagger + \hat{b})\hat{a}^\dagger\hat{a},\end{aligned} \tag{2.8}$$

having defined $\Delta \equiv \omega_o - \omega_\ell$.

The input–output formalism for a cavity mode coupled to a bath (outlined in Appendix B) allows the equations of motion for the system to be written

$$\dot{\hat{a}} = -\left(i\Delta + \frac{\kappa}{2}\right)\hat{a} - ig\hat{a}(\hat{b}^\dagger + \hat{b}) - \sqrt{\frac{\kappa_e}{2}}\hat{a}_{\rm in} - \sqrt{\kappa'}\hat{a}_{{\rm in},i}, \tag{2.9}$$

$$\dot{\hat{b}} = -\left(i\omega_m + \frac{\gamma_i}{2}\right)\hat{b} - ig\hat{a}^\dagger\hat{a} - \sqrt{\gamma_i}\hat{b}_{\rm in}. \tag{2.10}$$

The total optical and intrinsic mechanical loss rates are given by κ and γ_i respectively, with the latter giving the coupling to the thermal bath noise operator, $\hat{b}_{\rm in}$. We have also explicitly separated the coupling to the optical bath into detected (extrinsic) and undetected (intrinsic) channels, $\hat{a}_{\rm in}$ and $\hat{a}_{{\rm in},i}$, with respective coupling rates $\kappa_e/2$ and $\kappa' = \kappa - \kappa_e/2$. The factor of 1/2 models the behavior of the evanescent taper coupling scheme where there is back-reflection from the cavity, but

we only detect the transmitted signal (this is the scheme used for most of the systems in this work). In the input–output framework, this is equivalent to a two-sided cavity with symmetric loss rates. More correctly, we should write $\kappa = \kappa_e/2 + \kappa_e/2 + \kappa_i$, where κ_i is the *true* intrinsic loss rate of the cavity, so the loss rate to the undetected channels in (2.9) can be expressed as $\kappa' = \kappa_e/2 + \kappa_i$. We make this distinction because now it is clear that in the taper coupling scheme, $\kappa' \geq \kappa/2$, and the minimum loss rate to the undetected channel is $\kappa' = \kappa/2 = \kappa_e/2$ where we have set $\kappa_i = 0$. At the interaction boundary of the cavity mode and the bath, the bath noise operators satisfy

$$\hat{a}_{\text{out}} = \hat{a}_{\text{in}} + \sqrt{\frac{\kappa_e}{2}}\hat{a}, \tag{2.11}$$

$$\hat{b}_{\text{out}} = \hat{b}_{\text{in}} + \sqrt{\gamma_i}\hat{b}, \tag{2.12}$$

where experimentally, $\hat{a}_{\text{out}}$ represents the transmitted optical field. Usually, we can write $\hat{a}$ as a linear function of $\hat{a}_{\text{in}}$ so in the frequency domain we can implicitly define the optical cavity response function in transmission as $\hat{a}_{\text{out}}(\omega) = t(\omega)\hat{a}(\omega)$ and the optical cavity response function in reflection as $r(\omega) \equiv 1 - t(\omega)$.

The dynamics of the coupled optomechanical system described by (2.9) and (2.10) can be characterized by several dimensionless parameters:

- $Q_o \equiv \omega_o/\kappa$ and $Q_m \equiv \omega_m/\gamma_i$, respectively the optical and mechanical quality factor.
- κ/ω_m, the sideband resolution parameter. We will see that this determines the minimum phonon occupation.
- g/κ, the strong coupling parameter. This is a measure of the nonlinearity of the system in that for $g/\kappa > 1$, a single phonon will induce a significant shift ($>\kappa$) in the optical resonance frequency. Conversely, a single photon will strongly effect the momentum of the mirror. We can understand this intuitively in a Fabry-Perot cavity by comparing the momentum that the end mirror absorbs from a single photon introduced into the optical cavity to the zero-point momentum of the end mirror. The former is given by $(2\hbar\omega_o/c) \times (c/2L_{\text{eff}}) \times (1/\kappa)$, which is the photon impulse multiplied by the rate of incidence on the end mirror multiplied by the time spent in the cavity. The latter is given by $\sqrt{\hbar m_{\text{eff}}\omega_m/2}$. The ratio of the two is

  $$\frac{\hbar\omega_o/L_{\text{eff}}\kappa}{\sqrt{\hbar m_{\text{eff}}\omega_m/2}} = 2\frac{\omega_o}{L_{\text{eff}}}\frac{x_{\text{zpf}}}{\kappa} \approx \frac{g}{\kappa}, \tag{2.13}$$

  which for $g/\kappa > 1$ implies the aforementioned nonlinear behavior.
- Δ/κ, the detuning parameter.

The systems in this work typically have $\kappa/\omega_m \ll 1$ (the so-called good-cavity limit), $g/\kappa \ll 1$ (weak coupling approximation), $|\Delta/\kappa| \gg 1$ (since we usually work at $\Delta = \omega_m$), and $(Q_o, Q_m) \gg 1$ (high

quality factor cavities). A well-known method for solving the equations of motion is by linearizing about the steady state photon and phonon amplitudes, α_0 and β_0 satisfying

$$\alpha_0 = -\frac{\sqrt{\kappa_e/2}}{i(\Delta + g(\beta_0^* + \beta_0)) + \kappa/2}, \tag{2.14}$$

$$\beta_0 = -\frac{ig|\alpha_0|^2}{i\omega_m + \gamma_i/2}, \tag{2.15}$$

via the transformation $\hat{a} \to \alpha_0 + \hat{a}$ and $\hat{b} \to \beta_0 + \hat{b}$, where now $\langle \hat{a} \rangle = \langle \hat{b} \rangle = 0$ and the total photon number is given by $|\alpha_0|^2 + \langle \hat{a}^\dagger \hat{a} \rangle$. Qualitatively, the weak coupling approximation ensures the validity of the linear model ($|\hat{a}| \ll |\alpha_0|$) by bounding the perturbations caused by vacuum fluctuations; we do not want our dynamics to be significantly impacted by the vacuum field. The importance of the other bounds will be seen in the classical and quantum mechanical derivation of dynamics.

We note that (2.14) is a third-order polynomial equation with solutions that exhibit bistability for sufficiently strong input drive fields, with a stability criterion given by (for $\Delta > 0$) [71]

$$\omega_m \left(1 + \frac{4\Delta^2}{\kappa^2}\right) - \frac{4g^2|\alpha_0|^2}{\kappa^2}\Delta > 0. \tag{2.16}$$

While unstable solutions are a topic of interest, they are not the focus of this work. In the systems under consideration here, the even stricter *driven* weak coupling assumption, $G/\kappa \ll 1$ is valid, where we have introduced the cavity enhanced optomechanical coupling rate

$$G \equiv g\alpha_0 = g\sqrt{n_c}, \tag{2.17}$$

where n_c is the intracavity photon number. As a consequence, we consider only stable solutions to the steady state photon amplitude in the cavity, and we have $\Delta + g(\beta_0^* + \beta_0) \approx \Delta$.

2.1 Semiclassical Derivations of Observed Spectra

We first treat the system classically by representing the photon amplitude as a Fourier decomposition of sidebands and the phonon amplitude as the classical mechanical excitation amplitude. Substituting the ansatz

$$\hat{a} \to \alpha = \sum_q \alpha_q e^{-iq\omega_m t}, \tag{2.18}$$

$$\hat{b} \to \beta = \beta_0 e^{-i\omega_m t} \tag{2.19}$$

into (2.9), we get

$$-i\omega_m \sum_q q\alpha_q e^{-iq\omega_m t} = -\left(i\Delta + \frac{\kappa}{2}\right)\sum_q \alpha_q e^{-iq\omega_m t} - ig\beta_0 \sum_q \alpha_q \left(e^{-i(q+1)\omega_m t} + e^{-i(q-1)\omega_m t}\right) - \sqrt{\frac{\kappa_e}{2}}\alpha_{\text{in}}, \tag{2.20}$$

where $\alpha_{\text{in}} = \sqrt{P_{\text{in}}/\hbar\omega_o}$ is the driving field amplitude, P_{in} is the input power at the cavity, and the intrinsic noise operator is dropped in the classical limit. For now, we assume the mechanical oscillations are coherent so that β_0 is a simple complex number. For random oscillations however (such as thermal Brownian motion), β_0 will be a stochastic variable specified by a distribution. This issue will be addressed at the end of the next subsection. We can compactly express (2.20) as $\boldsymbol{M}\cdot\boldsymbol{\alpha} = \boldsymbol{\alpha}_{\text{in}}$ where

$$M_{pq} = \left(i(\Delta - p\omega_m) + \frac{\kappa}{2}\right)\delta_{pq} + ig\beta_0\left(\delta_{p,q+1} + \delta_{p,q-1}\right), \tag{2.21}$$

$$\alpha_{\text{in},p} = -\sqrt{\frac{\kappa_e}{2}}\alpha_{\text{in}}\delta_{p0}. \tag{2.22}$$

By truncating and inverting the coupling matrix, $\boldsymbol{M}$, we can determine the sideband amplitudes as $\alpha_q = (M^{-1})_{qp}\alpha_{\text{in},p}$ and therefore the steady state amplitude leaving the cavity to be

$$\alpha_{\text{out}} = \alpha_{\text{in}} + \sqrt{\frac{\kappa_e}{2}}\sum_q \alpha_q e^{-iq\omega_m t} \tag{2.23}$$

from the boundary equation, (2.11). The total power measured on a photodetector will thus be proportional to

$$|\alpha_{\text{out}}|^2 = |\alpha_{\text{in}}|^2 + \frac{\kappa_e}{2}\sum_q\sum_p \alpha_q\alpha_p^* e^{-i(q-p)\omega_m t} + 2\text{Re}\left\{\alpha_{\text{in}}\sqrt{\frac{\kappa_e}{2}}\sum_q \alpha_q e^{iq\omega_m t}\right\}. \tag{2.24}$$

2.1.1 Sideband-Resolved, Large Detuning Limit

The equations presented above are exact and can be solved for any case. In the sideband-resolved limit, $\kappa/\omega_m \ll 1$, the optomechanical phase modulation factor is proportional to g/ω_m, so only the first-order sidebands at $\omega = \omega_\ell \pm \omega_m$ ($q = \pm 1$) are significant. In this limit, (2.20) becomes the system of equations

$$0 = -\left(-i\Delta + \frac{\kappa}{2}\right)\alpha_0 - ig\beta_0(\alpha_+ + \alpha_-) - \sqrt{\frac{\kappa_e}{2}}\alpha_{\text{in}}, \tag{2.25}$$

$$\mp i\omega_m\alpha_\pm = -\left(-i\Delta + \frac{\kappa}{2}\right)\alpha_\pm - ig\beta_0\alpha_0. \tag{2.26}$$

Applying the approximation $\alpha_0 \gg \alpha_\pm$ to (2.25), (2.25), and (2.26) immediately gives

$$\alpha_0 = -\frac{\sqrt{\kappa_e/2}}{i\Delta + \kappa/2}\alpha_{\rm in}, \tag{2.27}$$

$$\alpha_\pm = -\frac{ig\beta_0}{i(\Delta \mp \omega_m) + \kappa/2}\alpha_0, \tag{2.28}$$

where $n_c \equiv |\alpha_0|^2$ is the intracavity photon number and

$$\begin{aligned} t(\Delta) &\equiv 1 - \alpha_0\sqrt{\kappa_e/2} \\ &= 1 - \frac{\kappa_e/2}{i\Delta + \kappa/2} \end{aligned} \tag{2.29}$$

gives the response of the cavity in transmission at $\omega_o - \omega_\ell$. We also have $|\alpha_{\rm in}| \gg |\alpha_0\sqrt{\kappa_e/2}| \gg |\alpha_\pm\sqrt{\kappa_e/2}|$. Therefore, the photodetector signal in (2.24) is dominated by terms proportional to $|\alpha_{\rm in}|^2$, $|\alpha_{\rm in}||\alpha_0|$, $|\alpha_{\rm in}||\alpha_\pm|$, and $|\alpha_0|^2$, and can be written

$$\begin{aligned} |\alpha_{\rm out}|^2 &= |\alpha_{\rm in}|^2 + \frac{\kappa_e}{2}|\alpha_0|^2 + 2\sqrt{\frac{\kappa_e}{2}}\alpha_{\rm in}{\rm Re}\{\alpha_0\} \\ &\quad + 2\sqrt{\frac{\kappa_e}{2}}\alpha_{\rm in}{\rm Re}\left\{\alpha_- e^{-i\omega_m t} + \alpha_+ e^{i\omega_m t}\right\} + \mathcal{O}(|\alpha_0||\alpha_\pm|) \\ &\approx |\alpha_{\rm in}|^2\left|1 - \frac{\kappa_e/2}{i\Delta + \kappa/2}\right|^2 \\ &\quad + \cos(\omega_m t)\Big(|A_+|\cos(\phi_+) + |A_-|\cos(\phi_-)\Big) \\ &\quad + \sin(\omega_m t)\Big(|A_+|\sin(\phi_+) - |A_-|\sin(\phi_-)\Big), \end{aligned} \tag{2.30}$$

where $A_\pm \equiv 2\alpha_{\rm in}\alpha_\pm\sqrt{\kappa_e/2} = |A_\pm|e^{-i\phi_\pm}$ and we have used the trigonometric summation identities (A.19) and (A.20). The first term in (2.30) is the DC cavity transmission spectrum with familiar Lorentzian shape. The remaining two terms compose the oscillating power at the mechanical frequency, with average oscillating power given by $\frac{\hbar\omega_o}{2}(A_{\rm cos}^2 + A_{\rm sin}^2)$, where $A_{\rm cos} = |A_+|\cos(\phi_+) + |A_-|\cos(\phi_-)$ and $A_{\rm sin} = |A_+|\sin(\phi_+) - |A_-|\sin(\phi_-)$.

For coherent mechanical oscillations where β_0 is a simple complex number, we can write the single sided power spectral density of the detected optical output power close to ω_m (given by the autocorrelation of $P(\omega) = \hbar\omega_o|\alpha_{\rm out}|^2$) as

$$\bar{S}_P(\omega, \Delta) \approx \frac{\hbar^2\omega_o^2\kappa_e^2 g^2|\beta_0|^2|\alpha_{\rm in}|^4}{2(\Delta^2 + (\kappa/2)^2)((|\Delta| - \omega_m)^2 + (\kappa/2)^2)} \times 2\pi\delta(\omega - \omega_m), \tag{2.31}$$

where we have applied the large detuning approximation, $|\Delta/\kappa| \gg 1$, so the $|A_-|$ ($|A_+|$) term is negligible for $\Delta/\kappa > 1$ ($-\Delta/\kappa > 1$).

If we have instead a mechanical system undergoing random thermal oscillations, (2.31) is no

longer valid since β_0 is no longer a simple complex number, and is instead a random process represented by a distribution. The autocorrelation function will now contain products of the form $\beta_0^*(t)\beta_0(t')$. Classically, the ensemble averages of these products can be calculated for a thermal state from the Bose-Einstein distribution, given in the frequency domain by $\langle\beta_0^*(\omega)\beta_0(\omega))\rangle = 1/(e^{\hbar\omega/k_BT_b}-1)$ where k_B is the Boltzmann constant and T_b is the bath temperature. For $\Delta/\kappa > 1$, the measured sideband frequency $(\omega_\ell + \omega_m)$ is blue of the pump frequency so from the quantum theory we will be considering normal ordered operators $(\hat{b}^\dagger\hat{b})$. Thus, (2.31) can be made valid for such oscillations in the $\Delta/\kappa > 1$ regime by substituting $|\beta_0|^2 \to \bar{n}$, the number of phonons occupying the mechanical mode, and replacing the Dirac delta functions $\delta(\omega - \omega_m)$ with unit-area Lorentzian functions. A more rigorous quantum mechanical derivation is given below.

2.1.2 Modified Result for a Weak Detuned Probe

Occasionally, we consider the case where in addition to a driving field α_{in} at ω_ℓ, we have a weak probe $\alpha_{\text{in},\pm}$ at $\omega_\ell \pm \Delta_p$ where we are interested in the cavity response. We have the modified ansatz

$$\hat{a} \to \alpha = \alpha_0 + \alpha_+ e^{-i\Delta_p t} + \alpha_- e^{i\Delta_p t}, \tag{2.32}$$

$$\hat{b} \to \beta = \beta_0 + \beta_+ e^{-i\Delta_p t} + \beta_- e^{i\Delta_p t}, \tag{2.33}$$

where it is assumed that in the sideband-resolved regime, the Fourier expansions can be truncated to the first-order sidebands, and that $|\alpha_0| \gg |\alpha_\pm|$ and $|\beta_0| \gg |\beta_\pm|$. Inserting these into (2.9) and (2.10) yields the system of equations

$$\mp i\Delta_p\alpha_\pm = -\left(i\Delta' + \frac{\kappa}{2}\right)\alpha_\pm - ig\alpha_0(\beta_\pm + \beta_\mp^*) - \sqrt{\frac{\kappa_e}{2}}\alpha_{\text{in},\pm}, \tag{2.34}$$

$$-i\Delta_p\beta_+ = -\left(i\omega_m + \frac{\gamma_i}{2}\right)\beta_+ - ig(\alpha_+\alpha_0^* + \alpha_0\alpha_-^*), \tag{2.35}$$

$$i\Delta_p\beta_- = -\left(i\omega_m + \frac{\gamma_i}{2}\right)\beta_- - ig(\alpha_+^*\alpha_0 + \alpha_0^*\alpha_-), \tag{2.36}$$

where $\Delta' = \Delta + g(\beta_0^* + \beta_0) \approx \Delta$ is the drive detuning accounting for the steady state cavity frequency shift and we have again dropped the noise terms in the classical limit. We make the large detuning assumption that $\Delta/\kappa > 1$ (the driving field is red of the optical cavity), allowing both α_- and β_- to be neglected (so long as $\Delta_p/\gamma_i \gg 1$). With these approximations, (2.34) and (2.35) can be solved, giving

$$\beta_+ = -\frac{ig\alpha_+\alpha_0^*}{i(\omega_m - \Delta_p) + \gamma_i/2}, \tag{2.37}$$

$$\alpha_+ = -\frac{\sqrt{\kappa_e/2}}{i(\Delta - \Delta_p) + \kappa/2 + \frac{g^2|\alpha_0|^2}{i(\omega_m - \Delta_p) + \gamma_i/2}}\alpha_{\text{in},+}. \tag{2.38}$$

The transmission frequency response of the cavity at the probe frequency $\omega_\ell + \Delta_p$ for a fixed $\Delta/\kappa > 1$ is simply

$$t_+(\Delta_p) = 1 - \frac{\kappa_e/2}{i(\Delta - \Delta_p) + \kappa/2 + \frac{g^2|\alpha_0|^2}{i(\omega_m - \Delta_p) + \gamma_i/2}}. \tag{2.39}$$

We can arrive at a similar result for $-\Delta/\kappa > 1$, giving

$$t_-(\Delta_p) = 1 - \frac{\kappa_e/2}{i(\Delta + \Delta_p) + \kappa/2 + \frac{g^2|\alpha_0|^2}{i(\omega_m - \Delta_p) - \gamma_i/2}}. \tag{2.40}$$

2.2 Quantum Mechanical Derivations of Dynamics

We now derive a fully quantum mechanical theory for the optomechanical cavity dynamics (with credit to Amir Safavi-Naeini for the original derivation), beginning again with (2.9) and (2.10). We linearize these equations about a steady state intracavity photon amplitude, α_0, satisfying

$$\alpha_0 = -\frac{\sqrt{\kappa_e/2}}{i\Delta + \kappa/2}\alpha_{\text{in}}, \tag{2.41}$$

by mapping $\hat{a} \to \alpha_0 + \hat{a}(t)$, where $\langle \hat{a}(t) \rangle = 0$. In the unrotated (lab) frame, the optical cavity mode occupancy is now given by $|\alpha_0|^2 + \langle \hat{a}^\dagger \hat{a} \rangle$, and we note that in the rotated frame, the steady state occupancy is now the vacuum. Representing time-dependent operators with their Fourier decomposition (A.1) and keeping only terms that are first-order in the fluctuating operators $\hat{a}(\omega)$ and $\hat{b}(\omega)$ allows (2.9) and (2.10) to be rewritten in the frequency domain as

$$\hat{a}(\omega) = \frac{-\sqrt{\kappa_e/2}\hat{a}_{\text{in}}(\omega) - \sqrt{\kappa'}\hat{a}_{\text{in},i}(\omega) - iG(\hat{b}(\omega) + \hat{b}^\dagger(\omega))}{i(\Delta - \omega) + \kappa/2}, \tag{2.42}$$

$$\hat{b}(\omega) = \frac{-\sqrt{\gamma_i}\hat{b}_{\text{in}}(\omega) - iG(\hat{a}(\omega) + \hat{a}^\dagger(\omega))}{i(\omega_m - \omega) + \gamma_i/2}. \tag{2.43}$$

From these expressions, we see that $\hat{a}(\omega)$ is a function that is peaked at Δ with a characteristic linewidth of κ, while $\hat{b}(\omega)$ is a function that is very sharply peaked at ω_m with a characteristic linewidth of γ_i. Thus, these functions both have negligible value for ω far away from ω_m.

To produce an expression dependent only on the input fields, we substitute (2.42) into (2.43) to

get

$$\begin{aligned}\hat{b}(\omega) = &\frac{-\sqrt{\gamma_i}\hat{b}_{\rm in}(\omega)}{i(\omega_m-\omega)+\gamma_i/2} \\ &- \frac{iG}{i(\omega_m-\omega)+\gamma_i/2}\left(\frac{-\sqrt{\kappa_e/2}\hat{a}_{\rm in}(\omega)-\sqrt{\kappa'}\hat{a}_{{\rm in},i}-iG\hat{b}(\omega)}{i(\Delta-\omega)+\kappa/2}\right) \\ &- \frac{iG}{i(\omega_m-\omega)+\gamma_i/2}\left(\frac{-\sqrt{\kappa_e/2}\hat{a}^\dagger_{\rm in}(\omega)-\sqrt{\kappa'}\hat{a}^\dagger_{{\rm in},i}+iG\hat{b}(\omega)}{-i(\Delta+\omega)+\kappa/2}\right) \\ = &\frac{-\sqrt{\gamma_i}\hat{b}_{\rm in}(\omega)}{i(\omega_m-\omega)+\gamma_i/2} \\ &+ \frac{iG}{i(\omega_m-\omega)+\gamma_i/2}\left(\frac{\sqrt{\kappa_e/2}\hat{a}_{\rm in}(\omega)+\sqrt{\kappa'}\hat{a}_{{\rm in},i}}{i(\Delta-\omega)+\kappa/2}+\frac{\sqrt{\kappa_e/2}\hat{a}^\dagger_{\rm in}(\omega)+\sqrt{\kappa'}\hat{a}^\dagger_{{\rm in},i}}{-i(\Delta+\omega)+\kappa/2}\right) \\ &- \frac{|G|^2}{i(\omega_m-\omega)+\gamma_i/2}\left(\frac{1}{i(\Delta-\omega)+\kappa/2}-\frac{1}{-i(\Delta+\omega)+\kappa/2}\right)\hat{b}(\omega), \end{aligned} \tag{2.44}$$

where (A.3) has been used to eliminate $\hat{b}^\dagger(\omega)$ terms which are sharply peaked around $-\omega_m$. Defining $\omega'_m \equiv \omega_m + \delta\omega_m$ (the optical spring shifted mechanical frequency) and $\gamma \equiv \gamma_i + \gamma_{\rm OM}$ (the optically damped mechanical loss rate) where

$$\delta\omega_m \equiv |G|^2 {\rm Im}\left\{\frac{1}{i(\Delta-\omega_m)+\kappa/2}-\frac{1}{-i(\Delta+\omega_m)+\kappa/2}\right\}, \tag{2.45}$$

$$\gamma_{\rm OM} \equiv 2|G|^2 {\rm Re}\left\{\frac{1}{i(\Delta-\omega_m)+\kappa/2}-\frac{1}{-i(\Delta+\omega_m)+\kappa/2}\right\}, \tag{2.46}$$

(2.44) can be rearranged to write finally

$$\begin{aligned}\hat{b}(\omega) = &\frac{-\sqrt{\gamma_i}\hat{b}_{\rm in}(\omega)}{i(\omega'_m-\omega)+\gamma/2} \\ &+ \frac{iG}{i(\omega'_m-\omega)+\gamma/2}\left(\frac{\sqrt{\kappa_e/2}\hat{a}_{\rm in}(\omega)+\sqrt{\kappa'}\hat{a}_{{\rm in},i}}{i(\Delta-\omega)+\kappa/2}+\frac{\sqrt{\kappa_e/2}\hat{a}^\dagger_{\rm in}(\omega)+\sqrt{\kappa'}\hat{a}^\dagger_{{\rm in},i}}{-i(\Delta+\omega)+\kappa/2}\right). \end{aligned} \tag{2.47}$$

We note that we have set $\omega = \omega_m$ in (2.45) and (2.46) since $\delta\omega_m(\omega)$ and $\gamma_{\rm OM}(\omega)$ both have a characteristic linewidth of κ and are therefore approximately constant over the bandwidth of $\hat{b}(\omega)$ (assuming $\gamma_i \ll \kappa$, which is true in the systems presented here). In the driven weak coupling approximation, we can further make the self-consistent assumption that $\delta\omega_m \ll (\omega_m, \kappa, \gamma)$ so that $\omega'_m \approx \omega_m$ for the remainder of this derivation. From (2.46), we can define a cooperativity parameter

$$C \equiv \left|\frac{\gamma_{\rm OM}}{\gamma_i}\right|. \tag{2.48}$$

Assuming that the input optical field is quantum limited and there are no thermal excitations (an excellent approximation since $\hbar\omega_o \gg k_B T$ for any temperature we operate at in this work) we

have the correlations of the respective operators (as shown in Appendix B) given by

$$\langle \hat{a}_{\rm in}^\dagger(\omega)\hat{a}_{\rm in}(\omega')\rangle = 0, \tag{2.49}$$

$$\langle \hat{a}_{\rm in}(\omega)\hat{a}_{\rm in}^\dagger(\omega')\rangle = \delta(\omega+\omega'), \tag{2.50}$$

$$\langle \hat{a}_{{\rm in},i}^\dagger(\omega)\hat{a}_{{\rm in},i}(\omega')\rangle = 0, \tag{2.51}$$

$$\langle \hat{a}_{{\rm in},i}(\omega)\hat{a}_{{\rm in},i}^\dagger(\omega')\rangle = \delta(\omega+\omega'), \tag{2.52}$$

$$\langle \hat{b}_{\rm in}^\dagger(\omega)\hat{b}_{\rm in}(\omega')\rangle = n_b\delta(\omega+\omega'), \tag{2.53}$$

$$\langle \hat{b}_{\rm in}(\omega)\hat{b}_{\rm in}^\dagger(\omega')\rangle = (n_b+1)\delta(\omega+\omega'), \tag{2.54}$$

where $n_b = 1/(e^{\hbar\omega_m/k_BT}-1)$ is the thermal bath phonon population at the mechanical frequency, $k_B = 1.3806488(13)\times10^{-23}\ \mathrm{J\cdot K^{-1}}$ is the Boltzmann constant [28], and T is the bath temperature. With these correlations known and the expression (2.47), it is possible to compute the steady state mechanical mode occupancy, $\bar{n} \equiv \langle \hat{b}^\dagger\hat{b}\rangle$. We have

$$\begin{aligned}\langle \hat{b}^\dagger(t)\hat{b}(t)\rangle &= \frac{1}{2\pi}\int_{-\infty}^{\infty} d\omega \int_{-\infty}^{\infty} d\omega'\, \langle e^{-i\omega t}e^{-i\omega' t}\hat{b}^\dagger(\omega)\hat{b}(\omega')\rangle \\ &= \frac{1}{2\pi}\int_{-\infty}^{\infty} d\omega\, S_{bb}(\omega),\end{aligned} \tag{2.55}$$

where we recognize the integrand to be equivalent to the spectral density of $\hat{b}$, given by

$$\begin{aligned}S_{bb}(\omega) &= \int_{-\infty}^{\infty} d\omega'\, \langle \hat{b}^\dagger(\omega)\hat{b}(\omega')\rangle \\ &= \frac{\gamma_i n_b}{(\omega_m+\omega)^2+(\gamma/2)^2} + \frac{|G|^2}{(\omega_m+\omega)^2+(\gamma/2)^2}\frac{\kappa_e/2+\kappa'}{(\Delta-\omega)^2+(\kappa/2)^2} \\ &= \frac{\gamma}{(\omega_m+\omega)^2+(\gamma/2)^2}\left(\frac{\gamma_i n_b}{\gamma} + \frac{|G|^2\kappa}{\gamma}\frac{1}{(\Delta-\omega)^2+(\kappa/2)^2}\right).\end{aligned} \tag{2.56}$$

Integrating this spectrum yields the detuning dependent cavity phonon population,

$$\bar{n}(\Delta) = \frac{\gamma_i n_b}{\gamma} + \frac{|G|^2\kappa}{\gamma}\frac{1}{(\Delta+\omega_m)^2+(\kappa/2)^2}, \tag{2.57}$$

where we have assumed the bracketed term in (2.56) is approximately constant over the bandwidth of the expression and substituted $\omega = -\omega_m$.

2.2.1 Sideband-Resolved, Mechanical Frequency Detuned Limit

In the sideband-resolved regime, $\kappa/\omega_m \ll 1$, we can evaluate (2.57) for different detunings, yielding

$$\bar{n} \approx \begin{cases} \dfrac{\gamma_i n_b}{\gamma} + \dfrac{|G|^2\kappa}{4\gamma\omega_m^2} \approx \dfrac{\gamma_i n_b}{\gamma} + \dfrac{\gamma_{\rm OM}}{\gamma}\left(\dfrac{\kappa}{4\omega_m}\right)^2, & \text{if } \Delta = \omega_m \quad \text{(cooling)}, \\ \dfrac{\gamma_i n_b}{\gamma} + \dfrac{|G|^2\kappa}{\gamma}\dfrac{1}{\omega_m^2 + (\kappa/2)^2}, & \text{if } \Delta = 0 \quad \text{(on resonance)}, \\ \dfrac{\gamma_i n_b}{\gamma} + \dfrac{4|G|^2}{\gamma\kappa} \approx \dfrac{\gamma_i n_b}{\gamma} - \dfrac{\gamma_{\rm OM}}{\gamma}, & \text{if } \Delta = -\omega_m \quad \text{(amplification)}, \end{cases} \tag{2.58}$$

where $\gamma_{\rm OM} \approx \pm 4|G|^2/\kappa$ for $\Delta = \pm\omega_m$. The $\Delta = \omega_m$ case exhibits the quantum limit on minimum achievable phonon number given by $\bar{n}_{\rm min} = (\kappa/4\omega_m)^2$ as derived by [29, 31, 72]. This residual heating effect arises from anti-Stokes scattering to the nonresonant $\omega_\ell - \omega_m$ sideband and is suppressed by the sideband resolution factor. We see then the importance of $\kappa/4\omega_m < 1$ ($\kappa/4\omega_m \ll 1$ ideally) in attempting to cool the phonon occupation of the mechanical mode below unity.

To get an expression for $\hat{a}(\omega)$ in terms of only the input bath operators in the large detuning limit $|\Delta/\kappa| \gg 1$, we substitute, (2.47) into (2.42) to get

$$\begin{aligned} \hat{a}(\omega) = {} & \frac{\sqrt{\kappa_e/2}\hat{a}_{\rm in}(\omega) + \sqrt{\kappa'}\hat{a}_{{\rm in},i}(\omega)}{i(\Delta-\omega)+\kappa/2}\left(\pm\frac{|G|^2}{i(\Delta-\omega)+\kappa/2}\frac{1}{i(\omega_m \mp \omega)+\gamma/2} - 1\right) \\ & + \frac{\sqrt{\kappa_e/2}\hat{a}^\dagger_{\rm in}(\omega) + \sqrt{\kappa'}\hat{a}^\dagger_{{\rm in},i}(\omega)}{i(\Delta-\omega)+\kappa/2}\left(\pm\frac{|G|^2}{-i(\Delta+\omega)+\kappa/2}\frac{1}{\pm i(\omega_m \mp \omega)+\gamma/2}\right) \\ & + \frac{i\sqrt{\gamma_i}G\hat{b}_{{\rm in},\pm}(\omega)}{i(\Delta-\omega)+\kappa/2}\left(\frac{1}{\pm i(\omega_m \mp \omega)+\gamma/2}\right), \end{aligned} \tag{2.59}$$

for $\pm\Delta/\kappa > 1$, where

$$\hat{b}_{{\rm in},\pm}(\omega) = \begin{cases} \hat{b}(\omega), & \text{if } \Delta/\kappa > 1 \quad \text{(red side driving)}, \\ \hat{b}^\dagger(\omega), & \text{if } -\Delta/\kappa > 1 \quad \text{(blue side driving)}. \end{cases} \tag{2.60}$$

Using the boundary equation $\hat{a}_{\rm out} = \hat{a}_{\rm in} + \sqrt{\kappa_e/2}\hat{a}$ and (2.59), we can write the output field in

the form

$$\begin{aligned}\hat{a}_{\rm out}(\omega) &= \left(1 - \frac{\kappa_e/2}{i(\Delta-\omega)+\kappa/2} \pm \frac{\kappa_e/2}{(i(\Delta-\omega)+\kappa/2)^2}\frac{|G|^2}{\pm i(\omega_m \mp \omega)+\gamma/2}\right)\hat{a}_{\rm in}(\omega) \\ &+ \left(-\frac{\sqrt{\kappa_e\kappa'/2}}{i(\Delta-\omega)+\kappa/2} \pm \frac{\sqrt{\kappa_e\kappa'/2}}{(i(\Delta-\omega)+\kappa/2)^2}\frac{|G|^2}{\pm i(\omega_m \mp \omega)+\gamma/2}\right)\hat{a}_{{\rm in},i}(\omega) \\ &+ \left(\frac{i\sqrt{\kappa_e\gamma_i/2}}{i(\Delta-\omega)+\kappa/2}\frac{G}{\pm i(\omega_m \mp \omega)+\gamma/2}\right)\hat{b}_{{\rm in},\pm}(\omega) \\ &+ \left(\pm\frac{\kappa_e/2}{(i(\Delta-\omega)+\kappa/2)(-i(\Delta+\omega)+\kappa/2)}\frac{|G|^2}{\pm i(\omega_m \mp \omega)+\gamma/2}\right)\hat{a}^\dagger_{\rm in}(\omega) \\ &+ \left(\pm\frac{\sqrt{\kappa_e\kappa'/2}}{(i(\Delta-\omega)+\kappa/2)(-i(\Delta+\omega)+\kappa/2)}\frac{|G|^2}{\pm i(\omega_m \mp \omega)+\gamma/2}\right)\hat{a}^\dagger_{{\rm in},i}(\omega) \\ &= t_\pm(\omega)\hat{a}_{\rm in} + \eta_\pm(\omega)\hat{a}_{{\rm in},i} + s_{12,\pm}(\omega)\hat{b}_{{\rm in},\pm}, \end{aligned} \tag{2.61}$$

where in the last line, we have dropped the conjugate terms in the resolved sideband approximation, $\kappa/\omega_m \ll 1$, and we label the remaining bath operator coefficients with scattering matrix terminology as outlined in [73]. The fluctuating optical power at the photodiode is proportional to $\hat{N}(\omega) = \hat{a}_{\rm out}(\omega) + \hat{a}^\dagger_{\rm out}(\omega)$ [74], with a spectral density given specifically for $\Delta = \omega_m$ by

$$\begin{aligned} S_{NN}(\omega) &= \int_{-\infty}^{\infty} d\omega'\, t_+(\omega)t^*(-\omega')\langle\hat{a}_{\rm in}(\omega)\hat{a}^\dagger_{\rm in}(\omega')\rangle + \eta_+(\omega)\eta^*_+(-\omega')\langle\hat{a}_{{\rm in},i}(\omega)\hat{a}^\dagger_{{\rm in},i}(\omega')\rangle \\ &\quad + s_{12,+}(\omega)s^*_{12,+}(-\omega')\langle\hat{b}_{\rm in}(\omega)\hat{b}^\dagger_{\rm in}(\omega')\rangle + s^*_{12,+}(-\omega)s_{12,+}(\omega')\langle\hat{b}^\dagger_{\rm in}(\omega)\hat{b}_{\rm in}(\omega')\rangle \\ &= |t_+(\omega)|^2 + |\eta_+(\omega)|^2 + |s_{12,+}(\omega)|^2 + n_b(|s_{12,+}(\omega)|^2 + |s_{12,+}(-\omega)|^2), \end{aligned} \tag{2.62}$$

where the correlations given by (2.49)–(2.54) are used to greatly simplify the expression. Using the properties of the scattering matrix, $|t_+(\omega)|^2 + |\eta_+(\omega)|^2 + |s_{12,+}(\omega)|^2 = 1$ (energy conservation), we can simplify (2.62) to

$$\begin{aligned} S_{NN}(\omega) &= 1 + \frac{4\kappa_e|G|^2}{\kappa^2}\frac{\gamma_i n_b}{2}\left(\frac{1}{(\omega_m-\omega)^2+(\gamma/2)^2} + \frac{1}{(\omega_m+\omega)^2+(\gamma/2)^2}\right) \\ &= 1 + \frac{4\kappa_e|G|^2}{\kappa^2}\bar{S}_{bb}(\omega), \end{aligned} \tag{2.63}$$

where we have similarly applied the sideband-resolved approximation to $\bar{S}_{bb}(\omega)$. We note that the signal-to-noise ratio (SNR) improves linearly with the extrinsic coupling rate and that at $\bar{n} = 0$, the SNR vanishes. Equivalently, we can say that at $\Delta = \omega_m$, the optical bath is not sensitive to the zero-point fluctuations of the mechanical system.

We can compare (2.63) to the classical derived equation (2.31) from above by defining the optical power spectral density at the detector, near $\omega = \omega_m$, as $\bar{S}_{\rm P}(\omega) = 2S_{PP}(\omega) = 2\hbar^2\omega_o^2|\alpha_{\rm in}|^2 S_{NN}(\omega)$, where we assume that in the large detuning approximation, the optical drive is not significantly

depleted by the cavity. Substituting (2.56) into (2.63), and using (2.41) for the steady state cavity photon population,

$$\begin{aligned}\bar{S}_P(\omega) &= 2\hbar^2\omega_o^2|\alpha_{\text{in}}|^2 + \frac{8\hbar^2\omega_o^2|\alpha_{\text{in}}|^2\kappa_e g^2|\alpha_0|^2}{\kappa^2}\frac{\gamma\bar{n}}{2}\left(\frac{1}{(\omega_m+\omega)^2+(\gamma/2)^2}+\frac{1}{(\omega_m-\omega)^2+(\gamma/2)^2}\right)\\ &\approx 2\hbar^2\omega_o^2|\alpha_{\text{in}}|^2 + \frac{\hbar^2\omega_o^2\kappa_e^2 g^2\bar{n}|\alpha_{\text{in}}|^4}{2(\Delta^2+(\kappa/2)^2)(\kappa/2)^2}\times 2\pi\frac{1}{\pi}\frac{\gamma/2}{(\omega_m-\omega)^2+(\gamma/2)^2},\end{aligned} \tag{2.64}$$

we see we have a nearly identical expression with the addition of the photon shot noise term, the substitution $|\beta_0|^2 \to \bar{n}$, and a unit area Lorentzian function in place of the Dirac delta function (as discussed at the end of Section 2.1.1).

Chapter 3

Optomechanical Device Design

The simplicity of the theoretical Fabry-Perot cavity model of optomechanics masks the complexity and diversity of the experimental realizations, from suspended membranes [23, 24, 42], to microtoroids [45, 50], to microwave resonators [35], to larger [37] or more exotic [75] structures. Even within the Painter group, a variety of optomechanical platforms have emerged, including the "zipper" double nanobeam cavities [56, 57], single nanobeam cavities [59, 60], and quasi-2D cavities [62, 63, 76].

Here, the focus will be on quasi-1D patterned silicon nanobeams designed for backaction cooling the mean phonon occupation of its mechanical mode, $\bar{n}$, below unity. From the derivations in Section 2.2, we already know that this can only be achieved for $\kappa/4\omega_m < 1$. Assuming we are in the sideband-resolved regime with some large steady state intracavity photon population (but still in the driven weak coupling regime) and using (2.48) and (2.57), we have

$$\bar{n} \approx \frac{\gamma_i \kappa}{4|G|^2} \frac{k_B T_b}{\hbar \omega_m}. \tag{3.1}$$

With the minimization of (3.1) in mind, the goal then is to design a device with small intrinsic optical and mechanical losses (or equivalently, large optical and mechanical quality factors), large optomechanical coupling, and large mechanical frequency.

These structures will be designed for a silicon-on-insulator substrate (SOI) with a device layer of 220 nm to take advantage of mature fabrication techniques for this material system in the Painter group. The operating principle is a perturbation in an otherwise periodic dielectric (a "defect") to tightly colocalize an optical and mechanical resonance to the same sub-cubic-wavelength volume, greatly enhancing their interaction strength—an optomechanical crystal. Being periodic structures, band diagrams will be used to provide an intuitive explanation for the unit cell choice. Finite element analysis combined with electromagnetic perturbation theory to account for the moving dielectric boundaries [77] and the photoelastic effect [78] will be used to model the coupling in these structures. Numerical minimization techniques will be used to optimize the geometric parameters.

To mitigate mechanical losses in these structures, work in complete phononic bandgaps [63] will be leveraged. For more detailed discussion and history of the design principles presented here, see [56, 59, 62].

3.1 Crystal Theory

We begin by briefly reviewing the physics of a periodic dielectric (a significantly more detailed treatment can be found in [79, 80]). Classical electromagnetism is governed entirely by Maxwell's equations, given in its microscopic form supposing an isotropic medium with no free charges or currents, for an electric field, $\boldsymbol{E}(\boldsymbol{x}, t)$, and a magnetic field, $\boldsymbol{B}(\boldsymbol{x}, t)$, as

$$\nabla \cdot \boldsymbol{D} = 0, \tag{3.2}$$

$$\nabla \cdot \boldsymbol{B} = 0, \tag{3.3}$$

$$\nabla \times \boldsymbol{E} = -\frac{\partial \boldsymbol{B}}{\partial t}, \tag{3.4}$$

$$\nabla \times \boldsymbol{H} = \frac{\partial \boldsymbol{D}}{\partial t}. \tag{3.5}$$

In these equations, $\boldsymbol{D} = \varepsilon(\boldsymbol{x})\boldsymbol{E}$ is the displacement field related to the electric field by $\varepsilon(\boldsymbol{x})$, the permittivity of the material, and $\boldsymbol{B} = \mu(\boldsymbol{x})\boldsymbol{H}$ is the magnetizing field, related to the magnetic field by $\mu(\boldsymbol{x})$, the permeability of the material (equal to the permeability of free space, μ_0, for most materials). Bold variables indicate vector values and $\boldsymbol{x}$ is the coordinate vector. For linear equations, we can always decompose the field solutions into a sum of time harmonic modes, so without loss of generality, we can examine Maxwell's equations for single mode oscillating at ω in the form

$$\boldsymbol{E}(\boldsymbol{x}, t) = \boldsymbol{E}(\boldsymbol{x})e^{i\omega t}, \tag{3.6}$$

$$\boldsymbol{B}(\boldsymbol{x}, t) = \boldsymbol{B}(\boldsymbol{x})e^{i\omega t}, \tag{3.7}$$

so we have

$$\nabla \cdot \varepsilon(\boldsymbol{x})\boldsymbol{E}(\boldsymbol{x}) = 0, \tag{3.8}$$

$$\nabla \cdot \boldsymbol{B}(\boldsymbol{x}) = 0, \tag{3.9}$$

$$\nabla \times \boldsymbol{E}(\boldsymbol{x}) = -i\omega \boldsymbol{B}(\boldsymbol{x}), \tag{3.10}$$

$$\nabla \times \boldsymbol{B}(\boldsymbol{x}) = i\frac{\omega \varepsilon_r(\boldsymbol{x})}{c^2}\boldsymbol{E}(\boldsymbol{x}), \tag{3.11}$$

where $\varepsilon(\boldsymbol{x}) = \varepsilon_0 \varepsilon_r(\boldsymbol{x})$, ε_0 is the permittivity of free space and we have the convenient relationship $c = 1/\sqrt{\mu_0 \varepsilon_0}$ relating the free space constants to the speed of light. Substituting (3.11) into (3.10),

we have the governing eigenequation

$$\hat{\Theta}\boldsymbol{B}(\boldsymbol{x}) = \frac{\omega^2}{c^2}\boldsymbol{B}(\boldsymbol{x}), \tag{3.12}$$

having defined the Hermitian operator

$$\hat{\Theta}\boldsymbol{B}(\boldsymbol{x}) \equiv \nabla \times \frac{1}{\varepsilon_r(\boldsymbol{x})}\nabla \times \boldsymbol{B}(\boldsymbol{x}). \tag{3.13}$$

It can be shown that such equations have an orthogonal set of eigenfunction solutions with real eigenvalues [81].

3.1.1 Plane Waves

For a homogeneous medium, we can see that the plane wave solution $\boldsymbol{B}(\boldsymbol{x}) = \boldsymbol{B}_0 e^{i\boldsymbol{k}\cdot\boldsymbol{x}}$ (where $\boldsymbol{B}_0$ is any constant vector) is an eigenfunction with eigenvalue $|\boldsymbol{k}|^2/\varepsilon_r$. The governing equation requires $(\omega/c)^2 = |\boldsymbol{k}|^2/\varepsilon_r$, known as the dispersion relation.

3.1.2 Translational Symmetry

Suppose we have another operator $\hat{O}$ satisfying the canonical commutation relation $[\hat{\Theta}, \hat{O}] = 0$ and eigenfunction $\boldsymbol{B}(\boldsymbol{x})$ satisfying (3.12). Then we have

$$\hat{\Theta}\hat{O}\boldsymbol{B}(\boldsymbol{x}) = \hat{O}\hat{\Theta}\boldsymbol{B}(\boldsymbol{x}) = \frac{\omega^2}{c^2}\hat{O}\boldsymbol{B}(\boldsymbol{x}), \tag{3.14}$$

which says that $\hat{O}\boldsymbol{B}(\boldsymbol{x}) = \alpha\boldsymbol{B}(\boldsymbol{x})$ for some simple scalar value α. This is itself an eigenequation, so $\boldsymbol{B}(\boldsymbol{x})$ is also an eigenfunction of $\hat{O}$. Thus, if we can find operators that commute with $\hat{\Theta}$ (that are hopefully simpler than $\hat{\Theta}$), we can use them to classify solution of (3.12).

One possibility is the discrete translation operator $\hat{T}_a \equiv f(\boldsymbol{x} + n\boldsymbol{a})$ for integer values of n. If we also have $T_a\varepsilon(\boldsymbol{x}) = \varepsilon(\boldsymbol{x})$ (the dielectric is periodic in the $\boldsymbol{a}$ direction with periodicity $a = |\boldsymbol{a}|$), then clearly, the commutator $[\hat{T}_a, \hat{O}]$ vanishes. For simplicity, consider the case where $\boldsymbol{a}$ is parallel to the x-axis. The translation operator then has a simple set of eigenfunctions with the form e^{ikx}, with eigenvalues e^{ikna} which we can label with a wavenumber k. We see that the wavevector e^{ikx} and $e^{i(k+2\pi m/a)x}$ (for some integer m) have the same eigenvalue and thus form a degenerate eigenspace spanned by the orthonormal set of eigenfunctions, $e^{i(k+2\pi m/a)x}$, labelled by m. Defining $\boldsymbol{b} = (2\pi/a)\hat{x}$ as the primitive reciprocal lattice vector, we must have then that

$$\begin{aligned}\boldsymbol{B}_k(\boldsymbol{x}) &= \sum_m \boldsymbol{B}_{k,m}(x,y)e^{i(k+mb)x} \\ &= e^{ikx}\bar{\boldsymbol{B}}_k(\boldsymbol{x}),\end{aligned} \tag{3.15}$$

where $\bar{\boldsymbol{B}}_k$ is periodic in x by construction.

This result that discrete periodicity results in a solution that is a product of a plane wave and a periodic function is known as Bloch's theorem with the Bloch state given by (3.15). A Bloch state is characterized by the property that states with wavevectors differing by integer multiples of the reciprocal lattice vector are identical, so we need only be concerned with $-\pi/a \leq k < \pi/a$ (called the Brillouin zone). We can further restrict the range of k to the irreducible Brillouin zone $0 \leq k < \pi/a$ by time reversal symmetry (valid for all the systems studied here). Typically, $k = 0$ is called the Γ symmetry point and $k = \pi/a$ is called the X symmetry point.*

To determine the actual form of $\boldsymbol{b}_k(\boldsymbol{x})$, we solve (3.12) using (3.15) as the ansatz, giving the new form of the governing equation

$$(ik\hat{x} + \nabla) \times \frac{1}{\varepsilon(\boldsymbol{x})}(ik\hat{x} + \nabla) \times \bar{\boldsymbol{B}}_k(\boldsymbol{x}) = \frac{\omega^2(k)}{c^2}\bar{\boldsymbol{B}}_k(\boldsymbol{x}), \tag{3.16}$$

subject to

$$(ik\hat{x} + \nabla) \cdot \bar{\boldsymbol{B}}_k(\boldsymbol{x}) = 0 \tag{3.17}$$

$$\bar{\boldsymbol{B}}_k(\boldsymbol{x}) = \bar{\boldsymbol{B}}_k(\boldsymbol{x} + na\hat{x}), \tag{3.18}$$

where the last line is the periodic boundary condition. Thus, for each value of k, we expect to find an infinite number of eigenvalue solutions, $\omega_n(k)$, continuous in k, but discretely spaced in n. Plotting $\omega_n(k)$ against k in the irreducible Brillouin zone yields the band structure of a periodic structure, from which many of its optical properties can be inferred.

3.1.3 Bandgaps and Localization

We can plot the eigenvalue solutions, $\omega_n(k)$, for the case where $\varepsilon(\boldsymbol{x})$ is composed of alternating layers of ε_1 and ε_2, with equal thickness, $a/2$, in the $\hat{x}$ direction (Figure 3.1). We see that there are frequency ranges where no crystal modes exist for any value of k, called bandgaps. The bands immediately below and above the bandgap are referred to as the dielectric and air band respectively (due to the distribution of field energy), analogous to the valence and conduction band in electronic band structures.

If we artificially introduce a traveling wave at a frequency inside the bandgap into the crystal, in the crystal basis, it will be assigned a complex k vector resulting in exponential decay in the spatial coordinate (since e^{ikx} now has a real component and is no longer purely oscillatory). We can see this by expanding the dispersion relation at the band edge to second-order, giving $\Delta\omega \approx \alpha(\Delta k)^2$,

*In higher degrees of symmetry, solutions are instead labeled by $\boldsymbol{k}$ and additional symmetry points will be introduced. For example, a 2D periodic rectangular lattice of circular holes has an irreducible Brillouin zone given by $0 \leq k_x < \pi/a$, $0 \leq k_y \leq k_x$, where we label $k_x = k_y = \pi/a$ as the M point.

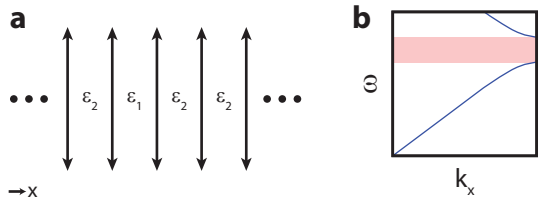

Figure 3.1: **Bandgaps in a 1D periodic dielectric. a**, Dielectric configuration for the example in the text, showing alternating dielectric slabs of ε_1 and ε_2, each of width $a/2$. **b**, Corresponding band diagram for $\varepsilon_1 \neq \varepsilon_2$ with the red region indicating a frequency range for which no real solutions exist (a bandgap). The band above the bandgap is typically referred to as the air band, and the band below the bandgap is typically referred to as the dielectric band.

where α depends on the curvature of the band and the linear term disappears due to time-reversal symmetry. For the air band, we can see from Figure 3.1b that $\alpha > 0$, so for $\Delta\omega < 0$ (moving into the bandgap), $\Delta k = \sqrt{\Delta\omega/\alpha}$, and k acquires an imaginary component. The dielectric band yields the same result for $\alpha < 0$ and $\Delta\omega > 0$. From this, we can infer that the decay factor is proportional to $\Delta\omega/\alpha$, so we get the strongest attenuation factor for frequencies far away from the band edge, and for bands that are very flat.

We can introduce a defect into this dielectric by changing the thickness of a single layer and approximate the entire system as a dielectric slab surrounded on either side by a frequency dependent mirror (with large reflection coefficients for frequencies in the bandgap). Thus, at frequencies commensurate with the gap, we effectively have an optical cavity, leading to a discretized optical mode spectrum in the bandgap region with frequency spacing inversely proportional to the width of the defect layer. By this reasoning, for a defect layer thickness of $(1+\delta)a/2$, with $0 < \delta \ll 1$, the defect state will be very close dielectric band. Conversely, for $0 < -\delta \ll 1$, the defect state will be very close to the air band. Thus, we can talk about defects that "draw" modes from the air/dielectric band.

3.1.4 Phononic Bloch States

A similar theory can be developed for acoustic waves propagating in a solid [82, 83], though the formulation is slightly more complex owing to the mixing of the longitudinal and transverse components of acoustic waves so that for a displacement field $\boldsymbol{Q}(\boldsymbol{x})$, $\nabla \cdot \boldsymbol{Q}(\boldsymbol{x}) \neq 0$ in general. An excellent practical resource for the subject, in the context of finite element simulation can be found in [84]. The governing equation for an acoustic wave traveling in a homogeneous medium with scalar density field, $\rho(\boldsymbol{x})$, rank 4 elasticity tensor, $\boldsymbol{C}(\boldsymbol{x})$, and no body forces, is (in component notation for clarity)

$$\frac{1}{\rho(\boldsymbol{x})}\nabla_j C_{ijmn}(\boldsymbol{x})\nabla_n Q_m(\boldsymbol{x},t) = \frac{\partial^2}{\partial t^2}Q_i(\boldsymbol{x},t). \tag{3.19}$$

The elasticity tensor in Voigt notation (Appendix A.8) for an isotropic medium is

$$\boldsymbol{C} = \begin{bmatrix} c_{11} & c_{12} & c_{12} & 0 & 0 & 0 \\ c_{12} & c_{11} & c_{12} & 0 & 0 & 0 \\ c_{12} & c_{12} & c_{11} & 0 & 0 & 0 \\ 0 & 0 & 0 & c_{44} & 0 & 0 \\ 0 & 0 & 0 & 0 & c_{44} & 0 \\ 0 & 0 & 0 & 0 & 0 & c_{44} \end{bmatrix}, \tag{3.20}$$

where $c_{11} = K(\boldsymbol{x}) + 4\mu(\boldsymbol{x})/3$, $c_{12} = K(\boldsymbol{x}) - 2\mu(\boldsymbol{x})/3$, and $c_{44} = \mu(\boldsymbol{x})$, $K(\boldsymbol{x})$ is the bulk modulus and $\mu(\boldsymbol{x})$ is the shear modulus. Similar to above, we can assume a time harmonic solution and write the governing equation as

$$\hat{\Phi}\boldsymbol{Q}(\boldsymbol{x}) = \omega^2 \boldsymbol{Q}(\boldsymbol{x}), \tag{3.21}$$

where

$$\hat{\Phi}\boldsymbol{Q}(\boldsymbol{x}) = \frac{1}{\rho(\boldsymbol{x})} \nabla^T (\boldsymbol{C}(\boldsymbol{x}) \nabla \boldsymbol{Q}(\boldsymbol{x}, t)). \tag{3.22}$$

In principle then, we can derive a phononic Bloch state (analogous to the photonic Bloch state), labeled by a wavenumber, k, with an associated spectrum of eigenvalue solutions, $\omega_n(k)$.

3.2 Index Guiding

We consider the case of an infinite slab, ε_1, embedded in an infinite dielectric medium, ε_2 (Figure 3.2a), with a wavevector incident on the interface as shown in Figure 3.2b. We have the boundary conditions $\omega_1 = \omega_2$ (by energy conservation) and $k_{1,\parallel} = k_{2,\parallel}$ (by translation invariance, where $\parallel$ is relative to the boundary). Since $k_\parallel = |\boldsymbol{k}| \sin\theta$ and $\omega = c|\boldsymbol{k}|/n$ (the dispersion relation from above, and $n = \sqrt{\varepsilon}$, is the refractive index of the material), we have

$$n_1 \sin\theta_1 = n_2 \sin\theta_2, \tag{3.23}$$

which is effectively Snell's law from ray optics. An equivalent to total internal reflection when $n_2 < n_1$ must also exist for wavevectors. If we consider the field far away from the boundary in ε_2, it must be essentially composed of free propagating plane waves, each with a characteristic frequency, ω, and wavevector amplitude set by the dispersion relation. The wavevector amplitude of these plane waves can be written as the quadrature sum of the parallel and perpendicular components, $|\boldsymbol{k}|^2 = (\omega n_2/c)^2 = k_\perp^2 + k_\parallel^2$. Since there is no condition limiting $k_\perp$, each value of $k_\parallel$ has associated

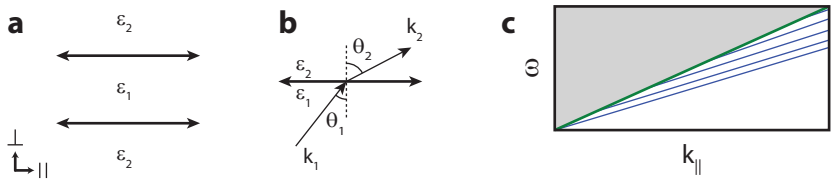

Figure 3.2: **Index guiding in an infinite slab.** **a**, Dielectric configuration for the example in the text, showing an infinite dielectric slab, ε_1, in an otherwise isotropic dielectric medium, ε_2, with parallel ($\parallel$) and perpendicular ($\perp$) directions indicated. **b**, A wavevector, $\boldsymbol{k_1}$, is incident on the ε_1–ε_2 boundary at angle θ_1. The resulting $\boldsymbol{k_2}$ wavevector depends on the boundary conditions discussed in the text. **c**, Corresponding band diagram with the gray region representing the continuum of modes above the light line (solid green line, described by $\omega = ck_\parallel/\sqrt{\varepsilon_2}$), with discrete modes below (blue lines).

with it a continuum of modes above $\omega > ck_\parallel/n_2$, corresponding to $|k_\perp| \in [0, \infty)$. The equality $\omega = ck_\parallel/n_2$ is known as the light line. The modes below the light line, have imaginary wavevector amplitudes ($k_\perp^2 = (n_2\omega/c)^2 - k_\parallel^2 < 0$) in ε_2, which results in exponential decay away from the interface. Thus, they are *localized* to ε_1 and are termed index-guided modes.

In *quasi*-1D waveguide structures like nanobeams, periodicity (and therefore Bragg confinement) exists only along the axial direction. It is this effect that gives rise to confinement in the off-axial directions.

3.3 Optomechanical Coupling Rate

The optomechanical coupling rate,

$$g = \frac{d\omega_o}{d\alpha} x_{\mathrm{zpf}} = \frac{d\omega_o}{d\alpha} \sqrt{\frac{\hbar}{2m_{\mathrm{eff}}\omega_m}}, \tag{3.24}$$

defined with respect to the generalized coordinate, α, and effective motional mass, m_{eff}, measures the frequency shift in the optical mode frequency imparted by the zero-point motion of the oscillator. In the canonical Fabry-Perot system, the simplest choice of generalized coordinate is the displacement of the movable end mirror, resulting in a motional mass that coincides with the mirror's true mass. In more complex systems such as nanobeams where the mode displacement is represented by a vector field, $\boldsymbol{Q}(\boldsymbol{x})$, a choice for the generalized coordinate is an overall scaling parameter of this field. For a unit-normalized mode displacement field, $\boldsymbol{q}(\boldsymbol{x})$, we can parameterize the motion of the mode as $\boldsymbol{Q}(\boldsymbol{x}) \to \boldsymbol{Q}(\alpha, \boldsymbol{x}) = \alpha \boldsymbol{q}(\boldsymbol{x})$. The effective mass is related to this choice by the requirement that the potential energy of this parameterized oscillator must of course be equal to the true potential energy.

This condition can be expressed as

$$\frac{1}{2}\omega_m^2 \int d\boldsymbol{x}\, \rho(\boldsymbol{x})|\boldsymbol{Q}(\boldsymbol{x})|^2 = \frac{1}{2} m_{\text{eff}} \omega_m^2 \alpha^2, \tag{3.25}$$

so we have for our particular choice of α,

$$m_{\text{eff}} = \frac{\int d\boldsymbol{x}\, \rho(\boldsymbol{x})|\boldsymbol{Q}(\alpha, \boldsymbol{x})|^2}{\alpha^2} = \int d\boldsymbol{x}\, \rho(\boldsymbol{x})|\boldsymbol{q}(\boldsymbol{x})|^2, \tag{3.26}$$

where $\rho(\boldsymbol{x})$ is the scalar density field of the material.

To compute the frequency shift with respect to a change in α, we employ first-order electromagnetic perturbation theory [85], giving

$$\frac{d\omega_o}{d\alpha} = -\frac{\omega_o}{2} \frac{\langle \boldsymbol{E}(\boldsymbol{x})| \frac{d\varepsilon(\boldsymbol{x})}{d\alpha} |\boldsymbol{E}(\boldsymbol{x})\rangle}{\langle \boldsymbol{E}(\boldsymbol{x})|\varepsilon(\boldsymbol{x})|\boldsymbol{E}(\boldsymbol{x})\rangle} = -\frac{\omega_o}{2} \frac{\int d\boldsymbol{x}\, \frac{d\varepsilon(\boldsymbol{x})}{d\alpha} |\boldsymbol{E}(\boldsymbol{x})|^2}{\int d\boldsymbol{x}\, \varepsilon(\boldsymbol{x})|\boldsymbol{E}(\boldsymbol{x})|^2}, \tag{3.27}$$

where $\boldsymbol{E}(\boldsymbol{x})$ is the unperturbed electric field vector and $\varepsilon(\boldsymbol{x})$ is the permittivity. We consider two effects which give rise to frequency shifts: the moving dielectric boundary, caused by the motion of the mechanical mode, and the photoelastic effect, caused by a change in the refractive index due to dynamic stresses. While there are many other effects that can contribute (e.g., thermorefractive effects, carrier density changes, surface effects), they were assumed to be negligible in comparison. The total optomechanical coupling rate is then approximated by

$$g = g_{\text{mb}} + g_{\text{pe}} = \left(\left.\frac{d\omega_o}{d\alpha}\right|_{\text{mb}} + \left.\frac{d\omega_o}{d\alpha}\right|_{\text{pe}} \right) x_{\text{zpf}}. \tag{3.28}$$

3.3.1 Moving Dielectric Boundary

We follow here the derivation by Johnson et al. [77] and represent the nanobeam as a closed volume of uniform dielectric, ε_1, undergoing a perturbation specified by the displacement field, $\boldsymbol{Q}(\alpha, \boldsymbol{x})$ (Figure 3.3a). Let us first consider the simpler 1D situation, $\varepsilon(x) = \varepsilon_2 + (\varepsilon_1 - \varepsilon_2)\Theta(x - x_0 - Q(\alpha, x_0))$ (where $\Theta(x)$ is the Heaviside function and x_0 is the location of the unperturbed boundary; shown in Figure 3.3a). We find then

$$\begin{aligned}
\left\langle E(x) \left| \frac{d\varepsilon(x)}{d\alpha} \right| E(x) \right\rangle &= \left\langle E(x) \left| \frac{d\varepsilon(x)}{dQ(\alpha, x)} \frac{dQ(\alpha, x)}{d\alpha} \right| E(x) \right\rangle \\
&= \int dx\, (\varepsilon_1 - \varepsilon_2)\delta(x - x_0 - Q(\alpha, x_0)) \frac{dQ(\alpha, x)}{d\alpha} |E(x)|^2 \\
&= \left. \frac{dQ(\alpha, x)}{d\alpha} (\varepsilon_1 - \varepsilon_2)|E(x)|^2 \right|_{x = x_0},
\end{aligned} \tag{3.29}$$

where $Q(\alpha, x_0) \ll x_0$ (for a small perturbation). Returning to the original problem and parameterizing the surface using (u, v), we can define a surface unit normal, $\hat{\boldsymbol{n}}(u, v)$, at the ε_1–ε_2 interface.

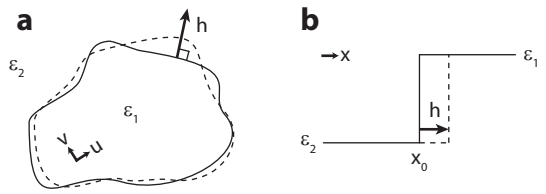

Figure 3.3: **Moving dielectric boundary.** **a**, From [77], schematic showing an infinite space of permittivity ε_2 in which we place a closed volume of permittivity ε_1 (solid line) with a perturbation specified by the surface function $h(\alpha, u, v) = \boldsymbol{Q}(\alpha, u, v) \cdot \hat{\boldsymbol{n}}(u, v)$ (dashed line). The surface itself has been parameterized with (u, v). **b**, An equivalent 1D case for a dielectric boundary at x_0, perturbed by $h(\alpha) = Q(\alpha, x_0)$ (dashed line).

Then, the volume integral in the numerator of (3.27) becomes a surface integral given by

$$\begin{aligned}\left\langle \boldsymbol{E}(\boldsymbol{x}) \left| \frac{d\varepsilon(\boldsymbol{x})}{d\alpha} \right| \boldsymbol{E}(\boldsymbol{x}) \right\rangle &= \oint_A dA \, \frac{d\boldsymbol{Q}(\alpha, u, v) \cdot \hat{\boldsymbol{n}}(u, v)}{d\alpha} (\varepsilon_1 - \varepsilon_2) |\boldsymbol{E}(u, v)|^2 \\ &= \oint_A dA \, \frac{dh(\alpha, u, v)}{d\alpha} (\varepsilon_1 - \varepsilon_2) |\boldsymbol{E}(u, v)|^2, \end{aligned} \tag{3.30}$$

in analogy to (3.29), and we have also set $dA \equiv dudv$ and defined $h(\alpha, u, v) \equiv \boldsymbol{Q}(\alpha, u, v) \cdot \hat{\boldsymbol{n}}(u, v)$. The problem with this expression is that it is generally undefined, owing to the discontinuous nature of $\boldsymbol{E}_\perp \equiv \boldsymbol{E} \cdot \hat{\boldsymbol{n}}$ (since we require $\varepsilon_1 \boldsymbol{E}_{\perp,1} = \varepsilon_2 \boldsymbol{E}_{\perp,2}$ across a boundary). Mathematically, this manifests as a finite first-order correction, even for vanishing α, ruining the assumptions of perturbation theory. For $\varepsilon_1 \approx \varepsilon_2$, we could pick a side and proceed with the analysis, but for silicon in air (with refractive indices of 3.48 and 1 respectively), this is clearly not good approximation.

The solution to this is to find a dielectric function that *smoothly* transitions from ε_1 to ε_2, allowing the field components to stay continuous. If such a dielectric function could be parameterized in a way that this transition, in the limit, becomes the step function we desire, the uniqueness theorem of Maxwell's equations guarantees that the resultant expression will be correct (as long as the limit is well defined). With this in mind, we focus on a small, locally flat, region of the interface and define the coordinate, x, parallel to $\hat{\boldsymbol{n}}$ with the origin at the boundary. We have then (nearly identical to the 1D case),

$$\varepsilon(x) = \varepsilon_1 + (\varepsilon_2 - \varepsilon_1)\Theta(x - h). \tag{3.31}$$

In this local coordinate system, we can define an anisotropic permittivity tensor

$$\boldsymbol{\varepsilon}_s(x) = \begin{bmatrix} \bar{\varepsilon}_s(x) & 0 & 0 \\ 0 & \bar{\varepsilon}_s(x) & 0 \\ 0 & 0 & \bar{\varepsilon}_s(x) \end{bmatrix}, \tag{3.32}$$

where

$$\bar{\varepsilon}_s(x) = \int dx'\, g_s(x-x')\varepsilon(x'), \tag{3.33}$$

$$\frac{1}{\tilde{\varepsilon}_s(x)} = \int dx'\, g_s(x-x')\frac{1}{\varepsilon(x')}, \tag{3.34}$$

and $g_s(x)$ is a unit area, localized distribution around $x = 0$ with the property $\lim_{s\to 0} g_s(x) = \delta(x)$. We see that in the limit $s \to 0$, $\boldsymbol{\varepsilon}_s(x) = \varepsilon(x)$. From the properties of derivatives, we also have

$$\frac{d\bar{\varepsilon}_s(x)}{dh} = (\varepsilon_1 - \varepsilon_2)g_s(x-h), \tag{3.35}$$

$$\frac{d\tilde{\varepsilon}_s(x)}{dh} = -\tilde{\varepsilon}_s(x)^2\left(\frac{1}{\varepsilon_1} - \frac{1}{\varepsilon_1}\right)g_s(x-h). \tag{3.36}$$

Still in the local coordinate system, the electric field can be separated into components perpendicular to the boundary, $\boldsymbol{E}_\perp$, and parallel to the boundary, $\boldsymbol{E}_\parallel$. Then $\boldsymbol{E}_\perp$ is sensitive only to $\tilde{\varepsilon}$ and $\boldsymbol{E}_\parallel$ is sensitive only to $\bar{\varepsilon}$. We can evaluate the integral $\langle \boldsymbol{E}|\frac{d\boldsymbol{\varepsilon}_s(x)}{d\alpha}|\boldsymbol{E}\rangle$ in this flat region, giving

$$\begin{aligned}\left\langle \boldsymbol{E}\left|\frac{d\boldsymbol{\varepsilon}_s(x)}{d\alpha}\right|\boldsymbol{E}\right\rangle &= \left\langle \boldsymbol{E}\left|\frac{d\boldsymbol{\varepsilon}_s(x)}{dh}\frac{dh}{d\alpha}\right|\boldsymbol{E}\right\rangle \\ &= dA\frac{dh}{d\alpha}\int dx\,\left((\varepsilon_1-\varepsilon_2)|\boldsymbol{E}_\parallel|^2 - \left(\frac{1}{\varepsilon_1}-\frac{1}{\varepsilon_2}\right)|\tilde{\varepsilon}_s(x)\boldsymbol{E}_\perp|^2\right)g_s(x-h).\end{aligned} \tag{3.37}$$

Integrating this expression over the entire surface, (u, v), and taking the limit $s \to 0$ yields

$$\oint_A dA\,\frac{dh(\alpha,u,v)}{d\alpha}\left((\varepsilon_1-\varepsilon_2)|\boldsymbol{E}_\parallel(u,v)|^2 - \left(\frac{1}{\varepsilon_1}-\frac{1}{\varepsilon_2}\right)|\varepsilon(u,v)\boldsymbol{E}_\perp(u,v)|^2\right), \tag{3.38}$$

where the integrand is now well behaved across the boundary. The full first-order correction due to the moving dielectric boundary is thus

$$\left.\frac{d\omega_o}{d\alpha}\right|_{\text{mb}} = -\frac{\omega_o}{2}\frac{\oint_A dA\,\boldsymbol{q}(u,v)\cdot\hat{\boldsymbol{n}}(u,v)\left(\Delta\varepsilon|\boldsymbol{E}_\parallel(u,v)|^2 - \Delta\varepsilon^{-1}|\boldsymbol{D}_\perp(u,v)|^2\right)}{\int d\boldsymbol{x}\,\varepsilon(\boldsymbol{x})|\boldsymbol{E}(\boldsymbol{x})|^2}, \tag{3.39}$$

where $\Delta\varepsilon = \varepsilon_1 - \varepsilon_2$ and $\Delta\varepsilon^{-1} = \varepsilon_1^{-1} - \varepsilon_2^{-1}$.

3.3.2 Photoelastic Effect

The motion of the mechanical mode creates a local variation in strain which that can alter the refractive index of the material. We once again compute the first-order frequency correction under the influence of the displacement field $\boldsymbol{Q}(\alpha, \boldsymbol{x}) = \alpha\boldsymbol{q}(\boldsymbol{x})$ via (3.27). The photoelastic shift for a

Wavelength	p_{11}	p_{12}	p_{44}	Ref.
1.15 μm	-0.101 ± 0.007	0.009 ± 0.001	–	[87]
3.39 μm	-0.094 ± 0.005	0.017 ± 0.001	-0.051 ± 0.002	[87]

Table 3.1: **Photoelastic coefficients for silicon.** We note that we estimate the value for $\lambda_o = 1.55$ μm as somewhere between the listed values since data for that wavelength is not available.

general refractive index tensor, $\boldsymbol{\varepsilon}$, is given by [86] to be

$$\frac{d\boldsymbol{\varepsilon}}{d\alpha} = -\boldsymbol{\varepsilon}\left(\frac{\boldsymbol{pS}}{\varepsilon_0}\right)\boldsymbol{\varepsilon}, \tag{3.40}$$

where $\boldsymbol{p}$ is the rank-four photoelastic tensor and $\boldsymbol{S}$ is the strain tensor with matrix elements defined as

$$S_{ij} = \frac{1}{2}\left(\frac{dq_i}{dx_j} + \frac{dq_j}{dx_i}\right). \tag{3.41}$$

For an isotropic medium (encompassing all the systems in this thesis), this simplifies to

$$\frac{d\varepsilon_{ij}}{d\alpha} = -\varepsilon_0 n^4 p_{ijkl} S_{kl}, \tag{3.42}$$

where $n = \sqrt{\varepsilon/\varepsilon_0}$ is the refractive index and $\varepsilon_{ij} = \varepsilon\delta_{ij}$. The symmetry of $\boldsymbol{\varepsilon}$ and $\boldsymbol{S}$ also requires $p_{ijkl} = p_{jikl} = p_{ijlk} = p_{jilk}$ so it is convenient to use a contracted index notation (Appendix A.8) where

$$\begin{aligned} S_1 &= S_{xx}, \\ S_2 &= S_{yy}, \\ S_3 &= S_{zz}, \\ S_4 &= 2S_{yz}, \\ S_5 &= 2S_{xz}, \\ S_6 &= 2S_{xy}, \end{aligned} \tag{3.43}$$

which also allows the photoelastic tensor to be expressed as a 6×6 matrix. Specifically for silicon (which again, encompasses all of the systems discussed in this thesis), the photoelastic tensor has the form [86]

$$\boldsymbol{p} = \begin{bmatrix} p_{11} & p_{12} & p_{12} & 0 & 0 & 0 \\ p_{12} & p_{11} & p_{12} & 0 & 0 & 0 \\ p_{12} & p_{12} & p_{11} & 0 & 0 & 0 \\ 0 & 0 & 0 & p_{44} & 0 & 0 \\ 0 & 0 & 0 & 0 & p_{44} & 0 \\ 0 & 0 & 0 & 0 & 0 & p_{44} \end{bmatrix}, \tag{3.44}$$

with coefficients given by Table 3.1, and it is assumed that the crystal unit cell coordinate system is aligned with the coordinate system for the electric field (e.g., $\langle 100 \rangle$ corresponds to the x-, y-, and z-axis).* In the contracted index notation, (3.42) can be written

$$\frac{d\boldsymbol{\varepsilon}}{d\alpha} = -\varepsilon_0 n^4 \boldsymbol{p}\boldsymbol{S} = -\varepsilon_0 n^4 \begin{bmatrix} p_{11}S_1 + p_{12}S_2 + p_{12}S_3 \\ p_{12}S_1 + p_{11}S_2 + p_{12}S_3 \\ p_{12}S_1 + p_{12}S_2 + p_{11}S_3 \\ p_{44}S_4 \\ p_{44}S_5 \\ p_{44}S_6 \end{bmatrix}, \tag{3.45}$$

which can be easily converted back to Cartesian indices by reversing (3.43), giving

$$\frac{d\boldsymbol{\varepsilon}}{d\alpha} = -\varepsilon_0 n^4 \begin{bmatrix} p_{11}S_{xx} + p_{12}(S_{yy} + S_{zz}) & p_{44}S_{xy} & p_{44}S_{xz} \\ p_{44}S_{xy} & p_{11}S_{yy} + p_{12}(S_{xx} + S_{zz}) & p_{44}S_{yz} \\ p_{44}S_{xz} & p_{44}S_{yz} & p_{11}S_{zz} + p_{12}(S_{xx} + S_{yy}) \end{bmatrix}. \tag{3.46}$$

The full first-order correction due to the photoelastic effect is thus

$$\begin{aligned} \left.\frac{d\omega_o}{d\alpha}\right|_{\text{pe}} = \frac{\omega_o \varepsilon_0 n^4}{2} \int_{\text{Si}} d\boldsymbol{x} \Big(& 2\text{Re}\{E_x^* E_y\} p_{44} S_{xy} \\ & + 2\text{Re}\{E_x^* E_z\} p_{44} S_{xz} \\ & + 2\text{Re}\{E_y^* E_z\} p_{44} S_{yz} \\ & + |E_x|^2 (p_{11} S_{xx} + p_{12}(S_{yy} + S_{zz})) \\ & + |E_y|^2 (p_{11} S_{yy} + p_{12}(S_{xx} + S_{zz})) \\ & + |E_z|^2 (p_{11} S_{zz} + p_{12}(S_{xx} + S_{yy})) \Big) \Big/ \int d\boldsymbol{x}\, \varepsilon |\boldsymbol{E}|^2, \end{aligned} \tag{3.47}$$

*If this is not the case, we can construct a rotated form of the photoelastic tensor, shown in Appendix C.

where ε and the elements of both $\boldsymbol{E}$ and $\boldsymbol{S}$ are functions of coordinate, and the numerator is a volume integral over only the silicon material.

3.4 Designing Nanobeams with Numerical Simulations

Numerical simulations were done primarily using a combination of MIT Photonic-Bands (MPB) [64] and COMSOL Multiphysics [65] with MATLAB [88] support. The former was used for generating optical band diagrams. The latter was used for mechanical band diagrams and full optical/mechanical cavity simulations. Numerous scripts were developed to facilitate these simulations, and are listed in Appendix F.

3.4.1 Unit Cell Design

We first examine the nominal unit cell of the nanobeam as shown in Figure 3.4a, geometrically a simple block with a hole. While technically the unit cell can have any number of holes in any shape (indeed, square holes were initially used quite successfully [59, 60]), a single oval hole was chosen for simplicity in fabrication, and because nanobeams with circular holes have previously produced cavity modes with large optical quality factors [89]. The corresponding optical (Figure 3.4c) and mechanical (Figure 3.4f) band diagram is generated using MPB and COMSOL respectively. In waveguide structures, the continuum of unguided optical modes above the light line precludes the existence of a complete photonic bandgap, but as they couple poorly to the guided modes below the light line (quantified by their small overlap integral), we can consider instead "quasi-bandgaps" which allow for such weakly coupled modes in the gap. By classifying bands by their vector symmetry across the y and z planes, we can extend this definition to include modes of differing symmetry; while technically possessing vanishing mode overlap, in reality they couple weakly due to symmetry breaking introduced by the fabrication process. This quasi-bandgap idea extends analogously to phononics, without having to worry about the unguided continuum of modes since acoustic modes are confined to propagate in the material.

The challenge now is first picking an appropriate pair of optical and mechanical modes, and then determining a perturbation to the nominal unit cell that simultaneously localizes the pair in their respective quasi-bandgaps. The optomechanical coupling equation (3.28) allows many of the mechanical modes to be eliminated as candidates on the basis of symmetry arguments. In (3.39), we see that the electric field components contribute as squared terms (even functions) whereas the displacement field contributes as linear terms (odd functions). In (3.47), lower-order optical modes typically have a dominant field polarization so that the first three terms are generally much smaller then the last three. In the last three terms, we see that again, the electric field components contribute as even functions while the displacement field components contribute as odd functions.

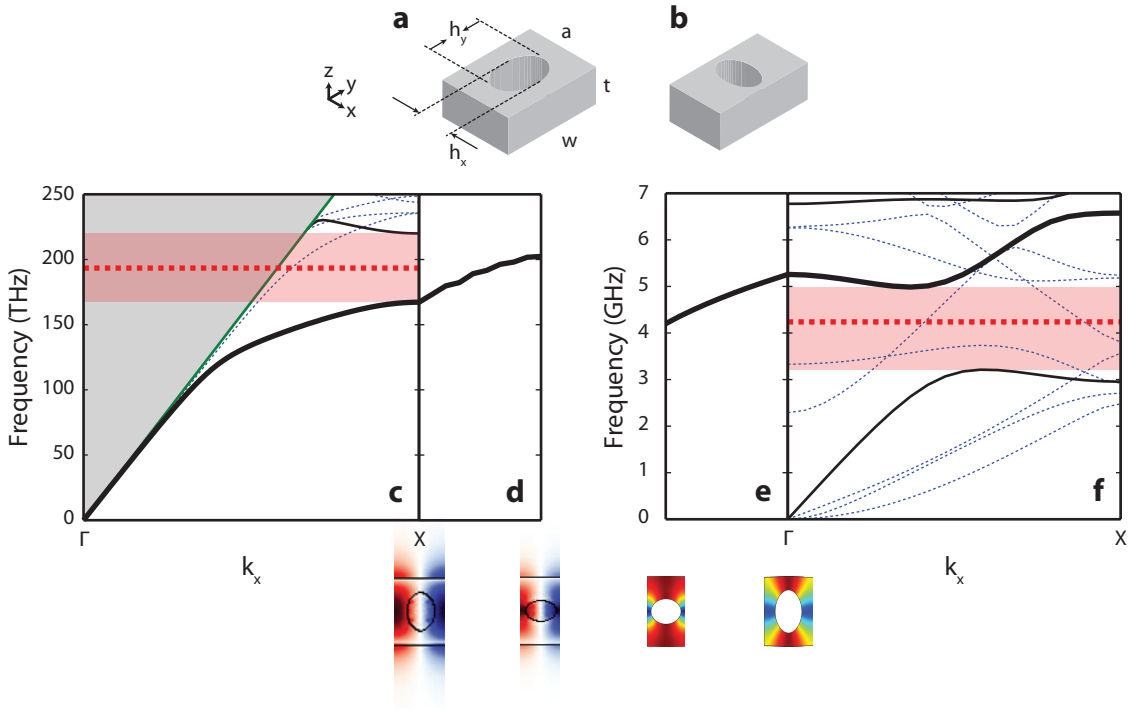

Figure 3.4: **Nanobeam unit cell band diagrams.** **a**, The nominal, and **b**, the defect unit cells of the nanobeam specified by the set of geometric (a, t, w, h_x, h_y). The related **c**, optical, and **f**, mechanical band structure for propagation along the x-axis in the nominal unit cell, with quasi-bandgaps (red regions) and cavity mode frequencies (red dashed) indicated. In **c**, the light line (green) divides the diagram into two regions: the gray shaded region above representing a continuum of unguided modes, and the white region below containing guided modes with y-odd and z-even vector symmetry in the electric field (black), and modes of other vector symmetries (blue dashed). In **f**, modes that are y- and z-symmetric (black), and modes of other vector symmetries (blue dashed) are indicated. Emphasis is placed on the bands from which the localized cavity modes are formed (thick black). Lastly, the frequency tuning of **d**, the X-point optical, and **e**, the Γ-point mechanical mode of interest, corresponding to changing from the nominal to the defect unit cell while keeping the k vector constant, is shown. Below the respective tuning plots are the $E_y(\boldsymbol{x})$ field solutions and the displacement field, $|\boldsymbol{Q}(\boldsymbol{x})|$, solutions.

We can therefore restrict consideration to mechanical modes that are symmetric across the y and z planes. We can further restrict the choice of mechanical modes to the Γ symmetry point by noting that modes at X symmetry point experience a π phase change at the unit cell boundary, so that unit cell pairs will nominally have vanishing optomechanical coupling.

Based on this intuition, we choose an optical mode drawn from the X symmetry point of the dielectric band and a mechanical "breathing" mode (with a displacement field predominantly along the y-axis) drawn from the Γ-point (from the emphasized bands in Figure 3.4c, f). From Figure 3.4d–e, we see that simultaneously reducing a (causing the optical mode frequency to increase), and "squishing" the hole so that h_y/h_x decreases (effectively increasing the motional mass, causing a reduction in the mechanical mode frequency) is the desired perturbation.

3.4.2 Cavity Design

An optomechanical cavity can be formed by transitioning (over M unit cell periods) from the nominal unit cell composing the "mirror" region, to the defect unit cell. The confinement of both the optical and mechanical mode is achieved in the axial ($\hat{x}$) direction by Bragg scattering in this mirror region. Index guiding confines the optical mode in the transverse ($\hat{y}$ and $\hat{z}$) direction. Labeling these transition unit cells with an index, $j \in [0, M]$, starting with the defect unit cell and ending the with nominal unit cell, we need to define three functions of this index: a_j, to set the scaling of the unit cell width (a), r_j, to set the scaling of the hole ratio (h_y/h_x), and s_j, to set the scaling of the unit cell hole area. These functions can essentially have any form, as long as they conform to the desired perturbation from the previous section (to ensure that a localized optomechanical mode exists). This requirement can be represented as the set of conditions

$$0 < r_j < r_{j+1}, \tag{3.48}$$

$$0 < a_j < a_{j+1}, \tag{3.49}$$

$$r_M = s_M = a_M = 1. \tag{3.50}$$

For example, in [59], we had

$$a_j = 1 - d\left(\left(\frac{M-i}{M}\right)^2 - 1\right), \tag{3.51}$$

where $d = 1 - \min\{a_j\}$ is the "depth" of the defect, and $r_j = s_j = 1$.

In practice, to reduce this infinitely large parameter space to a slightly smaller infinity, we set $1 - s_j = \chi(1 - a_j)$ and $r_j = a_j^{\xi}$, where $\chi \in (-\infty, \infty)$ and $\xi \in (0, \infty)$. This is so that the only function we need to define is a_j, with the other two functions related by a simple scalar parameters. We further note that we would like a_j to be as smooth as possible. To see why, consider an electromagnetic wave propagating along the nanobeam. For a particular k-vector, each unit cell has a basis of normal modes which compose this propagating wave. However, for every k-vector, there are unconfined modes located above the light line. Thus, if adjacent unit cells are significantly different, the vector for the propagating wave in the local unit cell basis might have a significant number of its components in these unconfined modes, leading to large scattering losses. This idea is explored extensively in [90] via Fourier analysis of the optical cavity mode, resulting in very high quality factor 2D photonic crystals with very small mode volumes. The problem with (3.51) is that the change in $\Delta a_j = a_{j+1} - a_j$ at $j = M$ in is quite large. We can fix this by requiring

$$\left.\frac{da(x)}{dx}\right|_{x=0,1} = 0, \tag{3.52}$$

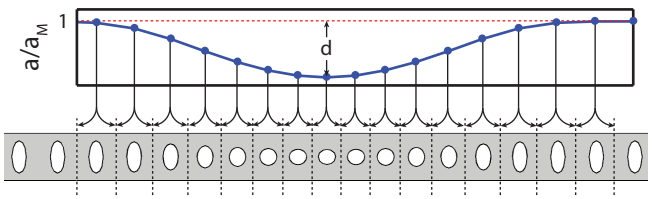

Figure 3.5: **Well function shape.** A candidate well function that smoothly transitions from a nominal unit cell width a_M to a defect unit cell width of $a_0 = a_M(1-d)$.

having defined $x \equiv j/M \in [0,1]$ for simplicity. A simple solution that conforms to the requirements above is $a(x) = 1 - d(2x^3 - 3x^2 + 1)$ (shown in Figure 3.5). We can further control the maximum slope by mapping

$$x \to y(x) = \begin{cases} \frac{1}{2}(2x)^\eta, & \text{if } x \leq 0.5, \\ 1 - \frac{1}{2}(2(1-x))^\eta, & \text{if } x > 0.5. \end{cases} \tag{3.53}$$

Thus, a nanobeam cavity design can be completely specified by the set of parameters (h_x, h_y, a_{nominal}, t, w, M, d, χ, ξ, η).

Finite element method (FEM) simulation of the entire structure is used to determine the cavity mode frequencies (ω_o and ω_m), optomechanical coupling rate, g (estimated using (3.28); see Appendix F), and radiation-limited optical quality factor, Q_o. To maximize g and Q_o, we assign each design a fitness value given by $F \equiv -g(\min\{Q_o, Q_{\text{cutoff}}\})^2$. In nanobeams, surface scattering effects typically limit quality factors to $\sim 10^6$, so we introduce a $Q_{\text{cutoff}} = 5 \times 10^6$ ceiling to prevent unrealizably high radiation-limited simulation Q_o values (occasionally $>10^8$) from unfairly weighting the fitness. We have here an 8 parameter optimization problem (since t is fixed by the choice of substrate and a_{nominal} is used to scale the fundamental optical cavity mode wavelength to between 1520 nm and 1570 nm) amenable to a variety of numerical minimization techniques. For a computationally expensive fitness function with a large parameter space, a good choice of optimization algorithm is the Nelder-Mead method [91, 92]. As a simplex search algorithm (as opposed to a gradient descent algorithm), it does not have smoothness requirements for the fitness function, and as a consequence, is also quite resistant to simulation noise. Conveniently, a modern variant of this method is already implemented in MATLAB's `fminsearch` function. Procedurally then, to create an optimized nanobeam design:

1. Choose a functional form for a_i, r_i and s_i parameterized by set of scalar parameters. In this case, we have (ξ, χ, η).

2. Randomly generate an initial parameter vector (h_x, h_y, w, M, d, χ, ξ, η).

3. Since the Nelder-Mead method is natively an unbounded search algorithm, we must ensure the

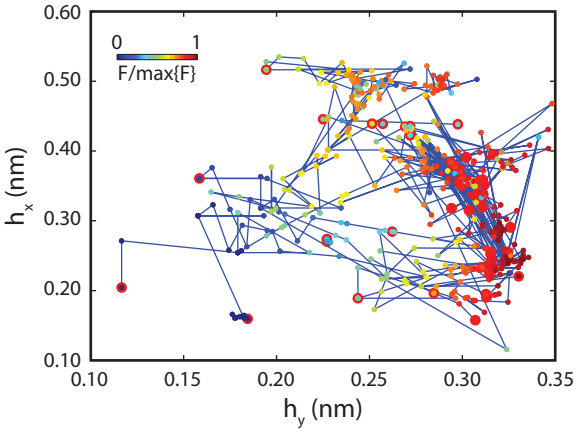

Figure 3.6: **Nelder-Mead simplex search path.** A slice of the multidimensional parameter space explored by the Nelder-Mead minimization method. The outlined points indicate randomized starting locations and the color of the point indicates the normalized value of the fitness function, F. We see a clear convergence to large values of F.

parameter vector is a realizable geometry by verifying that certain conditions are met (such as, but not limited to, requiring $(h_x, h_y) > (h_{x,\min}, h_{y,\min})$ to ensure the holes are above a certain size, $d \in (0, 1)$ to ensure the well function makes sense, and $h_y < w$ to ensure the holes are not larger than the beam width). If there are violated conditions, set $F = \infty$ and go to step 6.

4. Determine the a_{nominal} that gives a fundamental cavity optical mode frequency of approximately 1550 nm (nearly always possible in practice). If this fails, set $F = \infty$ and go to step 6.

5. Determine ω_o, ω_m, and g by simulation and compute the fitness of the design. If F has not changed appreciably over the last few iterations, we have reached a local minimum. We choose a new initial point by going to step 2.

6. Generate a new parameter vector via the Nelder-Mead method and go to step 3.

By continually reseeding the optimization algorithm, we mitigate the problem of converging on local minima. A visual representation of the search path is shown in Figure 3.6. We follow these steps until we have a design with a g and Q_o that we are satisfied with. This of course does not guarantee we have the *best* structure but it has, in practice, returned good results.

3.4.3 Mechanical Quality Factor

Unaddressed so far is the issue of mechanical losses in nanobeams, sources of which include the Akhieser mechanism, the Landau–Rumer mechanism, thermoelastic damping, and clamping losses

[93]. The overall mechanical quality factor is given simply by

$$\frac{1}{Q_{\text{total}}} = \frac{1}{Q_{\text{AK}}} + \frac{1}{Q_{\text{LR}}} + \frac{1}{Q_{\text{TE}}} + \frac{1}{Q_{\text{CL}}} + \cdots, \tag{3.54}$$

where each term can be modeled or computed individually for the nanobeam geometry.

Akhieser\Landau–Rumer Losses. The first two are phonon–phonon interaction theories describing the absorption of acoustic waves by the bulk material on differing length scales. Akhieser effects [94] are valid only for an acoustic wavelength much larger than the mean free path of the thermal phonons ($\lambda_m \gg \ell$, or equivalently in terms of acoustic frequency and thermal phonon lifetime, $\omega_m \tau \ll 1$). In this regime, acoustic phonons interact with ensembles of thermal phonons, perturbing them away from thermal equilibrium. The process of relaxing back to equilibrium via phonon-phonon collisions extracts energy from the acoustic wave and results in damping. On the other hand, the Landau–Rumer effects are valid only for $\omega_m \tau \gg 1$, where acoustic phonons interact with individual thermal phonons, operating primarily on the principle of three-phonon interactions [95]. In silicon, we can estimate the thermal phonon lifetime as [96]

$$\tau = \frac{3\kappa}{C_V c_s^2}, \tag{3.55}$$

where κ is the thermal conductivity, C_V is the volumetric specific heat at constant volume, and c_s is averaged longitudinal and shear wave velocities (see Appendix E for temperature dependent values). This corresponds to $\omega_m \tau = 1$ at $T \approx 100$ K, separating the two regimes. The absorption coefficients for these two effects are given by [97]

$$\alpha = \begin{cases} \dfrac{\pi \gamma^2 \omega_m^2 C_V T \tau}{3\rho c_s^3}, & \text{if } \omega_m \tau \ll 1 \quad \text{(Akhieser)}, \\ \dfrac{\pi \gamma^2 \omega_m C_V T}{4\rho c_s^3}, & \text{if } \omega_m \tau \gg 1 \quad \text{(Landau-Rumer)}, \end{cases} \tag{3.56}$$

where γ is the average Grüneisen coefficient [98] and ρ is the density. The quality factor may be estimated from this as $Q = \omega_m / 2\alpha c_s$.

Thermoelastic Damping. We now consider a more macroscopic model of intrinsic material damping. The compression (and rarefaction) of material under cyclic stress causes local heating (and cooling), leading to temperature gradients. The resultant heat flow is an entropy increasing process, resulting in net energy loss [99]. As the name suggests, it arises from a coupling between the temperature field, T, and the vector displacement field, $\boldsymbol{Q}$, given for an isotropic, homogeneous

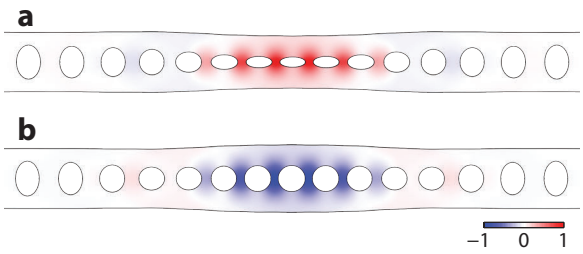

Figure 3.7: **Thermoelastic damping simulation.** Thermomechanical FEM simulations for the 4 GHz mechanical breathing mode at 300 K. The normalized thermal profile is plotted for **a**, 0, and **b**, π phase shifts.

material, by [100]

$$\rho \frac{\partial^2 \boldsymbol{Q}}{\partial t^2} = \nabla^T \boldsymbol{C}(\nabla \boldsymbol{Q} - \alpha T \boldsymbol{I}), \tag{3.57}$$

$$C_V \frac{\partial T}{\partial t} = \kappa \nabla^2 T - T_0 \frac{\partial}{\partial t} \alpha \mathrm{Tr}\left\{\boldsymbol{C} \nabla \boldsymbol{Q}\right\}, \tag{3.58}$$

where (3.58) is the heat balance equation,

$$T \frac{\partial S}{\partial t} = \kappa \nabla^2 T \tag{3.59}$$

linearized about some reference temperature, T_0,

$$S = C_v \log\left(\frac{T}{T_0}\right) + \alpha \mathrm{Tr}\left\{\boldsymbol{C} \nabla \boldsymbol{Q}\right\} \tag{3.60}$$

is the entropy per unit volume for a linear thermoelastic solid, α is the coefficient of thermal expansion, κ is the thermal conductivity, and $\boldsymbol{C}$ is the stiffness tensor. This pair of coupled partial differential equations can be solved numerically in COMSOL for a particular nanobeam geometry to determine the thermoelastic loss rate and corresponding quality factor (Figure 3.7).

Clamping Losses. Lastly, we consider losses attributed to acoustic energy leaking into the substrate via the clamping points of the nanobeam. The Bragg region of the nanobeam provides exponential attenuation of modes within the bandgap so naively one might expect to be able to make this loss vanishingly small simply by extended the number of mirror periods. We recall however that we only have a quasi-bandgap, so the small, symmetry-breaking defects introduced in the fabrication process couples the confined cavity mode to the unconfined modes of alternate symmetries, leading to energy leakage regardless of the number of mirror periods. We can model this effect in COMSOL by randomly offsetting the holes of the nanobeam by some amount specified by a normal distribution with 0 mean and δd standard deviation, and measuring the energy radiated at the clamping point

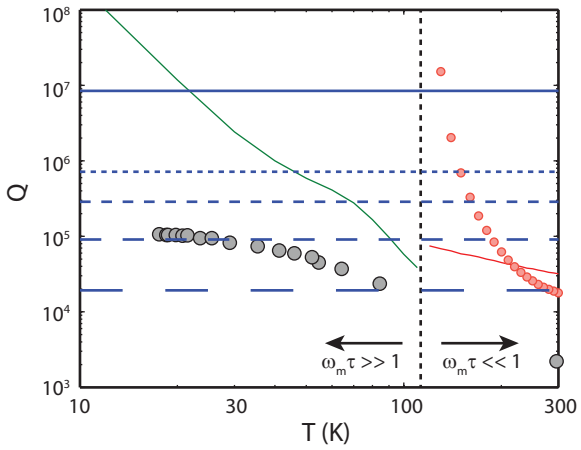

Figure 3.8: **Temperature dependence of mechanical losses.** Various contributions to the total mechanical Q_m for an 4 GHz mechanical breathing mode as a function of temperature. The black dashed line separates the plot into the Akhieser and Landau–Rumer regimes, with respective quality factor contributions, Q_{AK} (red line) and Q_{LR} (green line). The thermoelastic damping limited quality factor, Q_{TE}, is indicated using red ○'s, and the solid blue and increasingly spaced dashed blue lines indicates estimated clamping loss limited quality factors, Q_{CL}, for δd of 0 nm, 1 nm, 2 nm, 4 nm, and 8 nm. We have additionally included experimentally measured Q_m values of a phonically shielded nanobeam for comparison (black ○), suggesting the presence of alternative dominant loss factors.

per oscillation cycle.* By repeating this simulation a large number of times for different values of δd, we can estimate the Q due to these losses.

Once an optimized nanobeam design using the procedure from Section 3.4.2 is produced, we can estimate the losses for that particular geometry as a function of temperature. The individual theoretical contributions from each loss source for a 4 GHz mechanical breathing mode are plotted in Figure 3.8. We see that at room temperature (300 K), losses due to Akhieser effects, thermoelastic damping and clamping effects compete as the dominant loss mechanism. At low temperatures (<30 K), it is clear that theoretically, clamping losses dominate. While intrinsic material losses are difficult to circumvent, clamping losses are entirely geometry dependent and can be mitigated with clever design. We might consider choosing a different unit cell design or mechanical mode such that the mirror region has a complete mechanical bandgap. In practice, this is too restrictive of a requirement in quasi-1D structures and it is very difficult to find an appropriate optical and mechanical mode pair. A much simpler solution is to surround the nanobeam in a patterned silicon membrane with a complete phononic bandgap, strongly confining acoustic energy to the beam. The 2D "cross" phononic crystal design [62] has previously demonstrated this to great effect [63], and the wide tunability of the gap essentially allows the mechanical loss engineering to be decoupled from the nanobeam design. By carefully choosing c_a, c_h and c_t in the 2D unit cell (Figure 3.9a), it

*The procedure for mechanical Q simulation is outlined in detail in [59].

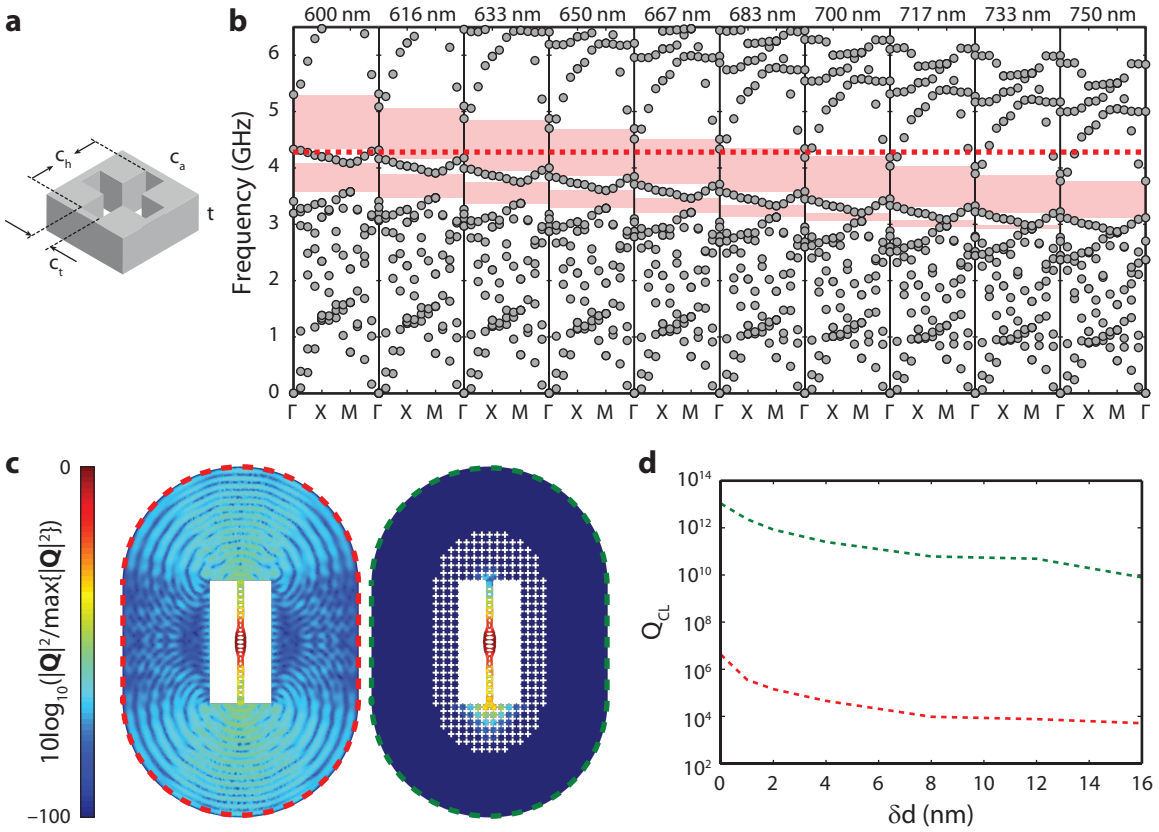

Figure 3.9: **Modeling the phononic shield and clamping losses.** **a**, The unit cell of the 2D phononic crystal that, for properly chosen set of geometry parameters (c_a, c_h, c_t, t), will act as a phononic shield for the mechanical mode at ω_m. **b**, Band diagrams for the phononic shield unit cell highlighting the tunability of the band gap (light red) as a function of c_a, with $t = 220$ nm, $c_t = 0.25c_a$, and $c_h = 0.85c_a$. The mechanical mode frequency, ω_m, is represented with the red dashed line, indicating $c_a = 650$ nm is a good choice for the unit cell size. **c**, FEM simulation of the normalized squared displacement field (proportional to mechanical energy) for a structure with and without a phononic shield, with the latter suppressing radiative energy by >100 dB. **d**, A comparison of quality factors from clamping loss simulations as a function of random perturbation amplitude, δd, as outlined in the text, with (green dashed) and without (red dashed) a phononic shield.

can be seen from Figure 3.9b that the complete phononic bandgap can be tailored to be centered on ω_m. With an appropriate shield in place, we repeat the clamping loss simulations outlined above and see a 6 order-of-magnitude improvement on Q_{clamping} (Figure 3.9c–d).

We experimentally measure the Q_m values in shielded devices as a function of local device temperature and draw a comparison to the theoretically predictions (black ○'s in Figure 3.8). That the measured quality factors are a order of magnitude lower than the theoretically dominant loss in all temperature regimes suggest additional mechanism for mechanical dissipation. The large variation in mechanical Q_m resulting from different surface treatments (as we will see in Section 4.3) suggests that the surface quality of the device plays a significant but difficult to model role in

	G1 [56, 57]	G2 [59, 60]	**5G** [52]	5GHF [101]
$\omega_m/2\pi$	10 MHz	2 GHz	**4.2 GHz**	5.7 GHz
Q_o	10^4–10^5	4×10^4	$\mathbf{1.1\times10^6}$	1.2×10^6
Q_m	10^2 (air) 10^3 (vacuum)	10^3 (air) 10^4 (10 K)	$\mathbf{3\times10^3}$ **(air)** $\mathbf{1.1\times10^5}$ **(20 K)**	3×10^3 (air) 6.8×10^5 (10 K)
$f_m\cdot Q_m$	10^{10}	10^{13}	$\mathbf{3.9\times10^{14}}$	3.5×10^{15}
$\lvert g\rvert/2\pi$ (meas.)	600 kHz	220 kHz	**900 kHz**	1.05 MHz
$\lvert g\rvert/2\pi$	–	150 kHz	**500 kHz**	780 kHz
$g_{\mathrm{mb}}/2\pi$	–	−380 kHz	**−400 kHz**	−90 kHz
$g_{\mathrm{pe}}/2\pi$	–	530 kHz	**900 kHz**	870 kHz
m_{eff}	40 pg	330 fg	**311 fg**	127 fg
x_{zpf}	5.1 fm	3.4 fm	**2.7 fm**	3.4 fm

Table 3.2: **Summary of device designs.** Summary of device designs and associated backaction cooling related parameters listed in chronological order (from left to right). All values are simulation values except for $|g|/2\pi$ (meas.), Q_o, Q_m, and $f_m\cdot Q_m$ where we have listed the highest experimentally realized value at room temperature and pressure (unless otherwise indicated). Optical mode frequencies, $\omega_o/2\pi$, for all devices are nominally 1.94 THz (free space wavelength of 1550 nm).

mechanical losses. In terms of engineering device geometry, the best we can currently do then is mitigate clamping losses as much as possible with the use of phononic shields, and take careful steps during fabrication to prepare the device surface.

3.5 Nanobeam Designs

Summarized in Table 3.2 are the nanobeam devices designed in the Painter group in the last several years, with associated backaction cooling parameter values. The optimization technique discuss above was applied to designing 5G (accounting only for g_{mb}) and 5GHF devices (accounting for both g_{mb} and g_{pe}), seeing a significant improvement on G2 nanobeam device parameters, designed by heuristic parameter space searching.

One feature of note is that g_{mb} and g_{pe} have opposing signs for the chosen pair of optical and mechanical modes. Running the optimization procedure results in a solution that minimizes the magnitude of one and maximizes the magnitude of other, and suggests that they cannot be made to add for the selected pair of modes. A pair of modes where these optomechanical couplings are of the same sign then, may have drastically improved SNR and cooling efficiency, both scaling as the square of g (from (2.64) and (2.57)).

In Chapter 4 and Chapter 5 we focus on the 5G design (5GHF was developed after the ground state cooling experiment). FEM simulations for this design are summarized in Figure 3.10.

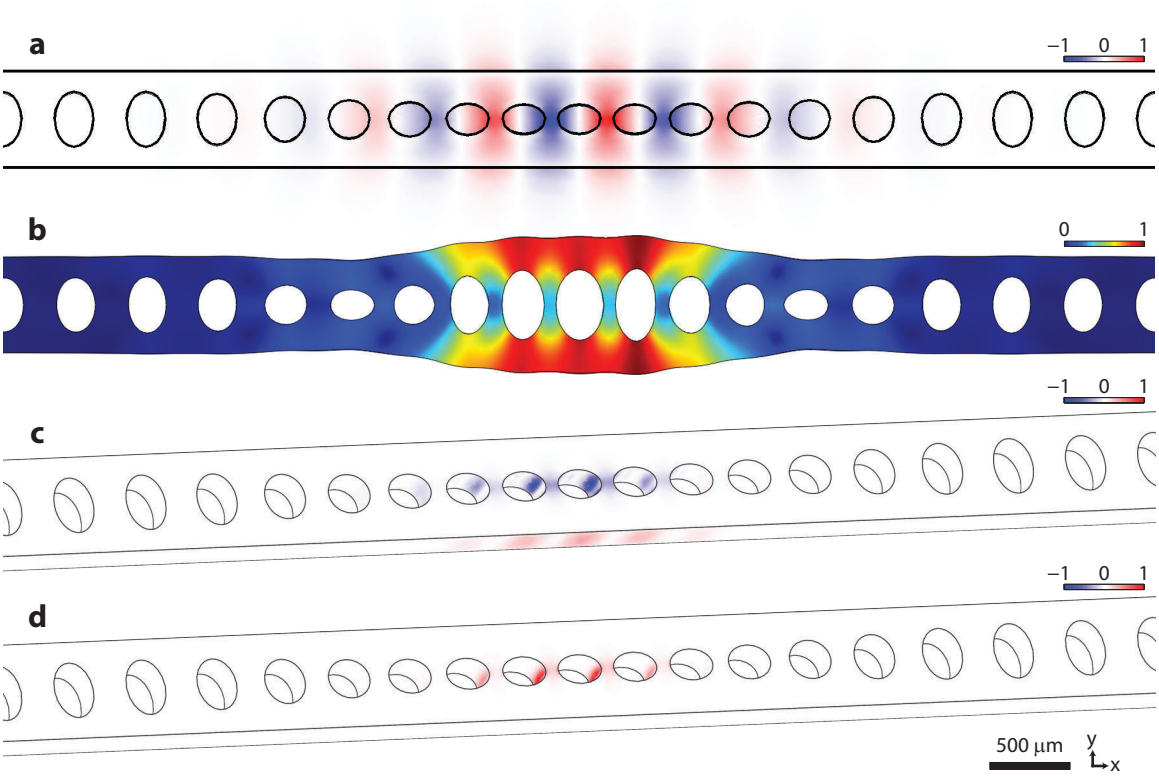

Figure 3.10: **FEM simulations of the 5G design.** FEM simulations corresponding to the normalized **a**, E_y field of the fundamental optical mode, **b**, displacement field, $|\boldsymbol{Q}|/\max\{|\boldsymbol{Q}|\}$, of the fundamental breathing mode, **c**, surface integrand in (3.39), showing the individual contributions to g_{mb}, and **d**, volume integrand in (3.47), showing the individual contributions to g_{pe}.

Chapter 4

Fabrication

In both the Painter group and the scientific community at large, a significant amount of effort has been spent developing silicon processing techniques and determining the role of surface chemistry in maintaining high quality factor optics and mechanics [66, 67, 102–104]. As such, we will only briefly discuss the procedure for fabricating 5G devices.

4.1 Lab Procedure

The basic fabrication steps for 5G devices are enumerated here (summarized in Figure 4.1). Figure 4.2 shows scanning electron microscope (SEM) images of a typical 5G device ready for optical and mechanical characterization.

1. The nanobeams are fabricated using a silicon-on-insulator (SOI) wafer from SOITEC (resistivity, ρ, of $4-20\ \Omega \cdot \mathrm{cm}$, device layer thickness, t, of 220 nm, (100) crystal orientation, and buried-oxide layer thickness of 3 μm). Typically, we work with diced chips either 1 cm × 1 cm or 1 cm × 0.5 cm in size which we initially clean with a solvent rinse train ordered by decreasing molecular weight: trichloroethylene (C_2HCl_3, abbreviated TCE), acetone (C_3H_6O), ethanol (C_2H_6O), then finally, deionized (DI) water (H_2O).

2. A resist layer of ZEP-520A is spun onto the chip (5,000 rpm, 60 s) and then baked (180°C, 20 minutes).

3. The cavity geometry is defined by electron beam lithography, then developed using ZED-N50 (150 s) and rinsed with ZMD-D (20 s).

4. We use inductively-coupled-plasma reactive ion etching (ICP-RIE) to transfer the pattern through the 220 nm silicon device layer.

5. The resist layer is removed using a heated TCE solution (50°C, stirred at 250 rpm) and a solvent rinse, followed by a Piranha clean (600 s, stirred at 250 rpm). The latter is prepared

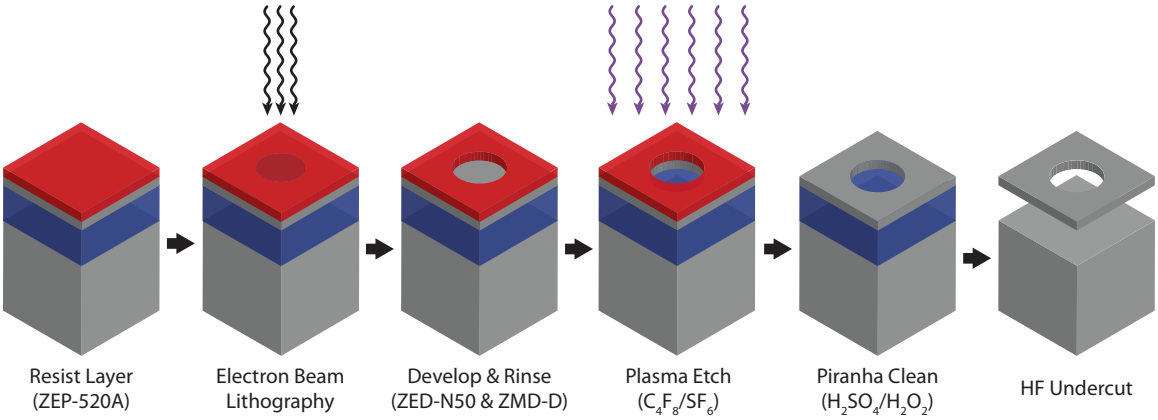

Figure 4.1: **Silicon-on-insulator device fabrication.** Diagrammatic representation of the 5G device fabrication procedure.

by combining sulfuric acid (H_2SO_4) and hydrogen peroxide (H_2O_2) in a 3:1 ratio at 75°C, and is finished with a DI water bath (30 s × 2).

6. The buried oxide layer is removed using a 1:1 hydrofluoric acid (HF) to DI water (H_2O) solution (90 s), followed by a DI water bath (30 s × 2).

7. The device surface is prepared by performing a Piranha clean (600 s, stirred at 250 rpm), followed by hydrogen termination using a weak 1:20 HF:H_2O solution (60 s) and a final DI water bath (30 s × 2). This is repeated as many times as necessary.

4.2 Lithography Adjustments

In the fabrication procedure, there are three different sets of feature dimensions:

- the designed (and desired) dimensions.
- the lithographic dimensions. These are the dimensions defined in the lithography pattern. Typically the beam widths are wider and the holes are smaller to account for blowout effects from the fabrication procedure.
- the realized dimensions. These are the dimensions of the fabricated nanobeam, and do not always match the desired dimensions.

A lithography pattern defined with the same feature dimensions as the nanobeam design tends to produce holes that are slightly larger than desired and a beam width that is slightly thinner than desired. We adjust the lithographic feature dimensions by utilizing MATLAB's image processing

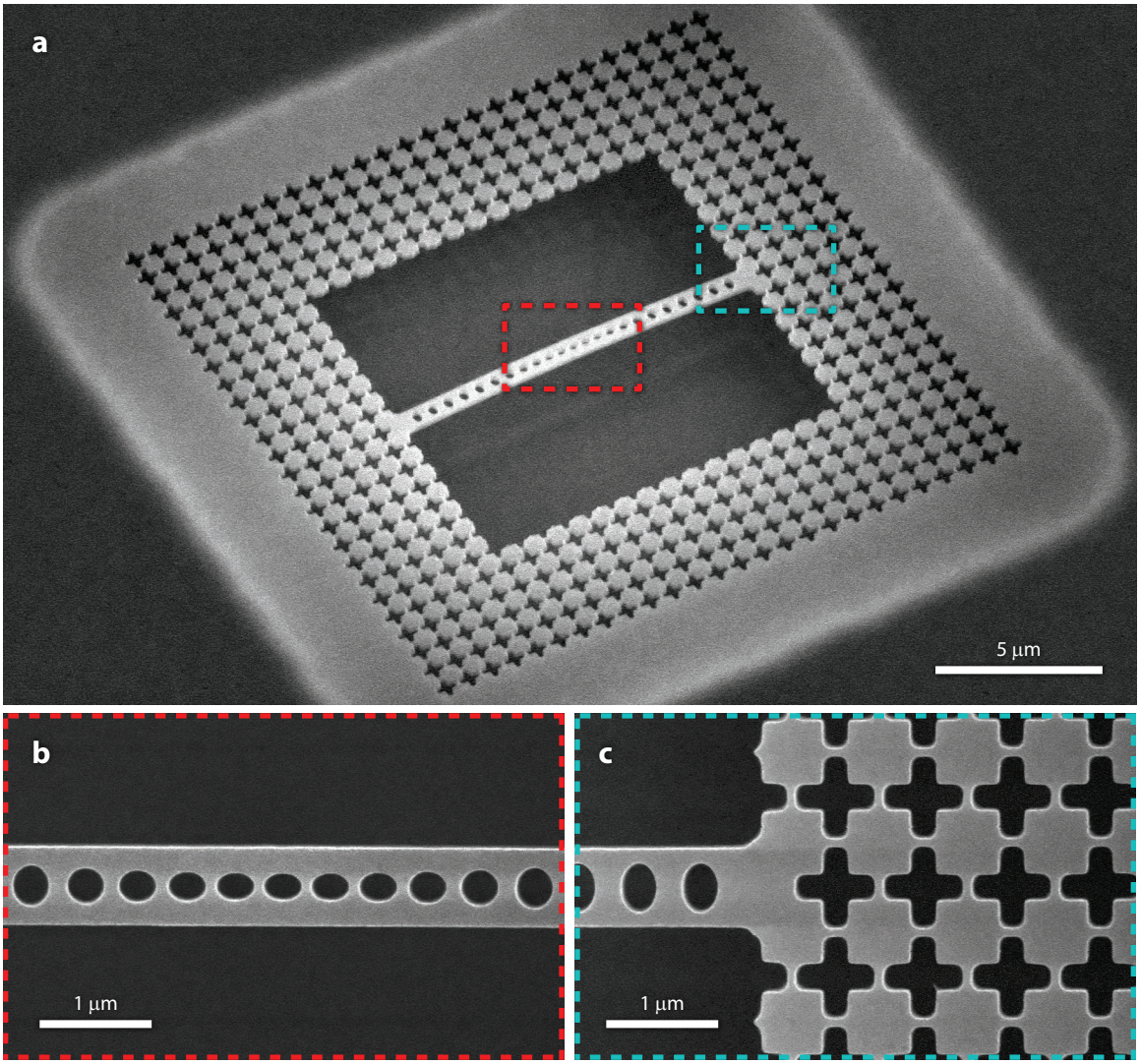

Figure 4.2: **Scanning electron microscope image of a 5G device.** **a**, Wide, angled view of a 5G device showing a suspended silicon nanobeam surrounded by a phononic shield to mitigate clamping losses. The lighter region around the crosses is the undercutting of the buried oxide layer. **b**, A zoomed view of the nanobeam cavity region. **c**, A zoomed view of the phononic shield region.

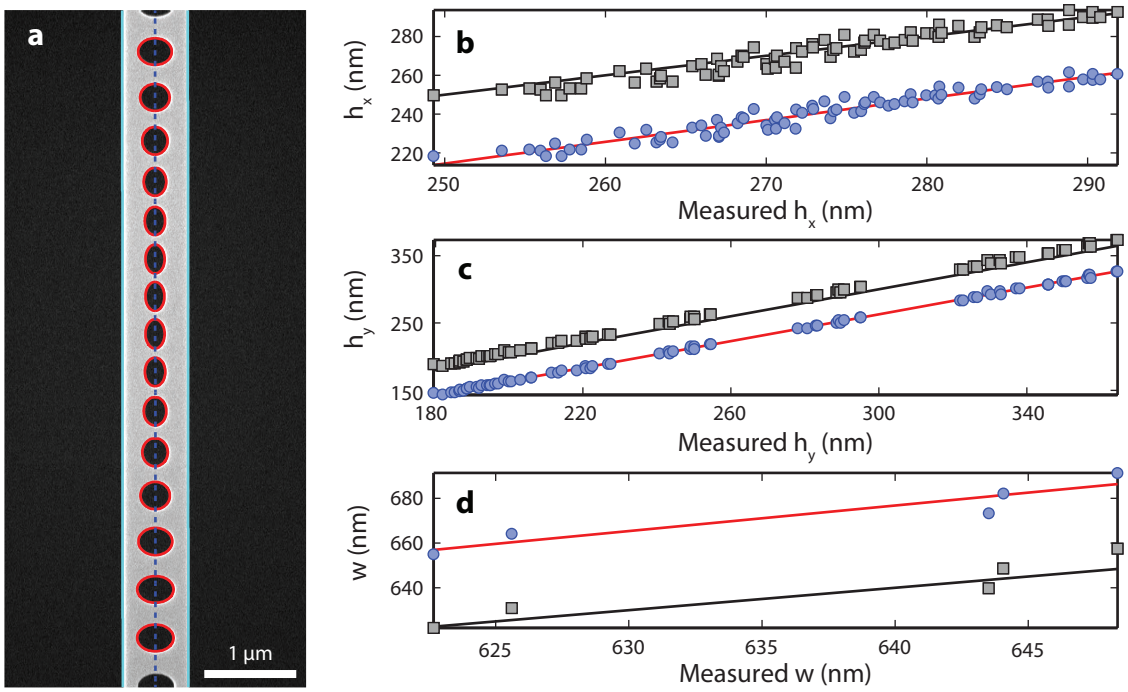

Figure 4.3: **Lithography parameter adjustment. a**, A scanning electron microscope (SEM) image of a fabricated 5G nanobeam with MATLAB measured feature dimensions overlayed. **b**–**d**, The measured h_x, h_y, and w feature dimensions plotted against the desired (black □'s) and lithographic (blue ○'s) feature dimensions. The red line is the mapping between the realized dimensions and the lithographic feature dimensions, and the black line shows how close the realized dimensions are to the correct sizes. We see that this particular nanobeam is nearly ideal.

functions to analyze scanning electron microscope (SEM) images of the fabricated nanobeams (Figure 4.3a), producing a mapping between the lithographic feature dimensions and the realized feature dimensions. Inverting this function (Figure 4.3b–d) and inputting the desired feature dimensions should then yield a lithography pattern that results in fabricated nanobeams of the correct size. In practice, if the ICP-RIE is stable, one or two iterations of this procedure is sufficient.

4.3 Silicon Surface Passivation

The surface chemistry of silicon plays a large role in limiting both the optical and mechanical quality factor of microscale devices through nonlinear absorption processes (via two-photon absorption and free carrier absorption, proportional to free carrier lifetime [67, 105–108]) and scattering losses (via surface roughness [66, 67]). This is especially true in nanobeams, given the large surface-to-volume ratio due to the patterning and elongated aspect ratio.

The final step in the procedure above was originally chosen since Piranha/HF cycles have been shown to significantly decrease free carrier lifetimes, as well as smoothing the surface and eliminating

Surface Treatment	Q_o (air)	Q_m (air)	Q_o (cryo)	Q_m (cryo)
O_2 + N_2 Anneal (∼10 nm SiO_2)	900,000	1,600	550,000	2,600
O_2 + N_2 Anneal (<1 nm SiO_2)	800,000	2,400	600,000	7,200
N_2 Anneal	750,000	3,700	500,000	140,000
HF Dip	**1,100,000**	**3,300**	**660,000**	**160,000**

Table 4.1: **Summary of surface treatments.** Impact of various surface treatments on quality factor at room temperature and pressure, and for cryogenic conditions. Listed optical quality factors measure intrinsic loss. The N_2 anneals were performed at 1,000°C and 1 atm, for 3 hours with 1 ramp down (following [67]). The growth rate of amorphous silicon oxide is estimated for dry oxygen annealing at 1,000°C and 1 atm using [115].

defects by repeatedly removing monolayers from the surface [109]. While effective at room temperature and pressure, the process does not prevent native oxide growth [110] and is not stable over time. Furthermore, accelerated degradation is observed during the transition to vacuum ($<3\times10^{-7}$ mbar) and cryogenic conditions (<30 K).

Alternative surface treatments following [109] were explored to mitigate this, with results shown in Table 4.1. The dry oxygen anneal, designed to improve surface stability, resulted in drastically decreased mechanical quality factors, likely related to two level systems (TLS) [111, 112] and anharmonicity [113] present in amorphous materials. Plain nitrogen annealing has been shown to reduce surface scattering due to roughness in proportion to the annealing time [114] (and the measured quality factors reflect this), but resulted in unstable fluctuations in both the mechanical and optical mode at cryogenic conditions that were difficult to explain. In the end, the most effective solution was to perform a 1:20 HF:H_2O dip for 60 s immediately (or as soon as possible) before cooling, which presumably maximizes the "protective" effect of the hydrogen termination.

Chapter 5

Ground State Cooling

With the theoretical framework and device design methodology developed in the previous sections, we now focus on the experimental procedure for backaction cooling the mechanical breathing mode of a 5G device to below unity phonon occupation. From (3.1), it is clear that precooling the device is immensely helpful in achieving this. Making use of a continuous flow, liquid helium (LHe) cryostat, we can bring the initial phonon population down to $\sim 10^2$ (instead of $\sim 10^3$ at room temperature). In cryogenic conditions, the device can be characterized to infer the values of κ, κ_e, and γ_i. With careful calibration of the laser power arriving at the optical cavity, the optomechanical coupling rate, g, can be inferred in two ways: via the broadening of the transparency window in the electromagnetically induced transparency (EIT) reflection spectroscopy, and via the broadening of the mechanical mode peak in the power spectral density (PSD) of the optical signal amplitude measured on a high speed detector connected to a real-time spectrum analyzer (RSA). Calibration of the optical and electronic gains of the components after the optical cavity also allows the phonon occupation, $\bar{n}$, of the mechanical mode to be extracted from the RSA trace—mechanical mode thermometry. Maintaining a laser frequency detuning, Δ, from the optical cavity mode of a mechanical frequency, ω_m, we then slowly increase the drive power while monitoring $\bar{n}$ until it is below unity, indicating the mechanical mode is spending most of its time (>50%) in the quantum ground state. The proceeding detailed discussion of this experiment is adapted from [52].

5.1 Experimental Setup

The detailed experimental setup used to measure the cooling spectra and the electromagnetically-induced transparency (EIT) window of the optomechanical crystal (OMC) is shown in Figure 5.1. A detailed listing of equipment and related model numbers is shown in Appendix D.1. The setup is designed measure both the EIT-like reflected signal and the transmission signal of the laser used to cool the mechanical system (though not simultaneously). It can also be configured via the optical switches (SWn, with control circuit described in Appendix D.2) for calibration and device

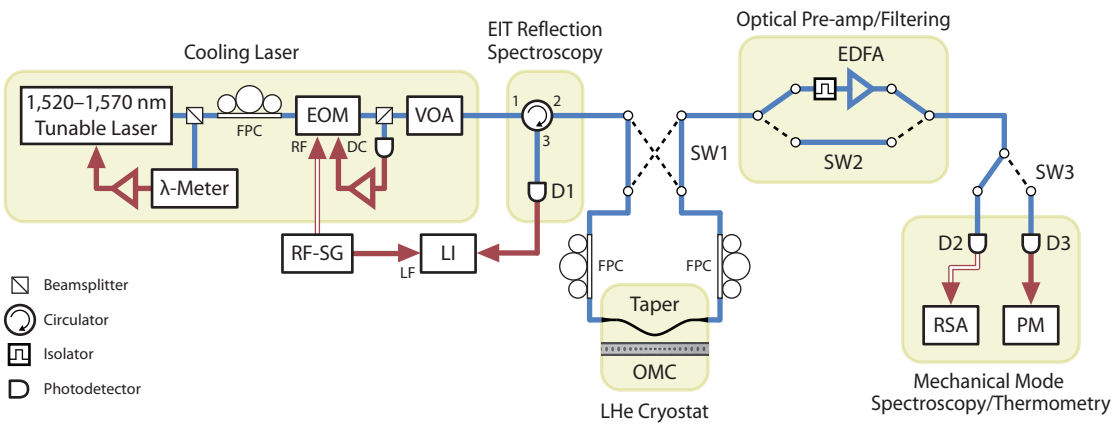

Figure 5.1: **Detailed experimental setup.** Full backaction cooling setup including switched optical paths (via optical switches, SWn). Blue lines indicate the optical path for the cooling measurement ("0" position of the optical switches), while the dashed black lines indicate alternative switched paths for calibration and characterization (the "1" position of the optical switches). The red lines indicate low-frequency (<1 MHz) electrical signals and the red–white lines indicate high-frequency (>1 GHz) electrical signals. A detailed explanation of the setup can be found in the text. The equipment key can be found in Table D.1.

characterization.

As a coherent light source we use a fiber-coupled, near-infrared laser, tunable across a wavelength range spanning approximately 50 nm centered around 1,545 nm, which has its intensity controlled by a variable optical attenuator (VOA). A small percentage (10%) of the laser intensity is sent to a wavemeter (λ-Meter) for passive frequency stabilization of the laser (frequency/detuning stabilization is outlined in Appendix D.4). A fiber polarization controller (FPC) is placed before the electro-optic amplitude modulator (EOM) to minimize polarization dependent losses. The amplitude modulator is driven by a microwave source (RF-SG) that generates a high-frequency RF signal. The RF signal itself is composed of an amplitude modulated carrier of frequency Δ_p, swept between 1 GHz and 8 GHz, modulated at the detection frequency of the lock-in amplifier (LI), ω_{LI} ($\sim$100 kHz). As a result, the amplitude modulation produces two probe sidebands at $\omega_\ell \pm \Delta_p$, each with a small amplitude modulation at the lock-in frequency.

A small portion of the signal from the amplitude modulator output (10%) is used as a DC control signal to keep the laser power constant, compensating for any low-frequency drift during the experiment. The remaining laser light is passed through a circulator, a 2×2 switch (SW1) (used to control the direction of the laser light through the device region), and a fiber polarization controller (FPC). The optical fiber then physically goes into a continuous flow, LHe cryostat, where it is fusion spliced [116] to a tapered and dimpled optical fiber (Taper) which has its position controlled with nanometer-scale precision (see Appendix D.5 for details of the Janis cryostat and related internal components). Coupling to the optomechanical crystal device is accomplished via the evanescent field

of this fiber probe [69, 70] (see Appendix D.6).

Switches 2 and 3 (SW2 and SW3) determine which path the light transmitted through the taper will follows. In the normal configuration (denoted by the solid blue path in Figure 5.1), the transmitted light is optically amplified by an erbium-doped fiber amplifier (EDFA) and then detected by a high-speed photodetector (D2) which is connected to a real-time spectrum analyzer (RSA) for spectral analysis. This optical amplification ensures the measured signal is above both the detector and RSA electronic noise floor. The alternative position of SW2 is used to calibrate the optical gain of the EDFA, and the nanosecond photodetector (D3) is used to measured the DC transmission response of the cavity. Additionally, the transmitted power is measured via a power meter (PM).

Any reflected signal coming from the taper/device is detected by a high-gain photodetector (D1) and its signal is sent to a lock-in amplifier (LI). The in-phase and quadrature signals from the lock-in are recorded for EIT reflection spectroscopy.

5.2 EIT Measurements

Here we will show how the amplitude modulation of the sidebands at $\omega_\ell \pm \Delta_p$ is used to measure an EIT-like reflected signal from the cavity. Using the model of an electro-optic amplitude modulator from Appendix D.3, the output field amplitude of the EOM can be written as

$$\begin{aligned} a_{\text{out}}(t) &= \frac{a_{\text{in}}(t)}{2}\Big((1 \pm i) \mp \beta\cos(\Delta_p t)\Big(1 + m_{\text{LI}}\cos(\omega_{\text{LI}}t)\Big)\Big) \\ &= \frac{a_{\text{in}}(t)}{2}\left((1 \pm i) \mp \frac{\beta}{2}\Big(\cos(\Delta_p t) + \frac{1}{2}\cos((\Delta_p + \omega_{\text{LI}})t) + \frac{1}{2}\cos((\Delta_p - \omega_{\text{LI}})t)\Big)\right), \end{aligned} \tag{5.1}$$

where $a_{\text{in}}(t) = \alpha_0 = \sqrt{P_{\text{EOM}}/\hbar\omega_\ell}$ is the input field amplitude to the EOM in a frame rotating at ω_ℓ, P_{EOM} is the input power to the EOM, β is the EOM modulation index (typically $\ll 1$), and ω_{LI} and m_{LI} are, respectively, the frequency and amplitude modulation index on the RF signal at Δ_p. For this experiment, we set $m_{\text{LI}} = 1$ and $\omega_{\text{LI}} \ll \Delta_p$. The reflected signal is filtered by the cavity dispersion. Considering the case where the pump is on the red side of the cavity ($\Delta > 0$) in the large detuning limit, and using the previously derived response functions of the cavity, (2.29) and (2.39), with the relation $r(\omega) = 1 - t(\omega)$, the reflected field is

$$a_{\text{refl}} = r(\Delta)\frac{\alpha_0}{2}(1 \pm i) \mp r_+(\Delta_p)\frac{\alpha_0\beta}{8}\left(e^{-i\Delta_p t} + \frac{1}{2}e^{-i(\Delta_p+\omega_{\text{LI}})t} + \frac{1}{2}e^{-i(\Delta_p-\omega_{\text{LI}})t}\right), \tag{5.2}$$

where we have assumed that $r_+(\omega)$ is approximately constant over $\Delta_p \pm \omega_{\text{LI}}$ (true for $\omega_{\text{LI}} < (\gamma_i + \gamma_{\text{OM}})/2$). The power incident on D1 in Figure 5.1 is thus

$$|a_{\text{refl}}|^2 \propto \text{D.C.} + |r_+(\Delta_p)|^2\frac{\alpha_0^2\beta^2}{32}\left(\cos(\omega_{\text{LI}}t) + \frac{1}{2}\cos(2\omega_{\text{LI}}t)\right) + \mathcal{O}(e^{i\Delta_p t}), \tag{5.3}$$

where we have ignored terms with frequency components $\gg \omega_{\mathrm{LI}}$ that are outside the detector bandwidth. The lock-in amplifier measures the in-phase (X) and quadrature (Y) components of the photodetector signal oscillating at ω_{LI}, so we have

$$X \propto |r_+(\Delta_p)|^2 \cos\phi, \tag{5.4}$$

$$Y \propto |r_+(\Delta_p)|^2 \sin\phi, \tag{5.5}$$

where ϕ is the phase difference between the photodetector signal and the reference oscillator in the lock-in amplifier. Adding X and Y in quadrature yields a signal amplitude $R(\Delta_p) \propto |r_+(\Delta_p)|^2$. For this experiment, we will see that the relevant information in the reflected signal is amplitude independent, so we are not too concerned with the proportionality constants.

If we vary Δ_p, we can identify two regimes of $R(\Delta_p)$: the "wide" regime where $|\Delta_p - \omega_m| > \gamma$, and the "narrow" regime where $|\Delta_p - \omega_m| \lesssim \gamma$. In the wide regime, we have

$$R(\Delta_p) \propto \frac{(\kappa_e/2)^2}{(\Delta - \Delta_p)^2 + (\kappa/2)^2}, \tag{5.6}$$

which is simply the steady state cavity frequency response, a Lorentzian signal from which we can extract both κ and the detuning of the laser from the optical cavity. In the narrow regime, if we assume $\Delta = \omega_m$ (that is, we are a mechanical frequency detuned, on the red side of the cavity), then in the sideband-resolved regime, we have

$$\begin{aligned} i(\Delta - \Delta_p) + \kappa/2 &= i(\omega_m - \Delta_p) + \kappa/2 \\ &\approx \kappa/2, \end{aligned} \tag{5.7}$$

so the lock-in amplifier signal is given by

$$\begin{aligned} R(\Delta_p) &\propto \frac{\kappa_e^2}{\kappa^2} \frac{(\omega_m - \Delta_p)^2 + (\gamma_i/2)^2}{(\omega_m - \Delta_p)^2 + \left(\frac{\gamma_i + \gamma_{\mathrm{OM}}}{2}\right)^2}, \\ &= \frac{\kappa_e^2}{\kappa^2} \left(1 - \frac{\gamma_{\mathrm{OM}}}{2} \frac{\gamma_i + \gamma_{\mathrm{OM}}/2}{(\omega_m - \Delta_p)^2 + \left(\frac{\gamma_i + \gamma_{\mathrm{OM}}}{2}\right)^2}\right), \end{aligned} \tag{5.8}$$

where we have substituted $|G|^2 = \kappa\gamma_{\mathrm{OM}}/4$ and used (A.23). This quantitatively describes the EIT transparency window induced by the interaction of the optical field with the mechanics, and is spectrally an inverted Lorentzian of width $\gamma = \gamma_i + \gamma_{\mathrm{OM}}$ with vanishing resonant reflection in the large cooperativity limit. We must note, however, that the previous assumption that $\omega_{\mathrm{LI}} < (\gamma_i + \gamma_{\mathrm{OM}})/2$ limits the smallest transparency window that can be measure to approximately the lock-in detection frequency. A detailed discussion of EIT induced by optomechanics can be found in [117, 118].

5.3 Mechanical Mode Thermometry

Equation (2.64) shows an explicit form for the spectral power in the mechanical sideband for a red-detuned pump laser, as seen by a perfect photodetector placed immediately at the output port of the optical cavity. If the input power to the cavity, $P_{\rm in}$, and the device parameters γ_i, κ, and κ_e were accurately known, such a measurement would allow the mechanical mode occupation, $\bar{n}$, to be inferred. In reality, photodetectors are neither perfect, nor so conveniently placed. More usefully, we can use this equation to relate the mechanical mode occupation to the measured power spectrum on the RSA in the experimental setup.

The signal analyzed by the RSA, $P_{\rm RSA}$, is related to the photodetector (D2) output voltage, $V_{\rm D2}$, by the electrical power relationship $P_{\rm RSA} = V_{\rm D2}^2/R_L$, where $R_L = 50\ \Omega$ is the input impedance of the RSA. This voltage is related to the incident optical power by some detector gain, $G_{\rm D2}$. This is then related to the power at the output port of the optical cavity by some system gain, which we can separate into gain provided by the EDFA, $G_{\rm EDFA}$, and system losses, G_o. Grouping the system losses together with the detector gain into a single, electronic gain term, $G_e \equiv G_{\rm D2}G_o$ (with units of volts per optical watt), we can relate the RSA-measured spectral power, $\widetilde{S_P}$, to (2.64) through

$$\widetilde{\bar{S}_P}(\omega) = \frac{G_e^2 G_{\rm EDFA}^2}{R_L}\bar{S}_P(\omega). \tag{5.9}$$

For $\Delta = \omega_m$, integrating this expression, and defining $\widetilde{P_{\omega_m}}$ as the integrated power spectral density near ω_m of the RSA-measured signal, and

$$P_{\omega_m} = \left(\hbar\omega_\ell|\alpha_{\rm in}|^2\right)\left(\frac{\kappa_e/2}{\Delta^2+(\kappa/2)^2}\hbar\omega_\ell|\alpha_{\rm in}|^2\right)\left(\frac{4g^2}{\kappa}\right)\left(\frac{\kappa_e}{\kappa}\right)\bar{n}, \tag{5.10}$$

as the average oscillating optical power close to ω_m (at the cavity), we get the relation

$$\widetilde{P_{\omega_m}} = \left(\frac{G_e^2 G_{\rm EDFA}^2}{R_L}\right)\left(\hbar\omega_\ell|\alpha_{\rm in}|^2\right)\left(\frac{\kappa_e/2}{\Delta^2+(\kappa/2)^2}\hbar\omega_\ell|\alpha_{\rm in}|^2\right)\left(\frac{4g^2}{\kappa}\right)\left(\frac{\kappa_e}{\kappa}\right)\bar{n}, \tag{5.11}$$

where we have subtracted off the flat background signal in $\bar{S}_P(\omega)$. Defined $\alpha_{\rm in} = \sqrt{n_{\rm in}} = \sqrt{P_{\rm in}/\hbar\omega_\ell}$, where $P_{\rm in}$ and $n_{\rm in}$ are respectively the input power and input photon flux to the optical cavity, and recalling that $|G|^2 = g^2 n_c = \kappa\gamma_{\rm OM}/4 = \kappa(\gamma-\gamma_i)/4$ for $\Delta = \omega_m$ in the sideband-resolved regime, we can then write the expression for the mechanical mode occupation in terms of all directly measurable values,

$$\bar{n} = \widetilde{P_{\omega_m}}\left(\frac{R_L}{G_e^2 G_{\rm EDFA}^2}\right)\left(\frac{1}{P_{\rm in}}\right)\left(\frac{1}{\hbar\omega_o}\right)\left(\frac{1}{\gamma-\gamma_i}\right)\left(\frac{\kappa}{\kappa_e}\right). \tag{5.12}$$

From (2.57), we can use the phonon number to get the bath temperature,

$$T_b = \frac{\hbar\omega_m}{k_B \log\left(\frac{\gamma_i}{\gamma\bar{n}} + 1\right)}. \tag{5.13}$$

To check the validity of this analysis, repeated measurements at room temperature were performed, yielding a measured T_b of $\sim 296 \pm 8$ K.

5.3.1 Calibration of Input Power

While the input/output optical power of the taper can be measured directly, the cavity input power, P_{in}, is additionally influenced by asymmetric losses in the taper resulting from coupling geometry. With this in mind, the 2×2 switch SW1 allows these losses to be characterized by switching the direction of the light through the taper. Labeling the two positions of the switch "0" and "1", the input powers to SW1, respectively P_0 and P_1, and the total insertion loss, L_{total}, can be measured directly. Optical transmission scans are then taken in both switch positions at high enough powers to induce optical bistability [68]. Given that the bistability shift of the optical mode, $\Delta\lambda_0$ and $\Delta\lambda_1$ for the two directions respectively, is proportional to the intracavity power, we have

$$\frac{P_0 L_0}{P_1 L_1} = \frac{P_{\text{in},0}}{P_{\text{in},1}} = \frac{\Delta\lambda_0}{\Delta\lambda_1}, \tag{5.14}$$

where L_0 and L_1 are the losses before the cavity, and $P_{\text{in},0}$ and $P_{\text{in},1}$ are the powers at the cavity, in the respective switch positions. Since $L_0 L_1 = L_{\text{total}}$, we can solve this system of equations and find

$$L_0 = \sqrt{\frac{P_1 \Delta\lambda_0}{P_0 \Delta\lambda_1} L_{\text{total}}}, \tag{5.15}$$

$$L_1 = \sqrt{\frac{P_0 \Delta\lambda_1}{P_1 \Delta\lambda_0} L_{\text{total}}}. \tag{5.16}$$

Thus, $P_{\text{in},0}$ and $P_{\text{in},1}$ can be determined for a fixed attenuation. During the measurement, the direction of the light through the taper is fixed so we choose one of the two to set as P_{in}. The linearity of the VOA then allows the power at the cavity to be inferred for any attenuation setting.

5.3.2 Calibration of EDFA Gain

The EDFA gain, G_{EDFA}, is measured by utilizing SW2 to insert and remove the EDFA from the optical train while measuring a fixed tone at the mechanical frequency, ω_m, generated by the EOM. The ratio of the integrated spectral power of the tones gives G_{EDFA}^2.

5.3.3 Calibration of Electronic Gain

To characterize the electronic gain, G_e, of detector D2, we first maximize the power incident on the detector (by reducing the attenuation on the VOA). We then measure the DC bias voltage $V_{\mathrm{DC}}^{(0)}$ (via the bias monitor port on D2) and verify that this voltage is identical to the DC voltage at the high-frequency port on D2, ensuring that $V_{\mathrm{DC}}^{(0)}$ accurately reflects the DC voltage measured by the RSA. Then, using switch SW3, the optical power incident on D3, $P_{\mathrm{D3}}^{(0)}$, was also measured. For each data point in the experiment (corresponding to a different attenuation), we measure the incident power on D3, P_{D3}. We have then

$$V_{\mathrm{DC}} = V_{\mathrm{DC}}^{(0)} \frac{P_{\mathrm{D3}}}{P_{\mathrm{D3}}^{(0)}}. \tag{5.17}$$

The purpose of the switching is a technical one; the dynamic range of our optical power meter is much larger than that of our voltmeter, allowing the DC bias voltage of the detector to be determined for any amplitude of optical signal. Since (2.64) is computed for optical power at the cavity, G_e must reflect the conversion of power at the cavity, P_{in}, to voltage at the detector, V_{DC}. We must have then $G_e = V_{\mathrm{DC}}/P_{\mathrm{in}}$ (for V_{DC} and P_{in} measured at the same attenuation). We note that this is not the gain typically quoted on a specification sheet; it encapsulates the optical insertion loss between the cavity and the detector in our experimental setup.

5.3.4 Optical Characterization

The normalized DC transmission spectra at detector D3, $T(\omega)$, is given by the squared magnitude of the cavity frequency response in (2.29),

$$\begin{aligned} T(\omega) &= \left| 1 - \frac{\kappa_e/2}{-i(\omega_o - \omega) + \kappa/2} \right|^2 \\ &= \frac{(\omega_o - \omega)^2 + (\kappa/2 - \kappa_e/2)^2}{(\omega_o - \omega)^2 + (\kappa/2)^2}, \end{aligned} \tag{5.18}$$

effectively a Lorentzian dip with a linewidth of κ and a normalized transmission on resonance (at $\omega = \omega_o$),

$$T_0 \equiv T(0) = \left(1 - \frac{\kappa_e}{\kappa}\right)^2. \tag{5.19}$$

The transmission contrast is given by $1 - T_0$. The optical parameters κ, κ_e, and ω_o can be determined by least squares fitting the measured normalized DC transmission spectra to the above functional form. We can also use EIT reflection spectra in the wide regime and (5.6) to determine κ.

5.3.5 Mechanical Characterization

The measured power spectral density on the RSA near ω_m, $\widetilde{S_P}(\omega)$, has a functional form given by (2.64). We can write this as

$$\widetilde{S_P}(\omega) = \frac{A}{\left(\frac{\omega_m - \omega}{\gamma/2}\right)^2 + 1}, \tag{5.20}$$

effectively a Lorentzian centered at ω_m, with a linewidth of γ, and amplitude A, where we have subtracted a spectral background taken with the cooling laser far-detuned from the cavity (with all other experimental conditions constant). The mechanical parameters, γ and ω_m, can be determined by least squares fitting. We can also use EIT reflection spectra in the narrow regime and (5.8) to determine both γ and ω_m when $\gamma > \omega_{\mathrm{LI}}$. We can compute the average oscillating power at ω_m, $\widetilde{P_{\omega_m}}$, using a modified form of (A.22),

$$\widetilde{P_{\omega_m}} = \frac{A\gamma}{4}. \tag{5.21}$$

To extract the intrinsic mechanical linewidth, γ_i, we first fix the input power P_{in}. We then lock the pump on the red side of the cavity (at $\Delta = +\omega_m$) and measure the total linewidth, $\gamma^{(\mathrm{red})} = \gamma_i + \gamma_{\mathrm{OM}}$. We repeat the measurement on the blue side (at $\Delta = -\omega_m$) with all other experimental conditions constant, where $\gamma^{(\mathrm{blue})} = \gamma_i - \gamma_{\mathrm{OM}}$. Using low input powers where $\gamma_{\mathrm{OM}} \ll \gamma_i$ to avoid amplification of the mechanical oscillations, we have

$$\gamma_i = \frac{\gamma^{(\mathrm{red})} + \gamma^{(\mathrm{blue})}}{2}. \tag{5.22}$$

5.3.6 Optomechanical Coupling Rate Characterization

For a fixed detuning $\Delta = \omega_m$, we can measure γ_{OM} as a function of P_{in} using either (5.21) or (5.8) (once γ_i is known). These two parameters are related by

$$\begin{aligned} \gamma_{\mathrm{OM}} &= \frac{4g^2}{\kappa} n_c \\ &= \left(\frac{\kappa_e/2}{\omega_m^2 + (\kappa/2)^2} \frac{1}{\hbar\omega_\ell} \frac{4g^2}{\kappa} \right) P_{\mathrm{in}}, \end{aligned} \tag{5.23}$$

where the optomechanical coupling rate, g, can be extracted from the slope.

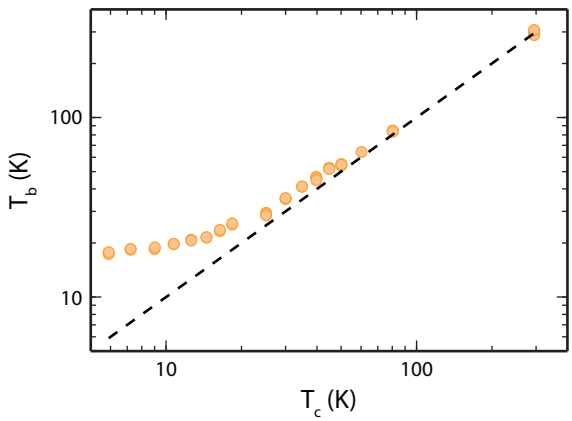

Figure 5.2: **Mechanical mode thermometry.** Plot of the measured (○) mechanical mode bath temperature (T_b) versus cryostat sample mount temperature (T_c). The dashed line indicates the curve corresponding to perfect following of the mode temperature with the cryostat temperature ($T_b = T_c$). We see a saturation of the sample temperature at 17.6 K.

5.4 Results

5.4.1 Bath Temperature Characterization

As discussed in Section 5.3, the calibration of the EDFA gain, along with the photoreceiver and real-time spectrum analyzer photodetection gain, allows one to convert the measured area under the photocurrent noise PSD into a mechanical mode phonon occupancy. These calibrations, along with low drive power measurements ($C \ll 1$) of both optical and RF spectra at $\Delta = \pm\omega_m$ detunings, provide an accurate, local thermometry of the optomechanical cavity. An application of this form of calibrated mode thermometry is shown in Figure 5.2, where we plot the optically measured mechanical mode bath temperature (T_b) versus the cryostat sample mount temperature (T_c; independently measured using a Si diode thermometer attached to the copper sample mount). As one can see from this plot, the optical mode thermometry predicts a mode temperature in good correspondence with the absolute temperature of the sample mount for $T_c > 50$ K; below this value the mode temperature deviates from T_c and saturates to a value of $T_b = 17.6 \pm 0.8$ K due to blackbody heating of the device through the imaging aperture in the radiation shield of our cryostat.

5.4.2 Device Characterization

In a first set of measurements under stabilized vacuum ($<3\times10^{-7}$ mbar) and cryogenic ($T_b = 17.6$ K) conditions, we follow Section 5.3.4 and 5.3.5 to measure the mechanical and optical properties of the system. The optical resonance was found to have $Q_o = 4 \times 10^5$, $\omega_o/2\pi = 195$ THz ($\lambda_o = 1{,}537$ nm), and resonant transmission contrast of 25%. This corresponds to $\kappa/2\pi = 488$ MHz and $\kappa_e/2\pi = 65$ MHz. The mechanical mode was found to have $Q_m = 1.06 \times 10^5$ and $\omega_m/2\pi = 3.68$ GHz. This

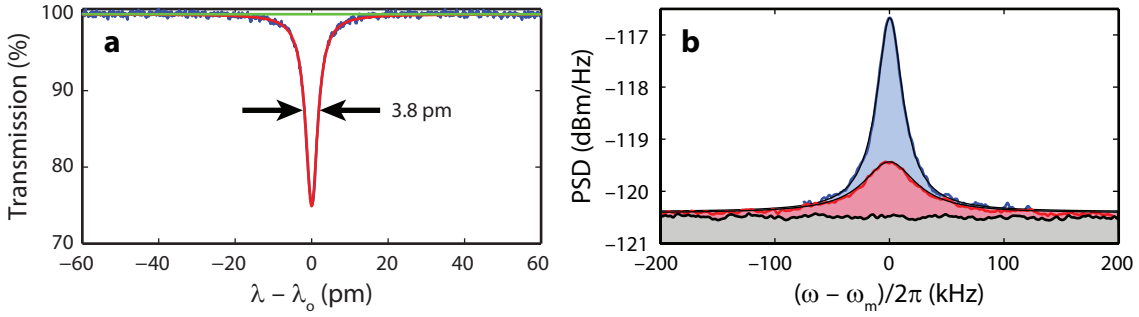

Figure 5.3: **Device characterization.** **a**, The normalized optical transmission spectrum measured on D3 from which κ, κ_e, and ω_o are extracted. **b**, The mechanical noise spectrum measured around the resonance frequency of the breathing mode, ω_m, at low laser drive power ($n_c = 1.4$), for $\Delta = +\omega_m$ (red) and $\Delta = -\omega_m$ (blue), from which γ_i can be inferred. The black trace corresponds to the measured noise floor (dominated by EDFA noise) with the drive laser detuned far from the cavity resonance.

corresponds to $\gamma_i/2\pi = 35$ kHz. The data for these measurements is presented in Figure 5.3. Typical measured noise power spectra under low power laser drive ($n_c = 1.4$, $C = 0.27$), for both red and blue detuning, are shown in Figure 5.3b. Even at these small drive powers the effects of backaction are clearly evident on the measured spectra, with the red-detuned drive broadening the mechanical line and the blue-detuned drive narrowing the line. The noise floor in Figure 5.3b (shaded in gray) corresponds to the noise generated by the erbium-doped fiber amplifier (EDFA) used to preamplify the transmitted drive laser signal prior to photodetection, and is several orders of magnitude above the electronic noise of the photoreceiver and real-time spectrum analyzer.

5.4.3 Backaction Cooling

In a second set of measurements, the mechanical damping, γ, and the cavity–laser detuning, Δ, can be measured by optical spectroscopy of the driven cavity. By sweeping a second probe beam of frequency $\omega_p = \omega_\ell + \Delta_p$ over the cavity, with the cooling beam tuned to $\Delta = \omega_m$, spectra exhibiting electromagnetically induced transparency (EIT) [117] are measured (shown in Figure 5.4b–d). Due to the high single-photon cooperativity in the system, an intracavity population of only $n_c \approx 5$ switches the system from reflecting to transmitting for the probe beam. The corresponding dip at the center of the optical cavity resonance occurs at a probe detuning $\Delta_p \equiv \omega_p - \omega_\ell = \omega_m$ and has a bandwidth equal to the mechanical damping rate, $\gamma = \gamma_i(1 + C)$. Figure 5.4a shows a plot of the measured mechanical linewidth versus intracavity photon number, displaying good correspondence between both mechanical and optical spectroscopy techniques, and indicating that the system remains in the weak-coupling regime for all measured cooling powers. From a fit to the measured mechanical damping rate versus n_c (dashed red line in Figure 5.4a), the zero-point-motion optomechanical coupling rate is determined to be $g/2\pi = 910$ kHz.

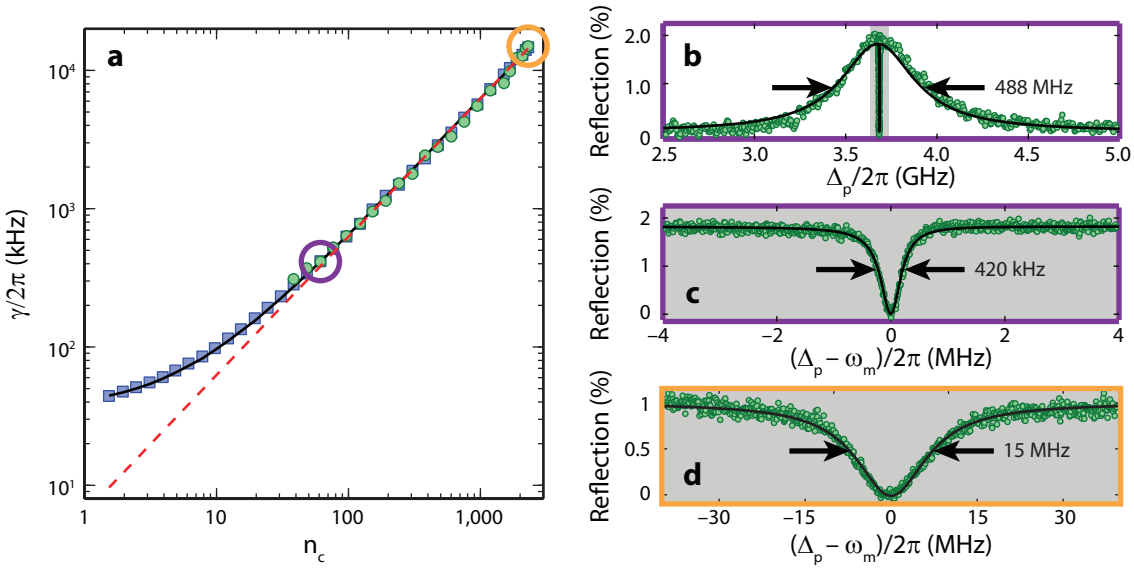

Figure 5.4: **EIT and optomechanical damping.** **a**, Measured mechanical mode linewidth (□) and EIT transparency bandwidth (○) (showing good correspondence, as expected), with a linear fit to $\gamma_{\rm OM}$ (red dashed line) to estimate the zero-point optomechanical coupling rate, g. **b**, Typical reflection spectrum of the cavity (normalized power reflection) while driven by the cooling laser ($\Delta = \omega_m$, $n_c = 56$, $C = 11$) as measured by a weaker probe beam at $\omega_p = \omega_\ell + \Delta_p$. The signature reflection dip on-resonance with the bare cavity mode is indicative of electromagnetically-induced transparency (EIT) caused by the coupling of the optical and mechanical degrees of freedom by the cooling laser beam. **c**, Zoomed view of the EIT transparency window region in **b**. **d**, Transparency window for the highest intracavity photon number, $n_c \approx 2{,}000$, with a transparency bandwidth of 15 MHz.

In Figure 5.5a we plot the calibrated Lorentzian noise PSD area, in units of phonon occupancy, versus red-detuned ($\Delta = \omega_m$) drive laser power. Due to the low effective temperature of the laser drive, the mechanical mode is not only damped but also cooled substantially. The minimum measured mode occupancy for the highest drive power of $n_c \approx 2{,}000$ is $\bar{n} = 0.85 \pm 0.08$, putting the mechanical oscillator in a thermal state with ground state occupancy probability greater than 50%. The dashed blue line in Figure 5.5a represents the ideal backaction cooled phonon occupancy estimated using both the measured mechanical damping rate in Figure 5.4a and the low drive power intrinsic mechanical damping rate. Deviation of the measured phonon occupancy from the ideal cooling model is seen to occur at the highest drive powers, and as detailed in Section 5.5, is due to both an increase in the bath temperature due to optical absorption (Figure 5.5d) and an increase in the intrinsic mechanical damping rate (Figure 5.5e) induced by the generation of free carriers through optical absorption. In order to evaluate the efficiency of the optical transduction of the mechanical motion, we also plot in Figure 5.5f the measured background noise PSD, or imprecision level. The minimum imprecision of our measurements (at $n_c \sim 500$) corresponds to $n_{\rm imp} \approx 20$ in units of phonon quanta when referred to the peak Lorentzian level of the transduced mechanical motion

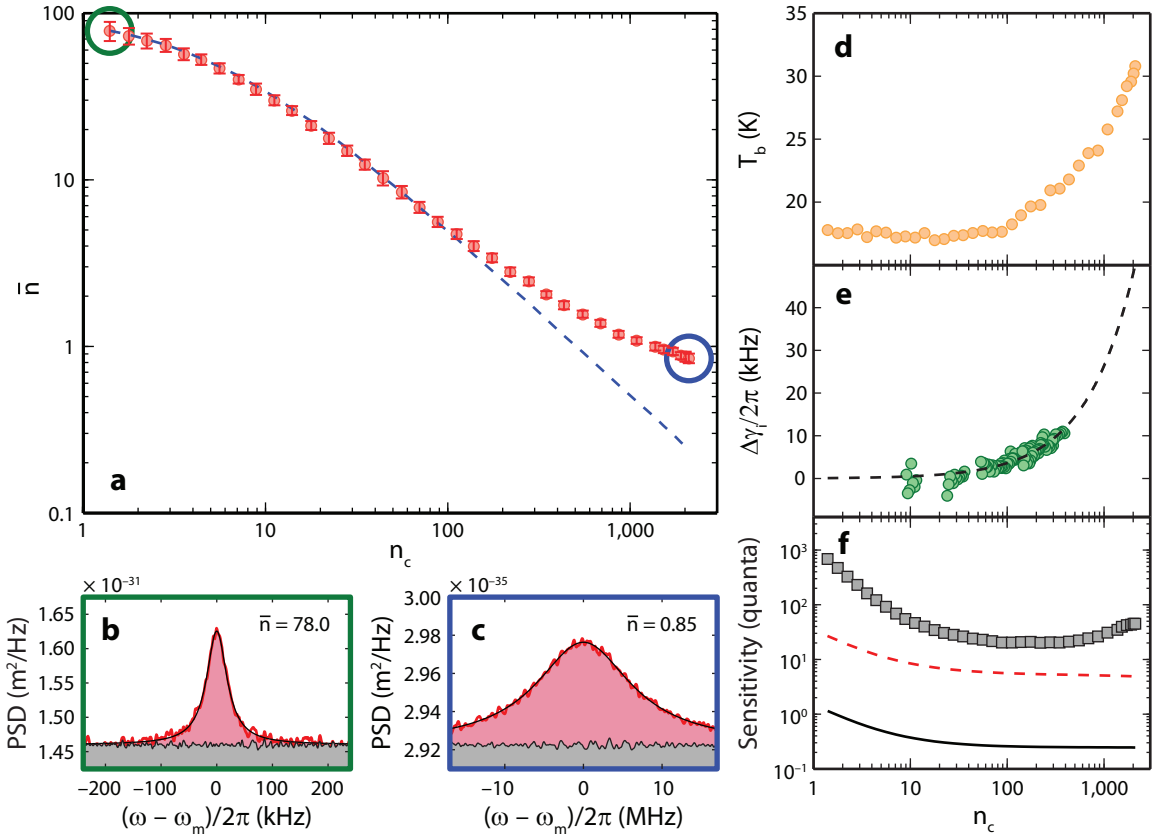

Figure 5.5: **Optical cooling results.** **a**, Measured (○) average phonon number, $\bar{n}$, in the breathing mechanical mode at $\omega_m/2\pi = 3.68$ GHz versus cooling laser drive power (in units of intracavity photons, n_c), as deduced from the calibrated area under the Lorentzian lineshape of the mechanical noise power spectrum, $\widetilde{S}_P$. The dashed blue line indicates the estimated mode phonon number from the measured optical damping alone. Error bars indicate estimated uncertainties as outlined in Section 5.4.4. **b** and **c**, The measured noise power spectrum in units of m^2/Hz (using $x_{\mathrm{zpf}} = 2.7$ fm, corresponding to the numerically computed motional mass for the breathing mode of $m_{\mathrm{eff}} = 311$ fg) at low and high laser cooling power, respectively. **d**, Estimated bath temperature, T_b, versus cooling laser intracavity photon number, n_c. **e**, Measured change in the intrinsic mechanical damping rate versus n_c (○). A polynomial fit to the mechanical damping dependence on n_c is shown as a dashed line. For more detail see Section 5.5. **f**, The measured (□) background noise PSD versus laser drive power (n_c), in units of effective phonon quanta. The plotted red dashed curve corresponds to the theoretical imprecision assuming shot-noise-limited detection, but all other cavity properties and optical loss as in the experiment. The solid black curve is for an ideal, quantum-limited continuous position measurement of mechanical motion.

(see Section 5.7). Comparing the measured imprecision to the theoretical imprecision for shot-noise-limited detection (dashed red curve) and ideal quantum-limited motion transduction (black curve), indicates that $n_{\mathrm{imp}}^{\mathrm{EDFA}} \approx 15$ stems from the excess noise imparted by the EDFA optical amplifier, the remaining $n_{\mathrm{imp}}^{\mathrm{loss}} \approx 5$ imprecision quanta being due to optical loss of signal inside the cavity (11.7 dB) and in the optical fiber output waveguide (2.2 dB).

5.4.4 Error Analysis

We can calculate the cumulative error for the measured intracavity phonon number using (5.12) and statistics on the set of measurable parameters, giving

$$\frac{\Delta\bar{n}}{\bar{n}} = \left(\frac{\delta\omega_o^2}{\omega_o^2} + \frac{\delta\kappa_e^2}{\kappa_e^2} + \frac{\delta P_{\text{in}}^2}{P_{\text{in}}^2} + \frac{\delta\widetilde{P_{\omega_m}}^2}{\widetilde{P_{\omega_m}}^2} + \frac{\delta\gamma_i^2}{(\gamma-\gamma_i)^2} + \frac{\delta\gamma^2}{(\gamma-\gamma_i)^2} \right.$$
$$+ \left(\frac{\kappa/2}{(\kappa/2)^2+(\Delta-\omega_m)^2} - \frac{1}{\kappa} \right)^2 \delta\kappa^2 + \left(\frac{2(\Delta-\omega_m)}{(\kappa/2)^2+(\Delta-\omega_m)^2} \right)^2 \delta\Delta^2$$
$$\left. + \left(\frac{2(\Delta-\omega_m)}{(\kappa/2)^2+(\Delta-\omega_m)^2} \right)^2 \delta\omega_m^2 \right)^{1/2}. \tag{5.24}$$

Here we neglected the error on G_e and G_{EDFA} which are much smaller than any other error quantity. To determine the variation in κ, κ_e, and ω_0, we measured the DC optical spectrum for every single data point in Figure 5.5 and determined $\delta\kappa$, $\delta\kappa_e$, and $\delta\omega_o$ from the normalized standard deviations of each of the values. The measurement uncertainty of these values is below 0.7%. The uncertainty in the mechanical properties, $\delta\gamma$, $\delta\widetilde{P_{\omega_m}}$, and $\delta\omega_m$, was determined from the deviation on the spectra fits using a 95% confidence interval, which produces percent errors below 0.6%. The pump laser detuning from the cavity is controlled by the EIT reflection spectra. To find the variation of the detuning, $\delta\Delta$, we once again computed the standard deviation of all the measured detunings, which results in a deviation of less than 0.3%.

The two main sources of error in our data are the determination of the intrinsic mechanical quality factor (reflected in γ_i) and the input power, P_{in}. The uncertainty in the mechanical linewidth, $\delta\gamma_i$, is found by repeatedly measuring it at a single power level and computing its standard deviation (found to be ∼1.6%). Using the calibration procedure discussed in Section 5.3.1 for P_{in}, the error lies in the determination of losses L_0 and L_1. In the worst case the calibration would be off by the ratio between the input loss, L_0 in the present experiment, and the square root of total loss $\sqrt{L_0 L_1}$ producing a percentage error of ∼4.0% to the input power.

Taking all of these factors into account, as well as the optical noise discussed in Section 5.6.1, we find an overall uncertainty of ∼9% in the measured absolute phonon number at the maximum cooling point.

5.5 Modifications to Intrinsic Mechanical Damping

5.5.1 Temperature Dependence

Absorption in the dielectric cavity causes the temperature of the cavity to increase locally. This effect is expressed through shifts in the refractive index of the structure, and the thermo-optic coefficient

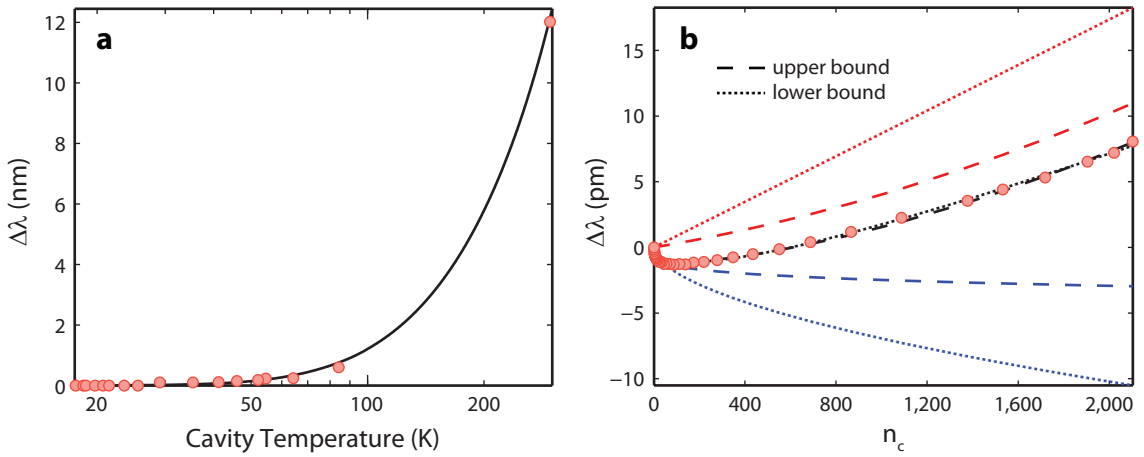

Figure 5.6: **Thermo-optic effects. a**, The measured wavelength shift compared to the theoretical shift predicted by (5.26) for a range of cavity temperatures, using 17.6 K as the reference point. **b**, The measured power-dependent wavelength shift of the cavity with fitted individual contributions due to free carrier dispersion (blue) and refractive index change (red), as well as their sum (black), for the two bounds discussed in the text.

of silicon [119]. As such, we can estimate the temperature of the cavity by looking at the shift in the cavity frequency, starting from a known temperature.

Equation (3.27), the first-order perturbation formula for dielectric cavities, in the slightly recast form,

$$\frac{\Delta\omega_o}{\omega_o} \approx \frac{\Delta\lambda_o}{\lambda_o} \approx -\frac{1}{2}\frac{\int d\boldsymbol{x}\, \delta\varepsilon(\boldsymbol{x})|\boldsymbol{E}(\boldsymbol{x})|^2}{\int d\boldsymbol{x}\, \varepsilon(\boldsymbol{x})|\boldsymbol{E}(\boldsymbol{x})|^2}, \tag{5.25}$$

is starting point of this analysis. For the temperature dependent index of refraction, $n(T)$, we have the relation $\varepsilon/\varepsilon_0 = n^2$, so we find $\delta\varepsilon = 2n\delta n\varepsilon_0$. Defining T_0 as the uniform initial temperature of the cavity and assuming the perturbed cavity temperature, T, is also uniform, (5.25) can be written

$$\frac{\Delta\lambda_o}{\lambda_o} \approx -\frac{\int_{\mathrm{Si}} d\boldsymbol{x}\, |\boldsymbol{E}(\boldsymbol{x})|^2}{\int d\boldsymbol{x}\, n(\boldsymbol{x}, T_0)^2|\boldsymbol{E}(\boldsymbol{x})|^2} n_{\mathrm{Si}}(T_0)\Delta n_{\mathrm{Si}}, \tag{5.26}$$

where the volume integral in the numerator is only over the dielectric and $\Delta n_{\mathrm{Si}} = n_{\mathrm{Si}}(T) - n_{\mathrm{Si}}(T_0) \ll 1$ is the change in the index of refraction of the dielectric between T and T_0. Using the values of $n(T)$ for silicon found in literature [119], and a value of

$$\frac{\int_{\mathrm{Si}} d\boldsymbol{x}\, |\boldsymbol{E}(\boldsymbol{x})|^2}{\int d\boldsymbol{x}\, n(\boldsymbol{x}, T_0)^2|\boldsymbol{E}(\boldsymbol{x})|^2} \approx 7.5066 \times 10^{-2}$$

calculated from the finite element simulations (FEM) of the optical mode profiles for an initial temperature of $T_0 = 300$ K, we plot the wavelength shift from 17.6 K up to 300 K in Figure 5.6a. The total shift of 12.0 nm agrees with the experimentally observed change in resonance wavelength.

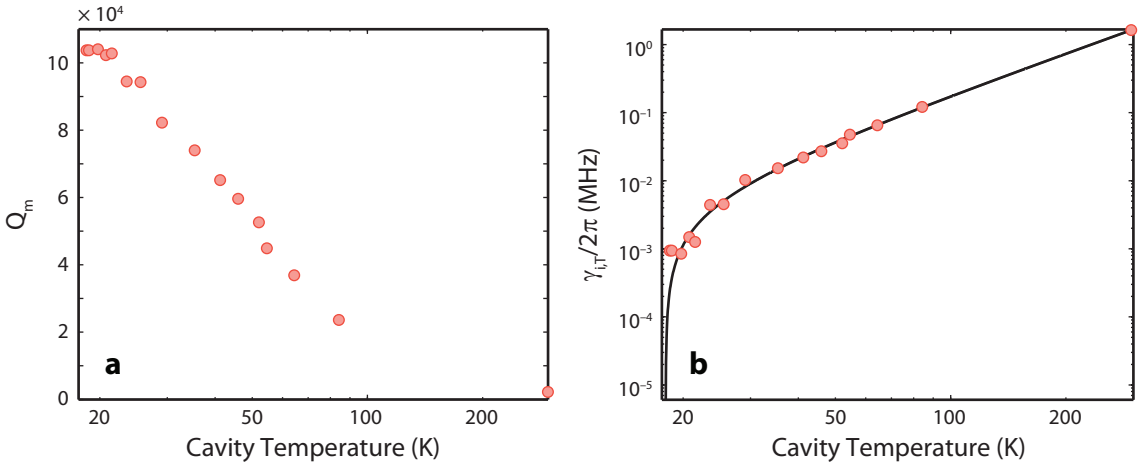

Figure 5.7: **Temperature-dependent loss. a**, The measured intrinsic mechanical quality factor for various cavity temperatures. **b**, The inferred intrinsic mechanical loss rate due to temperature, $\gamma_{i,T}$, modeled by a 4th-order polynomial fit.

This analysis can be applied to the wavelength shift data for various input powers at low temperature (Figure 5.6b, red circles) to determine the heating due to the intracavity photon population. We note an initial blueshift of the cavity, which is attributed to free carrier dispersion effects [68] and can be modeled by a power law dependence on intracavity photon number, $A(n_c)^B$, where A and B are fitting parameters. The temperature-dependent data for the refractive index of silicon in [119] is valid only for $T > 30$ K, so the power-dependent cavity heating for a starting temperature of 17.6 K, for the largest intracavity photon number, can only be bounded. For the upper bound, we assume $dn/dT = 0$ for $T < 30$ K, resulting in a $\Delta T_{\max}$ of 16.8 K. For the lower bound, we assume $dn/dT = dn/dT|_{T=30\text{ K}}$ for $T < 30$ K, resulting in a $\Delta T_{\min}$ of 7.8 K. These bounds and their respective fits are shown in Figure 5.6b.

Independent measurements of the mechanical quality factor, Q_m, at varying bath temperatures indicate that the Q_m changes with temperature (Figure 5.7a). These measurements are taken at low intracavity photon number, rendering free carrier effects negligible (see Section 5.5.2). As such we can model the mechanical loss rate as $\gamma_i(T) = \gamma_{i,T}(T) + \gamma_i^{(0)}$ where $\gamma_i^{(0)}$ is the measured mechanical loss rate at the reference temperature (17.6 K). The extracted form of $\gamma_{i,T}(T)$ is shown in Figure 5.7b. Temperature dependence of mechanical damping sources are further discussion in Section 3.4.3.

5.5.2 Intracavity Photon Number Dependence

The deviation of the expected cooled phonon number from the measured value is a result of two factors: bath heating and an increase in the intrinsic mechanical loss rate (γ_i) due to heating and free carriers. Since the integrated spectral power of the noise PSD near ω_m depends on the *product* $\gamma_i T_b$

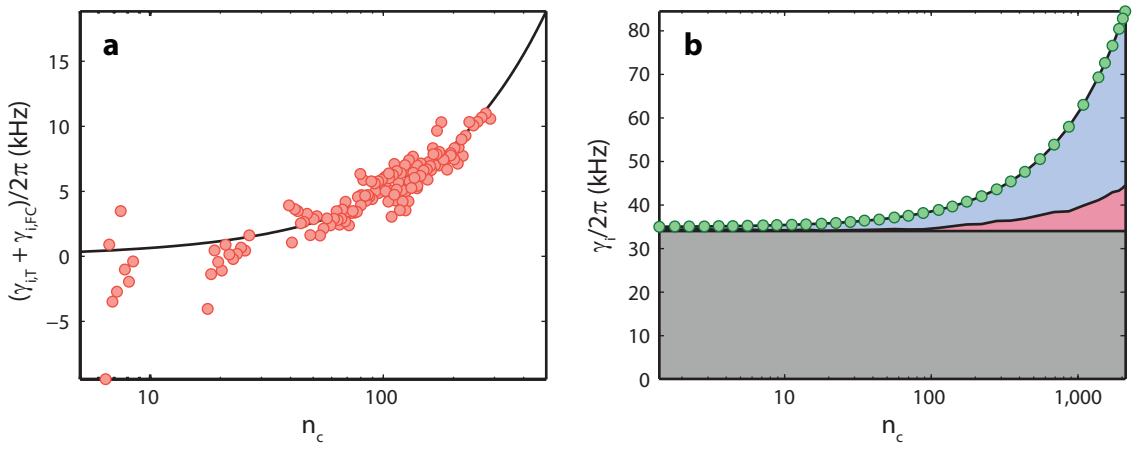

Figure 5.8: **Photon number–dependent loss. a**, Excess loss as a function of n_c, inferred from far-red-detuned ($\Delta > 5.5$ GHz) measurements of $\gamma(n_c) - \gamma^{(0)}(n_c) = \gamma_{i,T}(T(n_c)) + \gamma_{i,\mathrm{FC}}(n_c)$. **b**, Breakdown showing the individual contributions of $\gamma_i^{(0)}$ (gray), $\gamma_{i,T}$ (red), and $\gamma_{i,\mathrm{FC}}$ (blue) to the total γ_i (○).

(for large intracavity photon numbers, n_c), naively ignoring the latter effect results in an estimated change of >50 K in the bath temperature for ∼2,000 intracavity photons. This is unrealistic as (5.26) predicts that such a temperature change would tune the optical mode red by >300 pm, while the actual measured shift is closer to 10−20 pm (from Figure 5.6b). Thus, we attribute part of the deviation in phonon number to a nonlinear process in the cavity involving the generation of free carriers, and introduce an additional loss channel $\gamma_{i,\mathrm{FC}}$ in the intrinsic mechanical loss rate so that we have an intracavity photon number dependent loss rate given by

$$\gamma_i \to \gamma_i(n_c) \equiv \gamma_i^{(0)} + \gamma_{i,T}(T(n_c)) + \gamma_{i,\mathrm{FC}}(n_c). \tag{5.27}$$

From previous derivations, in the absence of heating effects, we would have a damped mechanical linewidth given by $\gamma^{(0)}(n_c) = \gamma_i^{(0)} + \gamma_{\mathrm{OM}}(n_c)$ (which can be computed for any n_c and any Δ from the optical/mechanical characterizations at low intracavity photon numbers). Incorporating (5.27), we have experimentally, $\gamma(n_c) = \gamma_i(n_c) + \gamma_{\mathrm{OM}}(n_c)$, with their difference,

$$\gamma(n_c) - \gamma^{(0)}(n_c) = \gamma_{i,T}(T(n_c)) + \gamma_{i,\mathrm{FC}}(n_c), \tag{5.28}$$

yielding the magnitude of the additional loss rates. However, for $\Delta = \omega_m$ and $n_c > 10$, γ_{OM} tends to be large compared to γ_i, making this subtraction quite error prone. To get accurate data for high intracavity photon numbers we use larger detunings, $\Delta \gg \omega_m$, noting from (2.46) that $\gamma_{\mathrm{OM}} \propto \Delta^{-2}$ for $\Delta \gg \omega_m$ and fixed n_c (approximately). Thus, for the *same* intracavity photon number at a larger detuning, we have a smaller γ_{OM}. The disadvantage of this of course is that we cannot obtain

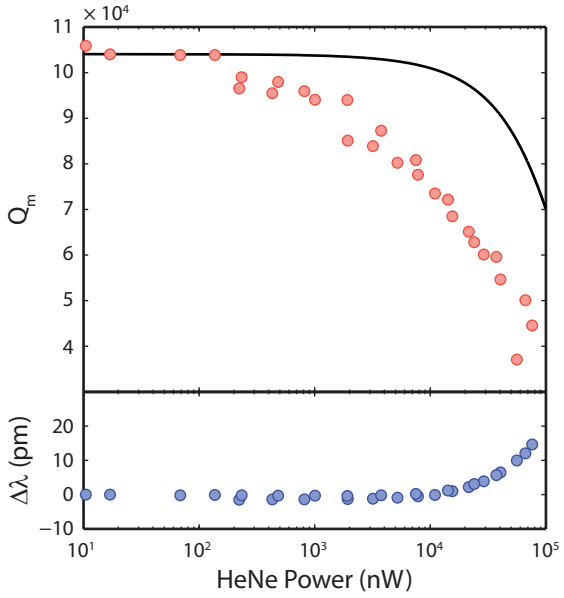

Figure 5.9: **Loss due to free carriers.** The Q_m degradation as a function of 532 nm laser power (red ○). The black line shows the expected Q_m for the bath temperature rise inferred from the wavelength shift data (blue ○). The deviation of the data from this prediction suggests an additional loss channel related to the presence of free carriers.

large intracavity photon numbers due to limits in laser power (the highest we achieve is ∼500). The results of these large detuning measurements are shown in Figure 5.8a, where we have modeled the excess loss using a power law dependence on n_c.

The addition of a free carrier related loss channel is corroborated by pumping the silicon sample above the band gap with a 532 nm solid state green laser, directly stimulating the production of free carriers. The results of this is shown in Figure 5.9. The degradation in Q_m can be only partially explained by heating due to absorption since the maximum 19 K temperature rise estimated from the cavity redshift results in an expected Q_m of approximately 70,000 at the highest power (estimated using Figure 5.7a), whereas a far lower value is measured. The remaining excess loss is attributed to the presence of free carriers.

5.5.3 Combined Loss Model

We use the models of excess mechanical loss from Figure 5.8a and Figure 5.7b in the mechanical mode thermometry procedure outlined in Section 5.3 by replacing the constant γ_i with the intracavity photon number dependent $\gamma_i(n_c)$ from (5.27). In this way, we can more accurately characterize the temperature rise in the cavity, as well as determine the individual contributions of $\gamma_{i,T}$ and $\gamma_{i,\mathrm{FC}}$ as a function of n_c (breakdown shown in Figure 5.8b). The result is an estimated increase of 13.2 K in T_b at the highest input power, well within the temperature bounds derived in Section 5.5.1. We

note that the minimum phonon occupation is unchanged by this analysis since all we are doing is determining relative contributions to the conserved product, $\gamma_i T_b$.

5.6 Noise Considerations

5.6.1 Phase Noise

In the measurements of this work, the same optical laser beam used to cool the mechanical oscillator is also used to detect its mechanical motion. Photodetection of the transmitted cooling beam and the light scattered by the mechanical oscillator produce a heterodyne output signal proportional to the mechanical motion. This also means that fluctuations in the cooling laser beam input that are imprinted into the mechanical system, are also read out by a beam containing the same fluctuations. In addition to potentially raising the phonon number beyond the quantum-backaction limit (in the case of added technical laser noise beyond shot noise), noise on the input cooling beam can also lead to a coherent cancellation effect at the readout called "noise squashing" which may cause the mechanical mode occupation to be inferred incorrectly (note that this effect can also be understood in terms of the recently demonstrated electromagnetically induced transparency (EIT), whereby noise photons are transmitted and/or reflected through a transparency window created by the cooling beam). Noise squashing has been studied in low-frequency mechanical systems, where excess laser phase noise can be an issue, and in recent microwave work where the electromagnetic cavity is populated with residual photons [49].

In this section, we will model the impact of laser phase noise on the previously derived results in Section 2.2. In brief, we show theoretically that the additional cavity noise photons cause an offset in the measured background (broadband) NPSD, which when compared in magnitude to the narrowband Lorentzian signal generated by the mechanical system can be used to assess the impact of the added noise on the inferred phonon population from the measured spectrum. We present the measured offset in the background NPSD versus cooling beam power for the cooling data of Figure 5.5, and compare it with the measured narrowband Lorentzian signal level, indicating that any added noise photons produce at most a 3% uncertainty in the inferred phonon occupancy of the mechanical oscillator. This analysis closely follows the work by Safavi-Naeini et al. [120].

We can model phase noise as a random rotating phase factor on the input field amplitude, given in the frame rotating with ω_ℓ as

$$\alpha_{\rm in} \rightarrow \alpha_{\rm in} e^{i\phi(t)} \approx \alpha_{\rm in}\left(1 + i\phi(t) - \frac{\phi(t)^2}{2} + \mathcal{O}(\phi(t)^3)\right), \tag{5.29}$$

where $\phi(t)$ is a stationary, zero-mean ($\langle\phi(t)\rangle = 0$), random variable presumed to be small ($\phi(t) \ll 1$), and we can assume $\phi(0) = 0$. Random variables are characterized by their correlations, but since

the autocorrelation for a stationary process depends only on the difference in t, we can write without a loss of generality,

$$\langle \alpha_{\rm in}^*(\tau)\alpha_{\rm in}(0)\rangle = |\alpha_{\rm in}|^2\left(1-\frac{1}{2}\langle\phi^2(\tau)\rangle\right). \tag{5.30}$$

We will ultimately treat the random phase factor as an additional perturbative input field, $\hat{a}_{{\rm in},\phi}$, with nonvanishing correlations $\langle \hat{a}^\dagger_{{\rm in},\phi}(\omega)\hat{a}_{{\rm in},\phi}(\omega')\rangle$. In the context of the derivations from Section 2.2, we will map $\hat{a}_{\rm in} \rightarrow \hat{a}_{\rm in} + \hat{a}_{{\rm in},\phi}$ and consider the impact on the steady state mechanical mode occupancy, (2.57), and the normalized spectral density, (2.63). Since the derivations were done by linearizing about a large steady state intracavity population, we recognize the second term in (5.30) as $\langle \hat{a}^\dagger_{{\rm in},\phi}(\tau)\hat{a}_{{\rm in},\phi}(0)\rangle$. Noting that $\phi(\tau) = \int_0^\tau ds\,\dot{\phi}(s)$ and $S_{\dot{\phi}\dot{\phi}}(\omega') = \omega'^2 S_{\phi\phi}(\omega)$ (integration by parts), we have

$$\begin{aligned}
\langle \hat{a}^\dagger_{{\rm in},\phi}(\tau)\hat{a}_{{\rm in},\phi}(0)\rangle &= -\frac{|\alpha_{\rm in}|^2}{2}\int_0^\tau ds\int_0^\tau ds'\,\langle\dot{\phi}(s)\dot{\phi}(s')\rangle \\
&= -\frac{|\alpha_{\rm in}|^2}{2}\int_0^\tau ds\int_0^\tau ds'\int_{-\infty}^{\infty}\frac{d\omega'}{2\pi}\,e^{i\omega'(s-s')}S_{\dot{\phi}\dot{\phi}}(\omega') \\
&= -\frac{|\alpha_{\rm in}|^2}{2}\int_{-\infty}^{\infty}\frac{d\omega'}{2\pi}\left(\frac{e^{i\omega'\tau}-1}{i\omega'}\right)\left(\frac{e^{-i\omega'\tau}-1}{-i\omega'}\right)S_{\dot{\phi}\dot{\phi}}(\omega') \\
&= -|\alpha_{\rm in}|^2\int_{-\infty}^{\infty}\frac{d\omega'}{2\pi}\left(\frac{1-\cos(\omega'\tau)}{\omega'^2}\right)S_{\dot{\phi}\dot{\phi}}(\omega') \\
&= -|\alpha_{\rm in}|^2\int_{-\infty}^{\infty}\frac{d\omega'}{2\pi}\,(1-\cos(\omega'\tau))\,S_{\phi\phi}(\omega').
\end{aligned} \tag{5.31}$$

The spectral density is given by

$$\begin{aligned}
S_{a_{{\rm in},\phi}a_{{\rm in},\phi}}(\omega) &= -|\alpha_{\rm in}|^2\int_{-\infty}^{\infty}d\tau\,e^{i\omega\tau}\int_{-\infty}^{\infty}\frac{d\omega'}{2\pi}\,(1-\cos(\omega'\tau))\,S_{\phi\phi}(\omega') \\
&= -|\alpha_{\rm in}|^2\delta(\omega)\int_{-\infty}^{\infty}d\omega'\,S_{\phi\phi}(\omega') + \frac{|\alpha_{\rm in}|^2}{2}\left(S_{\phi\phi}(\omega)+S_{\phi\phi}(-\omega)\right).
\end{aligned} \tag{5.32}$$

We can then compute the correlations in the frequency domain,

$$\langle \hat{a}^\dagger_{{\rm in},\phi}(\omega)\hat{a}_{{\rm in},\phi}(\omega')\rangle = \frac{1}{2\pi}\int_{-\infty}^{\infty}dt\int_{-\infty}^{\infty}dt'\,e^{-i\omega t}e^{-i\omega' t'}\,\langle \hat{a}^\dagger_{{\rm in},\phi}(t)\hat{a}_{{\rm in},\phi}(t')\rangle,$$

which we can simplify by applying the coordinate transformation $u = t + t'$ and $v = t - t'$, yielding

$$\begin{aligned}
\langle \hat{a}^\dagger_{{\rm in},\phi}(\omega)\hat{a}_{{\rm in},\phi}(\omega')\rangle &= -\frac{1}{4\pi}\int_{-\infty}^{\infty}du\int_{-\infty}^{\infty}dv\,e^{-i\omega\left(\frac{u+v}{2}\right)}e^{-i\omega'\left(\frac{u-v}{2}\right)}\langle \hat{a}^\dagger_{{\rm in},\phi}(v)\hat{a}_{{\rm in},\phi}(0)\rangle \\
&= \delta(\omega+\omega')\int_{-\infty}^{\infty}dv\,e^{-i\omega v}\langle \hat{a}^\dagger_{{\rm in},\phi}(v)\hat{a}_{{\rm in},\phi}(0)\rangle \\
&= \delta(\omega+\omega')S_{a_{{\rm in},\phi}a_{{\rm in},\phi}}(\omega),
\end{aligned} \tag{5.33}$$

where we see that the phase noise perturbation can be thought of as a thermal force on the mechanics, resulting in heating.

Making the replacement $\hat{a}_{\rm in} \to \hat{a}_{\rm in} + \hat{a}_{{\rm in},\phi}$ and recomputing (2.56) with the addition of phase noise, we have instead

$$\begin{aligned} S_{bb}(\omega) &= \int_{-\infty}^{\infty} d\omega' \, \langle \hat{b}^\dagger(\omega)\hat{b}(\omega')\rangle \\ &= \frac{\gamma}{(\omega_m+\omega)^2+(\gamma/2)^2} \\ &\quad \times \left(\frac{\gamma_i n_b}{\gamma} + \frac{|G|^2\kappa}{\gamma} \frac{1+(\kappa_e/2\kappa)S_{a_{{\rm in},\phi}a_{{\rm in},\phi}}(\omega)}{(\Delta-\omega)^2+(\kappa/2)^2} + \frac{|G|^2\kappa}{\gamma} \frac{(\kappa_e/2\kappa)S_{a_{{\rm in},\phi}a_{{\rm in},\phi}}(\omega)}{(\Delta+\omega)^2+(\kappa/2)^2} \right), \end{aligned} \tag{5.34}$$

and the phase noise modified damped cavity phonon population,

$$\bar{n}(\Delta) = \frac{\gamma_i n_b}{\gamma} + \frac{|G|^2\kappa}{\gamma} \frac{1+(\kappa_e/2\kappa)n_\phi}{(\Delta+\omega_m)^2+(\kappa/2)^2} + \frac{|G|^2\kappa}{\gamma} \frac{(\kappa_e/2\kappa)n_\phi}{(\Delta-\omega_m)^2+(\kappa/2)^2}, \tag{5.35}$$

where we have defined $n_\phi \equiv S_{a_{{\rm in},\phi}a_{{\rm in},\phi}}(\omega_m)$, the number of phase noise quanta at the mechanical frequency. For $\Delta = \omega_m$, we have

$$\begin{aligned} \bar{n}(\omega_m) &\approx \frac{\gamma_i n_b}{\gamma} + \frac{|G|^2\kappa}{4\gamma\omega_m^2}\left(1+\frac{\kappa_e}{2\kappa}n_\phi\right) + \frac{4|G|^2}{\gamma\kappa}\frac{\kappa_e}{2\kappa}n_\phi \\ &\approx \frac{\gamma_i n_b}{\gamma} + \frac{\gamma_{\rm OM}}{\gamma}\left(\left(\frac{\kappa}{4\omega_m}\right)^2 + \frac{\kappa_e}{2\kappa}n_\phi\right). \end{aligned} \tag{5.36}$$

Thus, we can see that phase noise heating manifests as the number of phase quanta at ω_m (n_ϕ), modified by both the cavity coupling efficiency ($\kappa_e/2\kappa$) and the optics–mechanics coupling efficiency ($\gamma_{\rm OM}/\gamma$).

We can now determine the modified induced photocurrent by treating the phase noise as a detuned drive and utilizing the frequency response of the cavity on transmission, $t_+(\omega)$ (assuming $\Delta = \omega_m$), given by (2.39). Considering just the contribution from the phase noise, the fluctuating optical power near ω_m will be proportional to $\hat{N}_\phi = t_+(\omega)a_{{\rm in},\phi}(\omega) + t_+^*(-\omega)a_{{\rm in},\phi}^\dagger(\omega)$. The model of phase noise we have chosen imposes a relationship between the positive and negative frequency components of $\hat{a}_{{\rm in},\phi}(\omega)$. We can see this by imposing a small, strictly sinusoidal phase modulation in place of $\phi(t)$, yielding

$$\alpha_{\rm in} \to \alpha_{\rm in} e^{i\beta_c\cos\omega t + i\beta_s \sin\omega t} \approx \alpha_{\rm in}\left(1 + \frac{\beta_s+i\beta_c}{2}e^{i\omega t} - \frac{\beta_s - i\beta_c}{2}e^{-i\omega t}\right), \tag{5.37}$$

from which we can deduce that $\hat{a}^{(+)}_{\text{in},\phi}(\omega) = -\left(\hat{a}^{(-)}_{\text{in},\phi}(-\omega)\right)^\dagger$, having defined

$$\hat{a}^{(+)}_{\text{in},\phi}(\omega) = \Theta(\omega)\hat{a}_{\text{in},\phi}(\omega), \tag{5.38}$$

$$\hat{a}^{(-)}_{\text{in},\phi}(\omega) = \Theta(-\omega)\hat{a}_{\text{in},\phi}(\omega), \tag{5.39}$$

as the positive and negative frequency components respectively (where $\Theta(\omega)$ is the Heaviside function), satisfying $\hat{a}_{\text{in},\phi}(\omega) = \hat{a}^{(+)}_{\text{in},\phi}(\omega) + \hat{a}^{(-)}_{\text{in},\phi}(\omega) = \hat{a}^{(+)}_{\text{in},\phi}(\omega) - \hat{a}^{(+)\dagger}_{\text{in},\phi}(\omega)$. With this symmetry, the correlation given by (5.33) can be written

$$\begin{aligned}\langle \hat{a}^\dagger_{\text{in},\phi}(\omega)\hat{a}_{\text{in},\phi}(\omega')\rangle &= \delta(\omega+\omega')S_{a_{\text{in},\phi}a_{\text{in},\phi}}(\omega) \\ &\quad\times\Big(\Theta(\omega)\Theta(\omega') + \Theta(\omega)\Theta(-\omega') + \Theta(-\omega)\Theta(\omega') + \Theta(-\omega)\Theta(-\omega')\Big).\end{aligned} \tag{5.40}$$

The symmetry also results in additional cancellations in $\hat{N}_\phi$, yielding the simplified form,

$$\hat{N}_\phi = r_+(\omega)a_{\text{in},\phi}(\omega) + r^*_+(-\omega)a^\dagger_{\text{in},\phi}(\omega), \tag{5.41}$$

the spectral density of which is

$$S_{N_\phi N_\phi}(\omega) = \Big(|r_+(\omega)|^2\Theta(\omega) + |r_+(-\omega)|^2\Theta(-\omega)\Big)S_{a_{\text{in},\phi}a_{\text{in},\phi}}(\omega), \tag{5.42}$$

having used the expanded form of $\langle \hat{a}^\dagger_{\text{in},\phi}(\omega)\hat{a}_{\text{in},\phi}(\omega')\rangle$ from above, and noting that $\Theta(\omega)\Theta(-\omega)$ vanishes and $\Theta(\omega)\Theta(\omega) = \Theta(\omega)$. Using the previously derived expression for $|r_+(\omega)|^2$ (5.8) and concerning ourselves only with $\Delta = \omega_m$, ω close to ω_m, and the large cooperativity limit ($\gamma_{\text{OM}} \gg \gamma_i$),

$$\begin{aligned}S_{N_\phi N_\phi}(\omega) &\approx n_\phi\left(\frac{\kappa_e}{\kappa}\right)^2\left(1 - \frac{\gamma^2_{\text{OM}}}{4}\frac{1}{(\omega_m-\omega)^2+(\gamma/2)^2} - \frac{\gamma^2_{\text{OM}}}{4}\frac{1}{(\omega_m+\omega)^2+(\gamma/2)^2}\right) \\ &= n_\phi\left(\frac{\kappa_e}{\kappa}\right)^2 - \frac{4\kappa_e|G|^2}{\kappa^2}\frac{4|G|^2}{\kappa}\frac{(\kappa_e/2\kappa)n_\phi}{2}\left(\frac{1}{(\omega_m-\omega)^2+(\gamma/2)^2} + \frac{1}{(\omega_m+\omega)^2+(\gamma/2)^2}\right).\end{aligned} \tag{5.43}$$

The crucial point to note is that the second term is effectively an inverted Lorentzian that reduces the overall amplitude of the measured power spectral density, resulting in an inferred phonon number, $\bar{n}_{\text{inf}}$, smaller than the true phonon number. The complete phase noise modified spectrum can be obtained by adding this to (2.63), giving

$$S_{NN}(\omega) = 1 + n_\phi\left(\frac{\kappa_e}{\kappa}\right)^2 + \frac{4\kappa_e|G|^2}{\kappa^2}\bar{S}_{bb}(\omega;\bar{n}_{\text{inf}}), \tag{5.44}$$

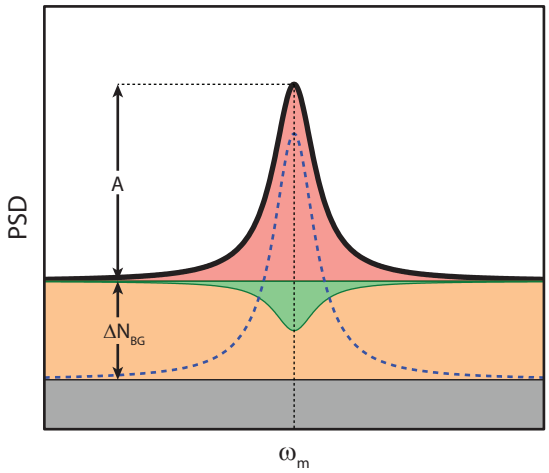

Figure 5.10: **Phase noise–modified output spectra.** An exaggerated plot of the impact of phase noise on the measured power spectral density. The thick black line with red fill is the actual measured signal, given in its normalized form by S_{NN} (5.44), with a normalized amplitude $A = 2\kappa_e \bar{n}_{\rm inf}/\kappa$ in the large cooperativity limit. The green curve showing the magnitude of the "squashing" effect (corresponding to the inverted Lorentzian term in (5.43)). The dashed blue curve indicates the theoretical signal in the absence of phase noise. The orange is the flat excess background signal due to phase noise and the gray is the shot-noise level. The difference in backgrounds for a far detuned signal, $\Delta \gg \omega_m$, and a spectrum measured at $\Delta = \omega_m$ is given by $\Delta N_{\rm BG} = n_\phi(\kappa_e/\kappa)^2$ (again, for a normalized spectra).

where integrating $\bar{S}_{bb}(\omega; \bar{n}_{\rm inf})$ near $\omega = \omega_m$ yields

$$\bar{n}_{\rm inf} = \frac{\gamma_i n_b}{\gamma} - \frac{\kappa_e n_\phi}{2\kappa}. \tag{5.45}$$

Thus, we will underestimate the true phonon occupation by $\bar{n} - \bar{n}_{\rm inf} = \kappa_e n_\phi/\kappa$. The individual contributions to the phase noise modified normalized spectral density are shown in Figure 5.10.

In the context of the cooling experiment, we can estimate the heating caused by excess phase noise by making a second measurement of the optical transmission NPSD with the cooling beam far-detuned from the cavity (several mechanical frequencies in practice), while keeping all other experimental parameters constant. The difference around the mechanical frequency in the background of the NPSD taken far-detuned, $N_{\rm BG,detuned}$, and the background of the spectrum taken during a cooling run, $N_{\rm BG}$, may be used to place bounds on the difference between $\bar{n}$ and the measured $\bar{n}_{\rm inf}$. By doing a background subtraction of the far-detuned measured RF spectra from the cooling spectra, we can fit A and $\Delta N_{\rm BG} \equiv N_{\rm BG} - N_{\rm BG,detuned}$ for each cooling beam power. We have then

$$\frac{\Delta N_{\rm BG}}{A} = \frac{n_\phi(\kappa_e/\kappa)^2}{2\kappa_e \bar{n}_{\rm inf}/\kappa} = \frac{\kappa_e}{2\kappa}\frac{n_\phi}{\bar{n}_{\rm inf}}, \tag{5.46}$$

where we compare the measured ratio to the expected ratio calculated from (5.44) in the large

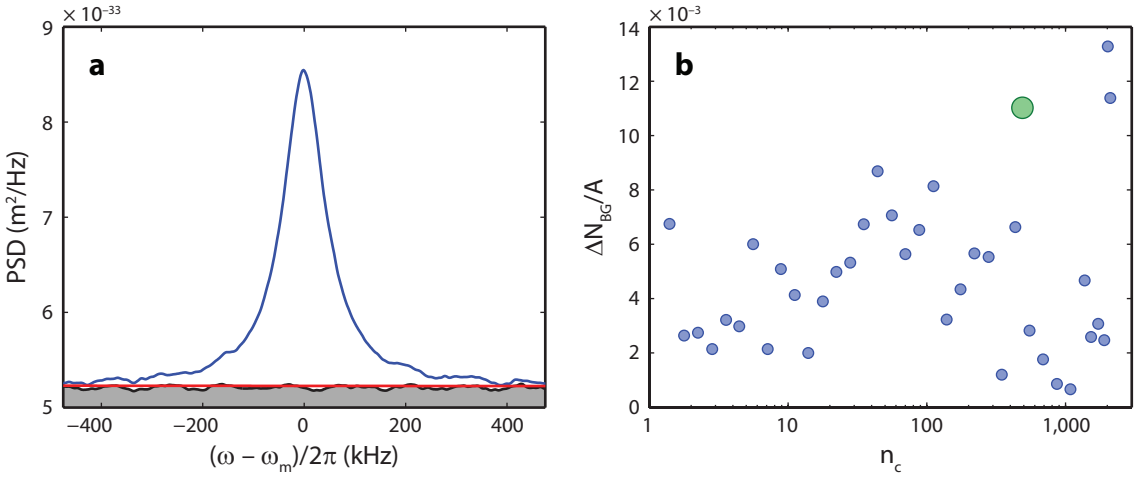

Figure 5.11: **Experiment phase noise analysis. a**, Typical recorded cooling spectrum showing that the background of the measured Lorentzian (red line) is nearly indistinguishable from the far-detuned background spectrum (black line). **b**, Plot versus cooling beam power of the ratio between the background difference ΔN_{BG} and the peak of the mechanical mode signal A as defined in the text. The green data point is a filtered laser measurement, exhibiting no significant difference from the unfiltered measurements.

cooperativity limit. Thus, in the same large cooperativity limit, the underestimation factor is given by $(\bar{n} - \bar{n}_{\mathrm{inf}})/\bar{n}_{\mathrm{inf}} \approx 2\Delta N_{\mathrm{BG}}/A$.

In Figure 5.11 we show a plot of a typical measured cooling and far-detuned noise spectrum pair for a single cooling beam power along with the deduced ratio $\Delta N_{\mathrm{BG}}/A$ for each cooling beam power. Crucially, the ratio $\Delta N_{\mathrm{BG}}/A$ is seen to be roughly cooling beam power independent and at a level of less than 1.5%, corresponding to an underestimation of the true phonon number, $\bar{n}$, at most by about 3%, well within the established experimental error.

In addition to these background subtraction measurements, a scanning Fabry-Perot filter with a free spectral range of 5.5 GHz and a bandwidth of 50 MHz was peak-locked to the output of the laser, providing a noise suppression of >30 dB at ω_m. No significant change in the background (plotted as a single point in Figure 5.11b) or $\bar{n}_{\mathrm{inf}}$ was measured, further indicating that laser phase noise is not a factor in this experiment.

Direct phase noise measurements for the laser used in this experiment (and other lasers in the lab) can be found in [120], and corroborates the analysis presented here. With these laser characterizations, we can illustrate the impact of phase noise on the measured signal by purposefully making a measurement in a noisy region of the laser. One of our lasers (New Focus, model TLB-6728) has a phase noise peak around 5.1 GHz, while another laser (New Focus, model TLB-6328) is shot-noise limited in that region. Using a device with a mechanical breathing mode at 5.1 GHz (the 5GHF design, discussed in Section 6.1), we can compare the spectra taken at large cooperativities a mechanical frequency red-detuned. This is shown in Figure 5.12, where the large amount of phase

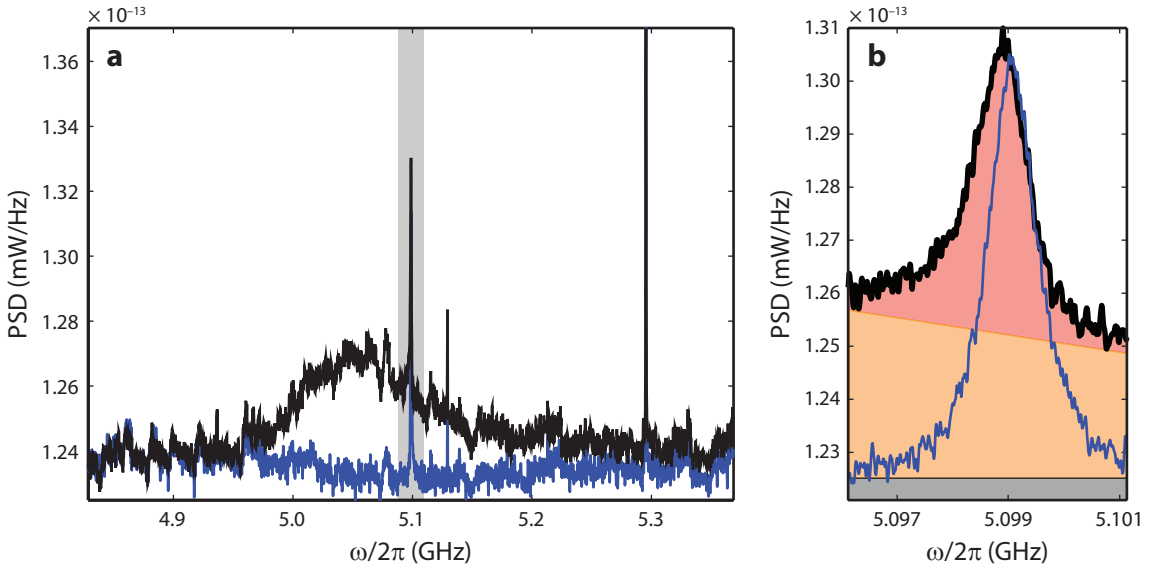

Figure 5.12: **Comparison of cooling spectra with and without phase noise.** Cooling spectra for $\Delta/2\pi = \omega_m/2\pi = 5.1$ GHz (in a 5GHF device) and $C \gg 1$, comparing the TLB-6728 laser (black curves, with a phase noise peak just below 5.1 GHz), against the TLB-6328 laser (blue curves, shot-noise limited near 5.1 GHz), with P_{in} and all other experimental parameters constant. **a**, Broad power spectrum of the measured signals. For the TLB-6728 laser, we see accordingly a significant noise peak at slightly less than 5.1 GHz on which the mechanical mode at 5.1 GHz sits. The shot-noise-limited laser exhibits no such peak and the mechanical mode sits on a flat background. **b**, Spectral density of the detected signal near ω_m for the two lasers. The spectra are colored in analogy to Figure 5.10 and we see a significant offset in the black curve due to laser phase noise. We further note a reduced Lorentzian area in the PSD of the noisy laser signal, leading to an underestimation of the phonon occupation ($\bar{n}_{\text{inf}} = 0.8$ from the black curve compared $\bar{n} = 1.2$ from the blue curve). Credit for this data goes to Amir Safavi-Naeini and Jeff Hill.

noise results in a significantly different spectral density near ω_m. In addition to a large phase noise offset in the Lorentzian signal, the inferred phonon occupation from naively integrating the area under the peak is smaller than the true phonon occupation due to the noise squashing effect.

5.6.2 Amplifier Noise

We consider here the impact of using a nonideal amplifier (EDFA) on the measured signal, and the deviation from quantum limits of motion transduction. For a coherent optical beam with frequency ω_ℓ and power P incident on a photodetector, the single-sided power spectral density of the optical shot noise is simply

$$S_{\text{shot}}(\omega) = \sqrt{2\hbar\omega_\ell P}, \tag{5.47}$$

independent of frequency. If we consider the EDFA gain, G_{EDFA}, and the optical insertion loss between the output of the cavity and the input of the EDFA, η_d (measured to be 2.2 dB), the

corresponding noise at the output of the amplifier assuming noise-free amplification is given by

$$S_{\text{shot,amplified}} = G_{\text{EDFA}}\sqrt{2\hbar\omega_\ell \eta_d P_{\text{in}}}, \tag{5.48}$$

where P_{in} is the optical power at the input of the cavity and $\eta_d P_{\text{in}}$ is the optical power reaching the input to the EDFA. We use the term "noise-free amplification" here to indicate an amplifier process in which the signal-to-noise ratio (SNR) at the output is equal to that at the input (i.e., an amplifier noise figure of 0 dB). Using the electronic gain, G_e, obtained from calibrations, the theoretical background noise power spectral density (NPSD) measured by the RSA, corresponding to noise-free amplification of shot noise on the optical cooling beam can be found. To wit,

$$\widetilde{S}_{\text{shot,amplified,RSA}} = (S_{\text{shot,amplified}})^2 \left(\frac{G_e}{\eta_d}\right)^2 \frac{1}{R_L}, \tag{5.49}$$

where R_L is the input impedance to the RSA and the ratio G_e/η_d is the electrical conversion factor for optical power at the output of the EDFA (η_d accounts for the loss between the cavity and the EDFA, while G_e accounts for the *total* insertion loss between the cavity and the detector). This is plotted against the measured background NPSD in Figure 5.13a. The trend seen in Figure 5.13a versus cooling beam power (plotted in units of intracavity photon number, n_c) is a result of the varying EDFA drive current versus n_c used in our experiment. Specifically, for intracavity photon populations of <10, we are limited by the highest gain setting of the EDFA. In this regime, the EDFA drive current (and thus gain) remains constant, resulting in the increasing background NPSD with cooling beam optical power. For larger intracavity photon numbers, we are limited by the saturation power of the detector D2. In this regime, the EDFA drive current (gain) is reduced to avoid detector saturation, resulting in the decreasing background NPSD with optical cooling beam power. The difference between the noise-free gain background level modeled by (5.49) and the measured background level, reflects the added noise due to the EDFA (its noise figure). An ideal EDFA amplifier adds 3 dB of noise above the shot-noise level [121]. In a real EDFA device, however, the noise figure of the amplifier depends on both the input power and EDFA drive current (amplifier inversion level). We define the added EDFA optical noise as the noise above that for a noise-free amplification process,

$$\widetilde{S}_{\text{excess}} \equiv \frac{\widetilde{S}_{\text{background}} - \widetilde{S}_{\text{shot,amplified,RSA}}}{(G_e/\eta_d)^2\,(1/R_L)}, \tag{5.50}$$

where $\widetilde{S}_{\text{background}}$ is the actual noise floor of the NPSD at the output of the EDFA. Although the EDFA adds excess noise, its utility stems from the fact that the gain provided by the EDFA overcomes the electronic noise in the photodetectors and RSA, nonunity quantum efficiency in the photodetectors, and optical insertion loss between the EDFA and detector D2, with a resulting

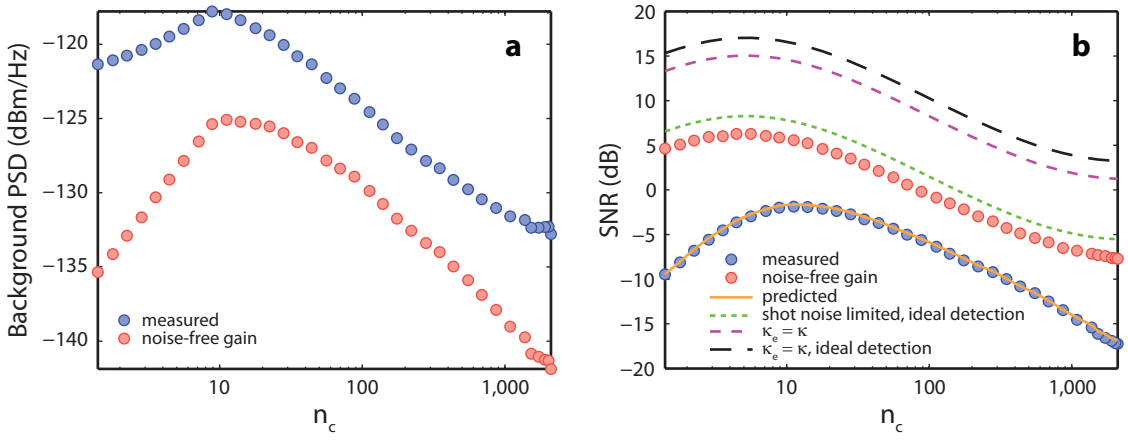

Figure 5.13: **Effect of amplifier noise and optical losses on the measured signal. a**, Comparison of the measured background NPSD to the shot-noise level of the cooling laser beam amplified by an ideal, noise-free amplifier. **b**, Comparison of the SNR for several different cases. (i) Experimental device and measurement conditions of this work. Measured (blue ○) and predicted SNR (orange curve) are both shown. (ii) Shot-noise-limited SNR with noise-free amplification and unit-quantum-efficiency photodetection, all other device parameters as in the experiment. SNR shown with (red ○) and without (dashed green curve) optical loss between the output of the cavity and the input to the optical amplifier. (iii) Noise-free amplification and unit-quantum-efficiency photodetection along with ideal coupling to the cavity system (i.e., single-sided coupling with no other optical loss channels; equivalent to setting $\kappa = \kappa_e/2$). This is plotted with (purple dashed curve) and without (black dashed curve) the optical insertion loss between the output of the cavity and photodetection. The dashed black curve thus represents an ideal quantum-limited transducer of mechanical motion.

overall SNR penalty of only $\widetilde{S}_{\text{excess}}/\eta_d$ (derived below).

In addition to broadband noise, the optical cooling beam signal at the output of the cavity also contains information about the mechanical motion of the localized acoustic mode in the nanobeam cavity. As shown in (2.64), the transduced mechanical motion results in a narrow Lorentzian signal centered at the mechanical frequency that sits on top of the noise floor in the NPSD of the transmitted optical beam. Defining the SNR for this measurement as the ratio between the peak of the Lorentzian component to that of the background in the measured NPSD, we can determine how the different nonidealities of the measurement process (such as cavity coupling, optical loss, and amplifier excess noise) impact the sensitivity of our measurement of mechanical motion. For example, the theoretical shot-noise-limited SNR, corresponding to noise-free amplification, ideal photodetection, and no optical insertion loss after the cavity is given by

$$\text{SNR}_{\text{shot}} = \frac{4P_{\omega_m}/(\gamma_i(n_c) + \gamma_{\text{OM}})}{2\hbar\omega_o P_{\text{in}}}, \tag{5.51}$$

where the numerator is the theoretical cooled peak signal amplitude due to the mechanical motion, with the average oscillating power given by (5.10) for a particular n_c (note that we include in this signal amplitude the effects of the power dependent bath temperature shift and modifications to the

intrinsic mechanical damping rate $\gamma_i(n_c)$, as discussed above). In Figure 5.13b we consider several cases for comparison:

i. **Measurement and cavity parameters as used in this work.** This includes all nonidealities. The actually measured SNR along with a predicted SNR based upon independent measurement and calibration of the device and experimental setup are shown. For the predicted SNR we have,

$$\begin{aligned}\mathrm{SNR}_{\mathrm{predicted}} &= \frac{4G_{\mathrm{EDFA}}^2 G_e^2 P_{\omega_m}/R_L(\gamma_i(n_c)+\gamma_{\mathrm{OM}})}{\widetilde{S}_{\mathrm{background}}} \\ &= \frac{4G_{\mathrm{EDFA}}^2 P_{\omega_m}/(\gamma_i(n_c)+\gamma_{\mathrm{OM}})}{2\hbar\omega_o G_{\mathrm{EDFA}}^2 P_{\mathrm{in}} + \widetilde{S}_{\mathrm{excess}}/\eta_d}\eta_d, \end{aligned} \tag{5.52}$$

which closely corresponds to the actual measured SNR values, as seen in Figure 5.13b. The deviation of the curve shape of the measured SNR from the other cases is attributed primarily to the variance in the excess noise added by the EDFA amplification.

ii. **Shot-noise-limited detection.** We consider both with and without loss in the optical path after the cavity (all other cavity parameters and nonidealities as per the measured device). In the case with optical loss in the optical path we have instead of (5.51),

$$\mathrm{SNR}_{\mathrm{shot,lossy}} = \frac{4P_{\omega_m}/(\gamma_i(n_c)+\gamma_{\mathrm{OM}})}{2\hbar\omega_o P_{\mathrm{in}}}\eta_d, \tag{5.53}$$

where $1-\eta_d$ is the insertion loss discussed above.

iii. **An ideally coupled cavity system with shot-noise-limited detection.** In this case we consider a perfect single-sided cavity system (equivalent to setting $\kappa = \kappa_e/2$) with all other device parameters constant and nonidealities present (excluding added amplifier noise). We repeat the same analysis for the insertion-loss-free case, representing an optimal (quantum-limited) transduction of motion. Considering all the above cases one can infer that a significant fraction of the degradation in our measured SNR from that of an ideal quantum-limited transducer stems from the nonideality of our cavity loading (photons carrying information regarding the mechanical motion are lost into nondetected channels). The remaining inefficiencies in our detection process are a result of the added noise due to the nonideality of the EDFA amplification and the small amount (2.2 dB) of optical loss in the optical path between the cavity output and the EDFA.

5.7 Measurement Imprecision

In considering the limits of a continuous position measurement of the mechanical motion of an object one typically defines a measurement imprecision level related to the power spectrum noise floor on top of which the position signal sits [122]. Conventionally, the imprecision level corresponding to the background NPSD in the power spectrum of the measured signal is expressed in terms of a mechanical displacement sensitivity with units of m^2/Hz. From the quantum mechanical derivation in Section 2.2 and (2.64), the PSD of the measured output signal in our case (transmission of the optical cooling beam) is proportional to

$$S_{NN}(\omega) = B + \frac{4\kappa_e |G|^2}{\kappa^2} \bar{S}_{bb}(\omega). \tag{5.54}$$

The background NPSD is set by the constant B, which for unit quantum efficiency and shot-noise-limited photodetection (as derived), is unity (though for the current measurement, $B > 1$ due to added EDFA amplifier noise and optical loss). Since $\bar{S}_{bb}(\omega)$ is proportional to $\bar{n}$ by (2.56), it is natural to consider the imprecision level of our measurements (due to the background noise level) in units of phonon quanta. The background NPSD in units of "quanta" is simply

$$\widetilde{S}^{(\mathrm{quanta})}_{\mathrm{background}} = \bar{n} \left(\frac{B}{\frac{4\kappa_e |G|^2}{\kappa^2} \bar{S}_{bb}(\omega)\big|_{\omega=\omega_m}} \right). \tag{5.55}$$

A background NPSD, or imprecision level, of $n_{\mathrm{imp}} = 1$ then, corresponds to the equivalent level of NPSD in the output signal that would be produced at the peak of the Lorentzian signal by a single quanta in the mechanical oscillator. For the case of noise-free optical amplification, unit-quantum-efficiency photodetection, and ideal coupling ($\kappa = \kappa_e/2$), the value of the constant B is unity and the background NPSD approaches 1/4 quanta in the large cooperativity limit.

One can convert between an imprecision level in units of quanta and the more conventional m^2/Hz through the relation

$$\widetilde{S}^{(\mathrm{m}^2/\mathrm{Hz})}_{\mathrm{background}} = \left(\frac{4}{\gamma} \right) \left(2x^2_{\mathrm{zpf}} \right) \widetilde{S}^{(\mathrm{quanta})}_{\mathrm{background}}, \tag{5.56}$$

where one phonon quanta has $2x^2_{\mathrm{zpf}}$ worth of displacement noise power which is dispersed over a bandwidth γ (the peak NPSD is $4/\gamma$ times the total noise power). The standard quantum limit (SQL) of displacement sensitivity corresponding to an on-resonance (single-sided) NPSD is equal to $\mathrm{SQL}_x(\omega)|_{\omega=\omega_m} = \left(x^2_{\mathrm{zpf}}/2 \right) (4/\gamma)$, or one-quarter quanta's worth of displacement noise power. Therefore, in terms of this SQL displacement sensitivity, the imprecision levels are related as $\widetilde{S}^{(\mathrm{m}^2/\mathrm{Hz})}_{\mathrm{background}} = (4\mathrm{SQL}_x)\, \widetilde{S}^{(\mathrm{quanta})}_{\mathrm{background}}$. Note that the spectra of the measured NPSD in Figure 5.5b–c of Section 5.4 are given in units of m^2/Hz. In order to determine x_{zpf} for these plots, we numerically

compute the effective motional mass, $m_{\rm eff}$, following Section 3.3. FEM simulations of the mechanical breathing mode of the nanobeam cavity yields a motional mass of $m_{\rm eff} = 311$ fg and a corresponding zero-point fluctuation amplitude of $x_{\rm zpf} = 2.7$ fm.

5.8 Future Directions

Looking forward, the optical backaction cooling and thermometry, as performed in this work, represents only a first step toward optical measurement and control of the quantum state of a nanomechanical object. The mechanical system, although cooled to a mode occupancy below one, is still prepared in a classical thermal state, with its quantum zero-point fluctuations hidden in our measurement scheme. Future experiments, however, to prepare and measure nonclassical quantum states of the mechanical system, are now within reach. A basic requirement for optomechanical experiments in the quantum regime is the ability to exchange photons with the mechanical resonator on a timescale shorter than that for a single thermal phonon entering the mechanical system from the environment. The latter, called the thermal decoherence time, is given by $\tau_T \equiv \hbar Q_m/k_B T_b$, while the timescale at which the mechanical resonator exchanges photons with an optical input is $\tau_{\rm OM} \equiv 1/\gamma_{\rm OM}$. This requirement, $\tau_{\rm OM} < \tau_T$, is equivalent to the requirement for optical backaction cooling of the mechanical oscillator to $\bar{n} < 1$, and is thus realized for the optomechanical crystal devices of this work. This allows for optomechanical entanglement between light and mechanics [123] or quantum state transfer between single optical photons and mechanical phonons [73, 124], enabling mechanical systems to function as both quantum transducers [125] and quantum memory elements [126]. In addition, the chip-scale nature of the optomechanical crystal architecture naturally lends itself to the creation of coupled photon and phonon circuits, facilitating not only the coupling of multiple mechanical and optical objects together, but also allowing for the integration of optomechanics with other quantum system such as superconducting quantum circuits [73]. Finally, if a regime of strong coupling at the single quanta level ($g/\kappa > 1$) [127] could be reached, myriad new opportunities would be available, not the least of which is nonlinear phononics at the single phonon level and the generation of highly nonclassical quantum states in the mechanical or optical field.

Chapter 6

Other Experiments

6.1 Further Device Improvements (5GHF Design)

As alluded to at the end of Section 3.5, we can additionally factor g_{pe} into the fitness function in the device optimization procedure. After running the minimization algorithm for several weeks, the result is the 5GHF design. The new device parameters are listed in Table 3.2 and the FEM simulations are summarized in Figure 6.1. Device fabrication is done in the same way as outlined in Section 4.1.

6.1.1 Device Characterization

Under stabilized vacuum ($<3 \times 10^{-7}$ mbar) and cryogenic ($T_b \sim 10$ K) conditions, we follow Section 5.3.4 and 5.3.5 to measure the mechanical and optical properties of the 5GHF devices. The best optical resonance was found to have $Q_o = 9.1 \times 10^5$, $\omega_o/2\pi = 194$ THz ($\lambda_o = 1{,}545$ nm), and resonant transmission contrast of 38% (intrinsic $Q_{o,i} = 1.2 \times 10^6$). This corresponds to $\kappa/2\pi = 217$ MHz and $\kappa_e/2\pi = 55$ MHz. The best mechanical mode was found to have $Q_m = 6.8 \times 10^5$ and $\omega_m/2\pi = 5.1$ GHz. This corresponds to $\gamma_i/2\pi = 7.5$ kHz and an $f_m \cdot Q_m$ product of 3.5×10^{15} (!). The data for these measurements is presented in Figure 6.2.

6.1.2 Backaction Cooling

In the same way as Section 5.4, we can cool the 5.1 GHz mechanical mode. Unfortunately, technical difficulties prevented the use of the device presented in the previous section. We use instead a device with $Q_o = 3.0 \times 10^5$, $\omega_o/2\pi = 194$ THz, $\kappa/2\pi = 650$ MHz, $\kappa_e/2\pi = 94$ MHz, $Q_m = 4.2 \times 10^5$, $\omega_m/2\pi = 5.1$ GHz, and $\gamma_i/2\pi = 12$ kHz. From a bath temperature of $\sim$10 K (achieved via cryostat improvements), we cool to a phonon occupation of 0.73 ± 0.07, with an optomechanical coupling rate of 867 kHz. These results are shown in Figure 6.3. As this is only a marginal improvement over the result from Section 5.4 (despite a significant improvement in device parameters), there appears

to be heating effects in these devices that we do not yet fully understand.

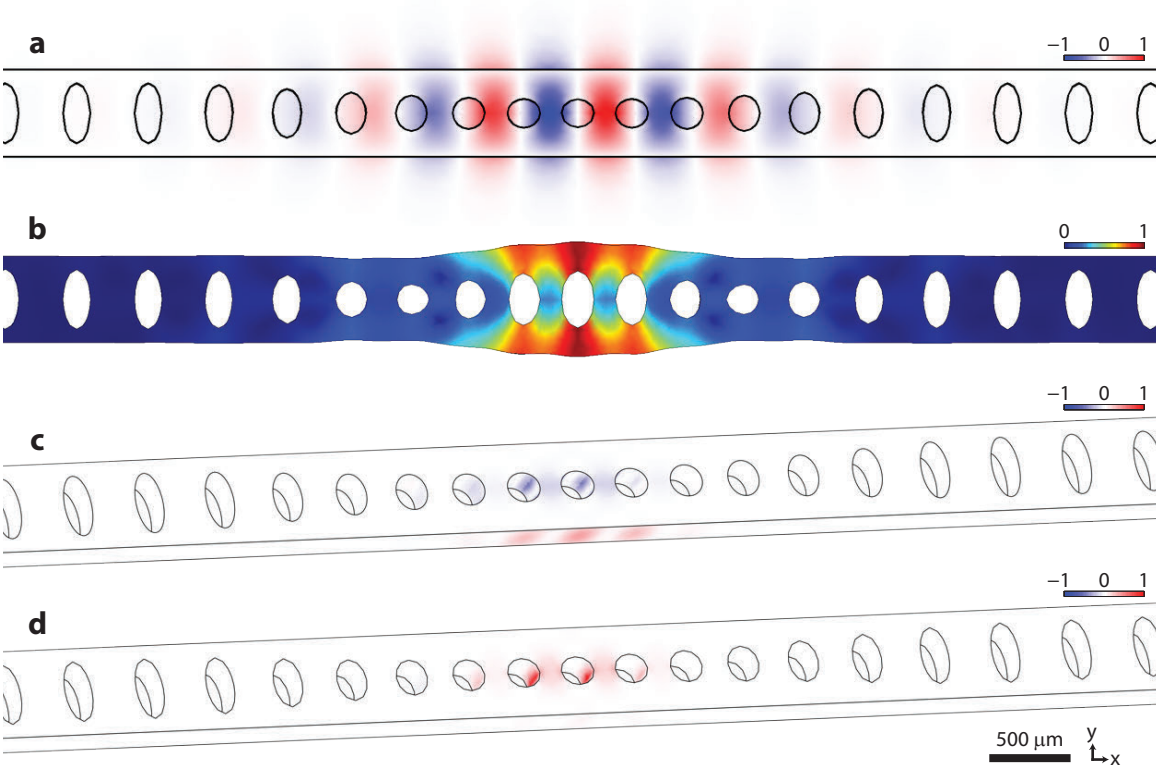

Figure 6.1: **FEM simulations of the 5GHF design.** FEM simulations corresponding to the normalized **a**, E_y field of the fundamental optical mode, **b**, displacement field, $|\boldsymbol{Q}|$, of the fundamental breathing mode, **c**, surface integrand in (3.39), showing the individual contributions to g_{mb}, and **d**, volume integrand in (3.47), showing the individual contributions to g_{pe}. While qualitatively seemingly very similar to the 5G design, both the mechanical frequency (5.7 GHz versus 4.2 GHz, simulated) and the optomechanical coupling rate (780 kHz versus 500 kHz, simulated) are significantly higher.

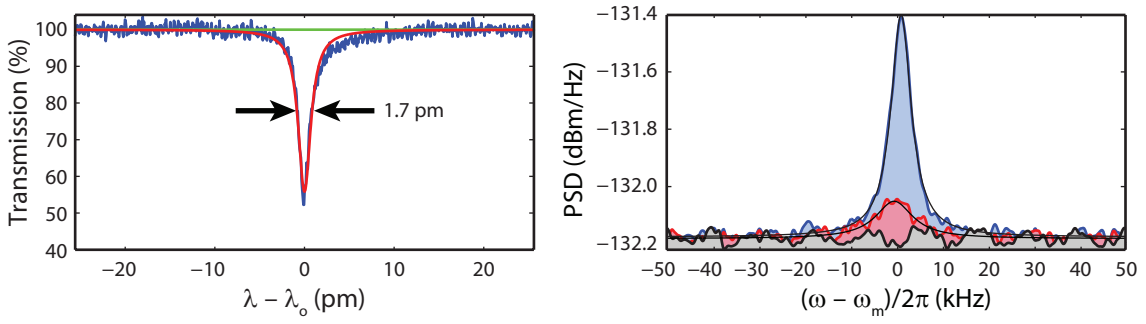

Figure 6.2: **5GHF device characterization.** **a**, The normalized optical transmission spectrum measured on D3 from which κ, κ_e, and ω_o are extracted. **b**, The mechanical noise spectrum measured around the resonance frequency of the breathing mode, ω_m, at cooperativity $C = 0.3$, for $\Delta = +\omega_m$ (red) and $\Delta = -\omega_m$ (blue), from which γ_i can be inferred. The black trace corresponds to the measured noise floor with the drive laser detuned far from the cavity resonance.

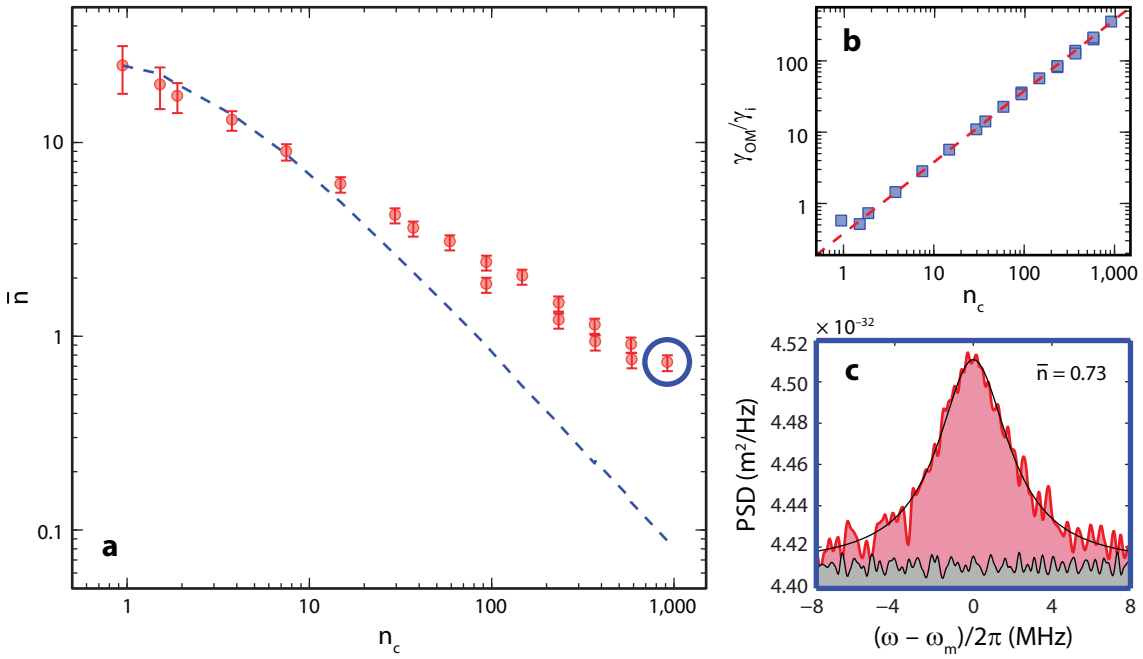

Figure 6.3: **5GHF backaction cooling.** **a**, Measured (○) average phonon number, $\bar{n}$, in the breathing mechanical mode at $\omega_m/2\pi = 5.1$ GHz versus cooling laser drive power (in units of intracavity photons, n_c), as deduced from the calibrated area under the Lorentzian lineshape of the mechanical noise power spectrum, $\widetilde{S}_P$. The dashed blue line indicates the estimated mode phonon number from the measured optical damping alone. Error bars indicate estimated uncertainties as outlined in Section 5.4.4. **b**, Measured cooperativity (□), with a linear fit (red dashed line) to estimate the zero-point optomechanical coupling rate ($g/2\pi = 867$ kHz). **c**, The measured noise power spectrum in units of m^2/Hz (using $x_{zpf} = 3.6$ fm, corresponding to the numerically computed motional mass for the breathing mode of $m_{eff} = 127$ fg) at the highest laser cooling power. Credit for this data goes to Amir Safavi-Naeini and Jeff Hill.

6.2 Free Space Couplers

The rapid development and characterization of nanobeam designs [52, 56, 57, 59, 60, 101] is in large part thanks to the extremely flexible, dimpled tapered fiber technology developed within the Painter group [69]. However, the coupling scheme does suffer from a few disadvantages. As mentioned at the beginning of Chapter 2, we have effectively a two-sided coupling scheme, so even in the best case, we have coupling to a "lost" channel (reflection) at a rate of $\kappa/2$. In addition, positioning the taper for evanescent coupling to a particular nanobeam without significantly perturbing the optical mode is a delicate task requiring a constant line of sight to the devices, a condition that is difficult to achieve if we move to lower temperature cryogenic setups. Related is the issue that stable coupling generally requires touching the taper to the silicon surface, and for a taper that is ~2 μm in diameter (compared to nanobeams that are <1 μm wide), this can lead to a significant reduction in optical and

mechanical quality factors if the taper is inadvertently touching the nanobeam itself. Lastly, since the taper is formed by heating and stretching an optical fiber, weakening its structural integrity, the thermal gradients induced by the transition to cryogenic conditions can cause the taper to break, a problem that plagued the experiment in Section 5.4 for several months. We briefly outline here an alternative, vertical free-space coupling scheme using a ball lense fiber that addresses some of these issues, while maintaining many of the taper coupling scheme advantages (Appendix D.6).

Similar to the well-known grating couplers [128–135], the challenge of free space coupling from an optical fiber to an integrated SOI waveguide is the significant mismatch between the single-mode fiber mode profile (confined to a core region of ∼10 μm) and the mode profile of an in-plane waveguide mode (confined to a width and thickness of <1 μm). While theoretical power coupling efficiencies in grating couplers can exceed 90% [130], typical demonstrated values are closer to ∼30% in large planar SOI designs (>80 μm long), with significant improvements to ∼60%−70% by introducing fabrication complications such as nonuniform etching [134], an additional silicon overlay [133], or substrate engineering [136]. We propose instead a coupler based on mode-matching a Gaussian beam profile to the far field of an optical resonance in a highly tailorable, quasi-2D optical cavity. This cavity is then coupled to a low loss W1 waveguide for in-plane routing [137].

6.2.1 Numerical Simulations

We require a low quality factor optical mode (ideally $Q_o < 100$ for a coupler bandwidth >15 nm) with a far field that has a large overlap integral with a Gaussian beam mode. The electric field amplitude of the latter is given in cylindrical coordinates, with $\hat{z}$ along the axial direction of the beam, by [138]

$$E_b(r,z) = E_0 \frac{w_0}{w(z)} \exp\left(-\frac{r^2}{w^2(z)}\right) \exp\left(-ikz - ik\frac{r^2}{2R(z)} + i\zeta(z)\right), \tag{6.1}$$

where E_0 is the beam amplitude, $w(z) \equiv w_0\sqrt{1+(z/z_R)^2}$ is the beam width, w_0 is the minimum beam radius (beam waist), $z_R = \pi w_0^2/\lambda_o$ is the Rayleigh range, λ_o is the optical wavelength, $R(z) \equiv z(1+(z_R/z)^2)$ is the radius of curvature, and $\zeta(z) \equiv \arctan(z/z_R)$ is the Gouy phase. A direct finite element simulation of the far field of an optical cavity mode is quite computationally expensive (requiring a simulation volume comparable to the far field distance, typically several microns). Instead, we simulate a much smaller volume and use the principles discussed in Section 3.2 to infer the far field from the near field simulations. Taking a 2D spatial fast Fourier transform (FFT) of the dominant electric field polarization in a plane above the crystal surface yields the modal distribution of in-plane k-vector component amplitudes, $k_\parallel = \sqrt{k_x^2 + k_y^2}$. Modes that can propagate without exponential decay in free space correspond to $k_\parallel < \omega_o/c = |\boldsymbol{k}|$ so we retain only $k_\parallel$ components satisfying this inequality. We then evolve this modal distribution over a distance of h by multiplying

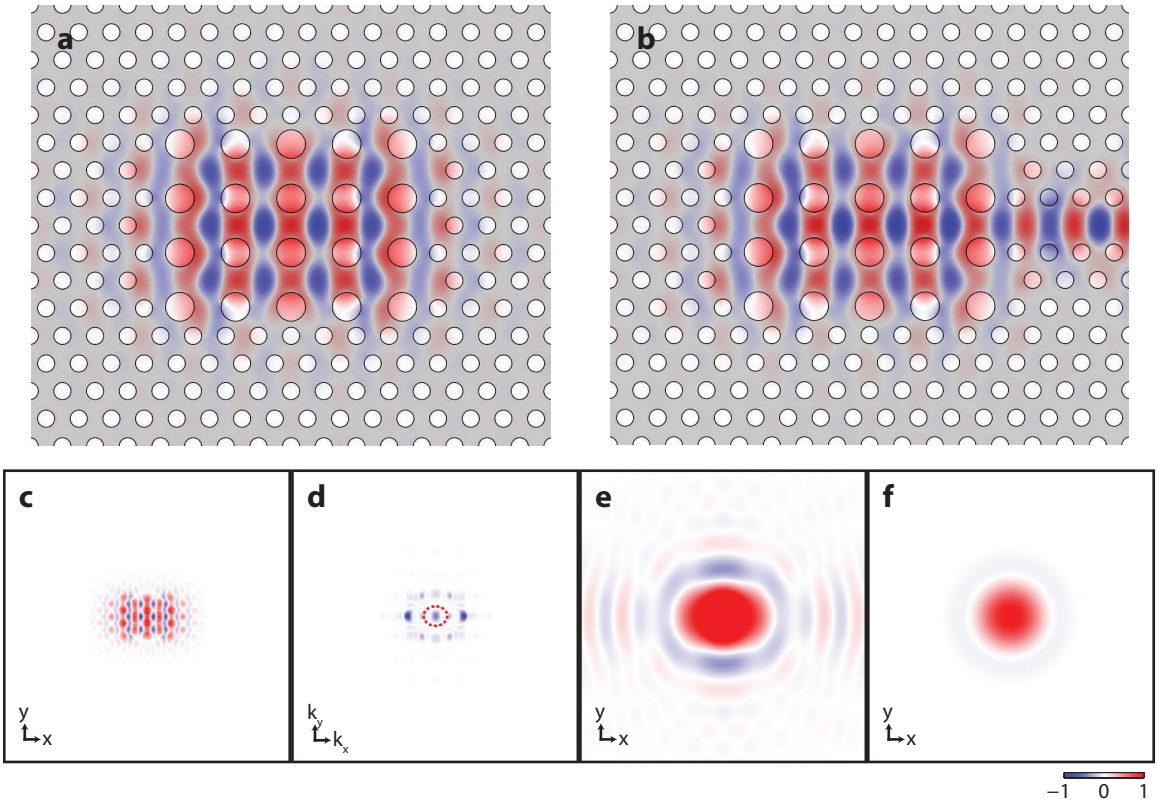

Figure 6.4: **Numerical simulations of a free-space coupler.** **a**, a 2D FEM simulation of a candidate coupler mode without a coupling waveguide (normalized E_y plotted), showing an exterior crystal region (small circles) with a complete photonic bandgap at 1,550 nm acting as the "mirror" for the lossy optical cavity mode in the coupling region (large circles). The gray indicates 220 nm silicon while the white indicates an air hole. **b**, The same structure with a W1 waveguide. It is desirable for the loss in the $\hat{y}$ direction to match the loss in the $\hat{z}$ direction (out of the page). **c**, A slice of E_y from **a**, taken just above the silicon substrate, **d**, the 2D spatial FFT of **c**, **e**, the "propagated" version of **c**, and, **f**, the best-fit Gaussian beam mode profile with $\xi = 0.94$.

the propagating components with $\exp(ih\sqrt{|\boldsymbol{k}| - k_{\|}})$. Finally, we revert back to the coordinate basis by inverse 2D FFT, resulting in the far field spatial electric field mode distribution, $E'_y(x, y)$. We then perform a fit of this spatial distribution to (6.1), keeping the beam waist (w_0), waist height (z), beam radius (r) and amplitude (E_0) as free parameters, with the goodness of fit determined by the mode overlap integral

$$\xi = \frac{\iint dxdy\, |E'_y(x,y) E_b(x,y,z)|}{\iint dxdy\, |E'_y(x,y)||E_b(x,y,z)|}. \tag{6.2}$$

Thus, each cavity mode can be characterized by a best-fit set of beam parameters and a normalized mode overlap of the far field. We can then introduce the W1 waveguide and look for modes that have matched loss rates between the W1 waveguide and the vertical, $\hat{z}$ direction. This entire procedure is summarized in Figure 6.4.

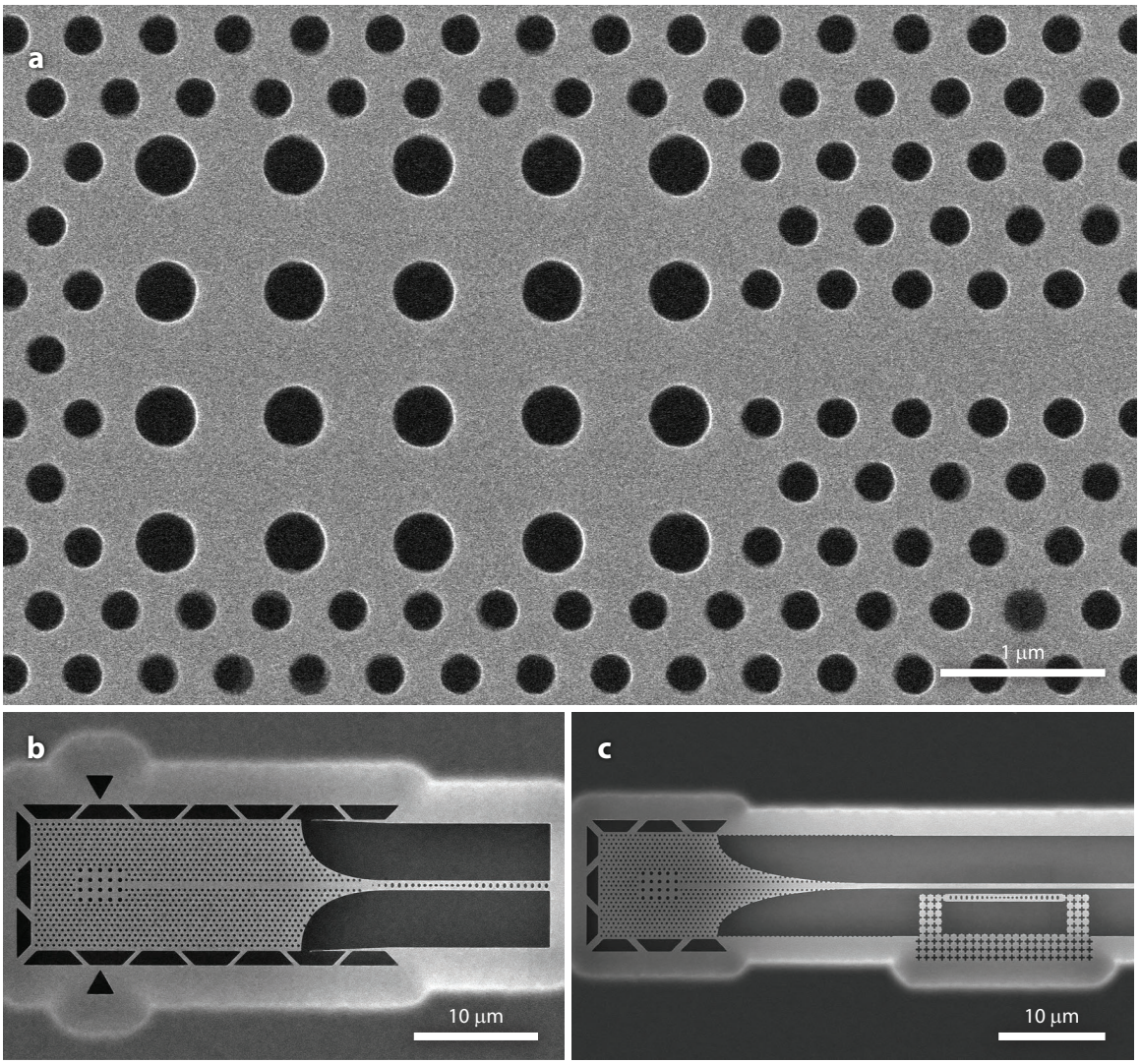

Figure 6.5: **SEM image of a free-space coupler and related designs.** **a**, Zoomed-in view of a fabricated free-space coupler showing the coupling region and the W1 waveguide. The W1 waveguide acts as a generic port for the free-space couplers, allowing them to be easily combined with a variety of photonic crystal cavity geometries, such as **b**, butt coupled to a 5G device so we have the desired one-sided coupling scheme, or **c**, side coupled to a nanobeam allowing a phononic shield to be maintained around the device.

6.2.2 Fabrication and Preliminary Results

As with the other devices in this work, the waveguide couplers can be fabricated following the procedure in Section 4.1, with scanning electron microscope (SEM) images of the results shown in Figure 6.5. Characterization is done using a ball lens fiber mounted on a set of Suruga Seiki motorized linear stage (for all three axis). For the device in Figure 6.5b, an example of a measured wavelength-dependent reflection spectrum is shown in Figure 6.6. Currently, we can obtain an in–out coupling efficiency of ∼20% (one way losses are ∼3.5 dB), indicating further refinement is required.

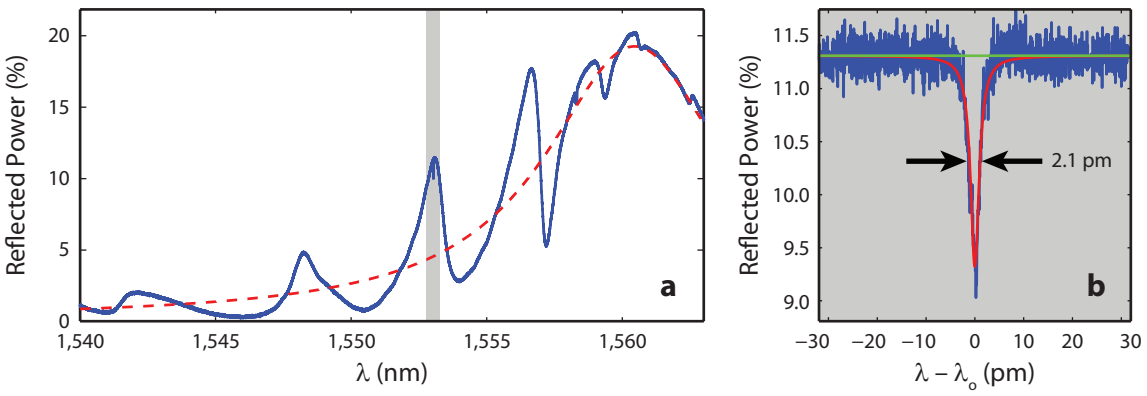

Figure 6.6: **Optical characterization of a free-space coupler.** The free-space coupler is butt coupled to a 5G device. **a**, A broad wavelength scan of the reflection response of the butt-coupled free-space coupler. The broad peak indicated with the dashed red lie is the lossy free-space coupler cavity mode (with a 3 dB bandwidth of ∼8 nm or ∼100 GHz and peak in–out coupling efficiency of 20%). Further experimentation needs to be done to understand the fringe pattern modulating this peak. We can also see a narrow linewidth dip in the gray region corresponding to the optical cavity mode of the 5G device. **b**, A narrow wavelength scan of the gray region in **a**, showing an optical resonance with a Q_o of 7.3×10^5. Credit for the data goes to Simon Gröblacher.

6.3 Motional Sideband Asymmetry

In the measurement performed in Section 5.4, the spectral signature imprinted by the mechanical motion of the oscillator is directly proportional to the mechanical mode occupancy, $\bar{n}$. Consequently, an occupancy approaching zero manifests as a vanishing signal; the zero-point motion of the nanobeam is hidden, and there is no clear indication that the quantum regime has been breached. This is because S_{bb} (the spectral density the signal is proportional to) is a measure of the mechanical system's ability to *emit* energy (or from the experimentalist's perspective, the ability to *extract* energy from the mechanics), and it is well-known that zero-point motion cannot do work [139]. These quantum fluctuations can, however, are very capable of *absorbing* energy, a process described by $S_{b^\dagger b^\dagger}$ [122]. Using (2.47) and the correlations given by (2.49)–(2.54), we can write a simple expression for S_{bb} and $S_{b^\dagger b^\dagger}$ in the absence of a coupled optical field (by setting $\alpha_0 = 0$),

$$S_{bb}(\omega) = \frac{\gamma_i n_b}{(\omega_m + \omega)^2 + (\gamma_i/2)^2} \tag{6.3}$$

$$S_{b^\dagger b^\dagger}(\omega) = \frac{\gamma_i (n_b + 1)}{(\omega_m - \omega)^2 + (\gamma_i/2)^2}. \tag{6.4}$$

For the position operator $\hat{x} = x_{\text{zpf}}(\hat{b}^\dagger + \hat{b})$, we have an asymmetric (in the positive and negative frequency components) displacement spectrum

$$\begin{aligned} S_{xx}(\omega) &= S_{b^\dagger b^\dagger}(\omega) + S_{bb}(\omega) \\ &= x_{\text{zpf}}^2 \left(\frac{\gamma_i(n_b+1)}{(\omega_m-\omega)^2 + (\gamma_i/2)^2} + \frac{\gamma_i n_b}{(\omega_m+\omega)^2 + (\gamma_i/2)^2} \right), \end{aligned} \tag{6.5}$$

which recovers the classical displacement spectrum (with equal sideband amplitudes) in the large n_b limit. We see then the asymmetry arises from the finite commutation relation of $\hat{b}$ and $\hat{b}^\dagger$, a purely quantum phenomenon.

6.3.1 Observing Zero-Point Motion

In [140], Safavi-Naeini et al. use the 5G devices to demonstrate this spectral asymmetry using an additional probe laser and a second optical cavity mode as a filter to select a particular (positive or negative) frequency component of the displacement spectrum. For $\Delta = \omega_m$ (of the probe), the resulting spectrum is given by (2.63) with a modification to the cooling-beam-only damped phonon occupation, $\bar{n}$, resulting from backaction of the probe beam (expressed as the probe cooperativity, C_p),

$$S_{NN,+} = 1 + \frac{4\kappa_e|G|^2}{\kappa^2} \bar{S}_{bb}\left(\omega; \frac{\bar{n}}{1+C_p}\right). \tag{6.6}$$

We can derive a similar expression for $\Delta = -\omega_m$ (assuming a weak probe) where we have instead of (2.62),

$$\begin{aligned} S_{NN,-}(\omega) &= \int_{-\infty}^{\infty} d\omega'\, t_-(\omega)t^*(-\omega')\langle \hat{a}_{\text{in}}(\omega)\hat{a}_{\text{in}}^\dagger(\omega')\rangle + \eta_-(\omega)\eta_-^*(-\omega')\langle \hat{a}_{\text{in},i}(\omega)\hat{a}_{\text{in},i}^\dagger(\omega')\rangle \\ &\quad + s_{12,-}(\omega)s_{12,-}^*(-\omega')\langle \hat{b}_{\text{in}}^\dagger(\omega)\hat{b}_{\text{in}}(\omega')\rangle + s_{12,-}^*(-\omega)s_{12,-}(\omega')\langle \hat{b}_{\text{in}}(\omega)\hat{b}_{\text{in}}^\dagger(\omega')\rangle \\ &= |t_-(\omega)|^2 + |\eta_-(\omega)|^2 + |s_{12,-}(-\omega)|^2 + n_b(|s_{12,-}(\omega)|^2 + |s_{12,-}(-\omega)|^2) \\ &= 1 + \frac{4\kappa_e|G|^2}{\kappa^2}\frac{\gamma_i(\bar{n}+1)}{2}\left(\frac{1}{(\omega_m-\omega)^2+(\gamma/2)^2} + \frac{1}{(\omega_m+\omega)^2+(\gamma/2)^2}\right) \\ &= 1 + \frac{4\kappa_e|G|^2}{\kappa^2}\bar{S}_{b^\dagger b^\dagger}\left(\omega; \frac{\bar{n}+1}{1-C_p}\right), \end{aligned} \tag{6.7}$$

having used $t_-(\omega)^2 + \eta_-(\omega)^2 = 1 + |s_{12,-}(\omega)|^2$ valid for blue side driving. Integrating (6.6) and (6.7) near ω_m (with appropriate proportionality constants and after subtracting the shot-noise background) yields the respective spectral power near ω_m, $P_{\omega_m,+}$ (anti-Stokes sideband power; proportional to $\frac{\bar{n}}{1+C_p}$) and $P_{\omega_m,-}$ (Stokes sideband power; proportional to $\frac{\bar{n}+1}{1-C_p}$). The asymmetry

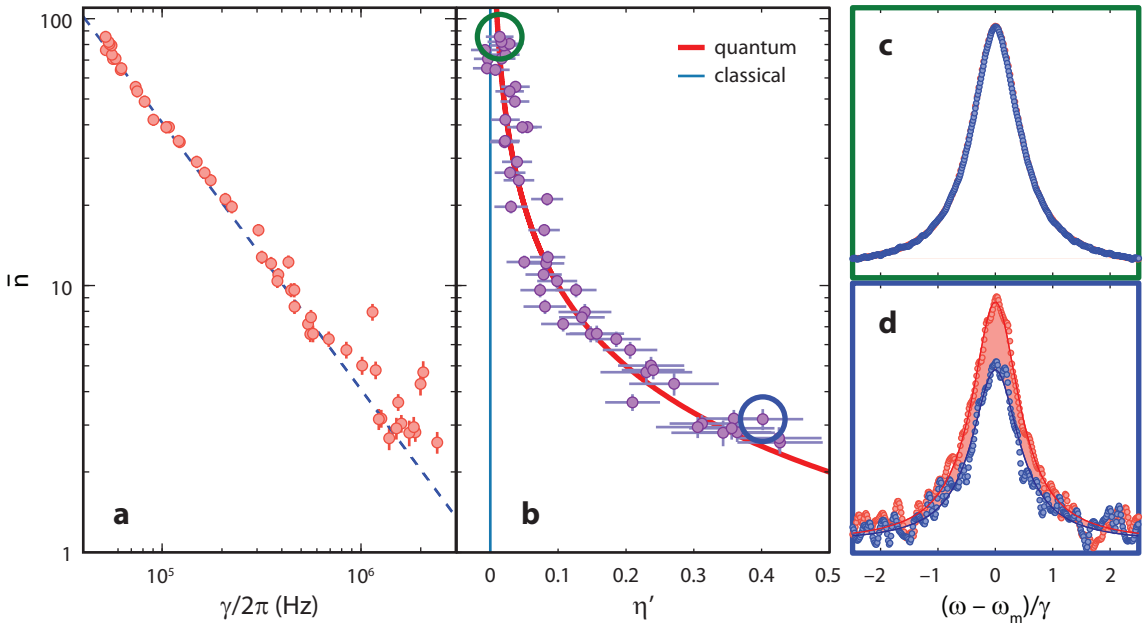

Figure 6.7: **Measuring zero-point motion.** From [140]. **a**, The mechanical mode occupancy, $\bar{n}$, as a function of measured mechanical mode linewidth, γ, with estimated mode phonon number from the measured optical damping alone (blue dashed line), given by $\gamma_i n_b/(\gamma - \gamma_i)$. **b**, The measured asymmetry, η' (defined in the text), as a function of $\bar{n}$ (vertical axis) with the theoretical quantum (red line) and classical behavior (blue line). For the highlighted asymmetry points, **c**, $\bar{n} = 85$ phonons, and **d**, $\bar{n} = 3.2$ phonons, the measured Stokes (red) and anti-Stokes (blue) sideband spectra are plotted superimposed on a linewidth normalized x-axis to highlight the asymmetry in the area (red region).

(adjusting for the the probe cooperativity), is given by

$$\eta' \equiv \frac{P_{\omega_m,-}/P_{\omega_m,+}}{1+C_p} - \frac{1}{1-C_p} = \frac{1}{\bar{n}}. \tag{6.8}$$

In the experiment, an asymmetry of $\eta' \approx 40\%$ is measured at the minimum achieved phonon occupation of $\bar{n} = 2.6 \pm 0.2$, showing good correspondence to the theoretical expectation. These results are summarized in Figure 6.7.

Appendix A

Mathematical Definitions

A.1 Fourier Transform

For an operator, $\hat{O}$, the Fourier transform pair is defined to be [141]

$$\hat{O}(t) = \frac{1}{\sqrt{2\pi}} \int_{-\infty}^{\infty} d\omega \, e^{-i\omega t} \hat{O}(\omega), \tag{A.1}$$

$$\hat{O}(\omega) = \frac{1}{\sqrt{2\pi}} \int_{-\infty}^{\infty} dt \, e^{i\omega t} \hat{O}(t). \tag{A.2}$$

We note specifically that

$$\begin{aligned} \left(\hat{O}(-\omega)\right)^{\dagger} &= \left(\frac{1}{\sqrt{2\pi}} \int_{-\infty}^{\infty} d\omega \, e^{-i\omega t} \hat{O}(t)\right)^{\dagger} \\ &= \frac{1}{\sqrt{2\pi}} \int_{-\infty}^{\infty} d\omega \, e^{i\omega t} \hat{O}^{\dagger}(t) \\ &= \hat{O}^{\dagger}(\omega). \end{aligned} \tag{A.3}$$

A.2 Delta Functions

Several properties of the Dirac delta function $\delta(x)$ are listed here [141].

$$\int_{-\infty}^{\infty} dt \, \delta(t) = 1 \tag{A.4}$$

$$\int_{-\infty}^{\infty} dt \, f(t)\delta(t - t_0) = f(t_0) \tag{A.5}$$

$$\int_{-\infty}^{t_0} dt \, f(t)\delta(t - t_0) = \frac{1}{2} f(t_0) \tag{A.6}$$

$$\int_{-\infty}^{\infty} d\omega \, e^{i\omega(t - t_0)} = 2\pi\delta(t - t_0) \tag{A.7}$$

Related is the Kronecker delta function

$$\delta_{ij} = \begin{cases} 0, & \text{if } i \neq j, \\ 1, & \text{if } i = j. \end{cases} \tag{A.8}$$

A.3 Spectral Density

The spectral density of an operator $\hat{O}$ is defined as

$$S_{OO}(\omega) = \int_{-\infty}^{\infty} d\tau \, e^{i\omega\tau} \langle \hat{O}^\dagger(t+\tau)\hat{O}(t) \rangle, \tag{A.9}$$

where $\langle \cdots \rangle$ indicates an ensemble average [74]. Using the definitions from above and assuming $\hat{O}$ is stationary, the spectral density can also be written as

$$\begin{aligned} S_{OO}(\omega) &= \frac{1}{2\pi} \int_{-\infty}^{\infty} d\tau \, e^{i\omega\tau} \left\langle \int_{-\infty}^{\infty} d\omega' \, e^{-i\omega'(t+\tau)} \hat{O}^\dagger(\omega') \int_{-\infty}^{\infty} d\omega'' \, e^{-i\omega'' t} \hat{O}(\omega'') \right\rangle \\ &= \int_{-\infty}^{\infty} d\omega' \langle e^{2i\omega' t} \hat{O}^\dagger(\omega) \hat{O}(\omega') \rangle \\ &= \int_{-\infty}^{\infty} d\omega' \langle \hat{O}^\dagger(\omega) \hat{O}(\omega') \rangle. \end{aligned} \tag{A.10}$$

We further define the symmetrized spectral density as $\bar{S}_{OO} = (S_{OO}(\omega) + S_{OO}(-\omega))/2$ and the one-sided spectral density as $\bar{S}_O(\omega) = 2\bar{S}_{OO}$. The latter is the measurement made by the spectrum analyzer. The average oscillating power in a $\pm\delta$ window around ω is

$$P_\omega = \frac{1}{2\pi} \int_{\omega-\delta}^{\omega+\delta} d\omega' \, \bar{S}_O(\omega'). \tag{A.11}$$

A.4 Commutation Relations

The commutator of two operators $\hat{A}$ and $\hat{B}$ is defined $[\hat{A}, \hat{B}] = \hat{A}\hat{B} - \hat{B}\hat{A}$. We list several useful identities here [81].

$$[\hat{A}, \hat{A}] = 0 \tag{A.12}$$

$$[\hat{A}, \hat{B}] = -[\hat{B}, \hat{A}] \tag{A.13}$$

$$[\hat{A}, \hat{B}\hat{C}] = \hat{B}[\hat{A}, \hat{C}] + [\hat{A}, \hat{B}]\hat{C} \tag{A.14}$$

$$e^{\hat{A}} \hat{B} e^{-\hat{A}} = \hat{B} + [\hat{A}, \hat{B}] + \frac{1}{2!}[\hat{A}, [\hat{A}, \hat{B}]] + \frac{1}{3!}[\hat{A}, [\hat{A}, [\hat{A}, \hat{B}]]] + \cdots (*) \tag{A.15}$$

*This is the Campbell-Baker-Hausdorff expansion.

We note for the special case of creation ($\hat{a}^\dagger$) and annihilation ($\hat{a}$) operators with the canonical commutation relation $[\hat{a}, \hat{a}^\dagger] = 1$, for some scalar quantity λ, we have the identity

$$\begin{aligned} e^{\lambda \hat{a}^\dagger \hat{a}} \hat{a} e^{-\lambda \hat{a}^\dagger \hat{a}} &= \hat{a} + \lambda[\hat{a}^\dagger \hat{a}, \hat{a}] + \frac{\lambda^2}{2!}[\hat{a}^\dagger \hat{a}, [\hat{a}^\dagger \hat{a}, \hat{a}]] + \frac{\lambda^3}{3!}[\hat{a}^\dagger \hat{a}, [\hat{a}^\dagger \hat{a}, [\hat{a}^\dagger \hat{a}, \hat{a}]]] + \cdots \\ &= \hat{a}\left(1 + (-\lambda) + \frac{(-\lambda)^2}{2!} + \frac{(-\lambda)^3}{3!} + \cdots\right) \\ &= \hat{a} e^{-\lambda}, \end{aligned} \tag{A.16}$$

having used $[\hat{a}^\dagger \hat{a}, \hat{a}] = [\hat{a}^\dagger, \hat{a}]\hat{a} = -\hat{a}$ and (A.15). We also have

$$e^{\lambda^* \hat{a}^\dagger \hat{a}} \hat{a}^\dagger e^{-\lambda \hat{a}^\dagger \hat{a}} = \hat{a}^\dagger e^{\lambda}. \tag{A.17}$$

A.5 Differential Equations

First-order differential equations of the form $\frac{d}{dt}y(t) = \dot{y}(t) = p(t)y(t) + q(t)$ have the solution

$$y(t) = \frac{\int dt\, e^{-\int^t dt'\, p(t')} q(t) + C}{e^{-\int^t dt'\, p(t')}}, \tag{A.18}$$

where C is a constant dependent on the initial conditions [142].

A.6 Trigonometric Identities

We list some useful trigonometric identities here.

$$\sin(A + B) = \sin(A)\cos(B) + \sin(B)\cos(A) \tag{A.19}$$

$$\cos(A + B) = \cos(A)\cos(B) - \sin(B)\sin(A) \tag{A.20}$$

A.7 Lorentzian Function

The Lorentzian function has the form

$$L(\omega) = \frac{1}{\pi} \frac{\gamma/2}{(\omega - \omega_0)^2 + (\gamma/2)^2}, \tag{A.21}$$

with a single peak at ω_0, with a full width at half maximum (FWHM) of γ and an amplitude of $2/\gamma\pi$. In this form, we have the area conveniently given by

$$\int_{-\infty}^{\infty} d\omega\, L(\omega) = 1. \tag{A.22}$$

We also note the useful relationship

$$\frac{(\omega-\omega_0)^2+(\gamma_2/2)^2}{(\omega-\omega_0)^2+(\gamma_1/2)^2}=1-\frac{(\gamma_1/2)^2-(\gamma_2/2)^2}{(\omega-\omega_0)^2+(\gamma_1/2)^2}, \tag{A.23}$$

describing an offset, inverted Lorentzian.

A.8 Contracted Index Notation

A symmetric tensor can be represented in lower order using Voigt notation, essentially a mapping of indices [143]. For a rank 4 tensor, $\boldsymbol{T}$, satisfying $T_{ijmn}=T_{jimn}=T_{ijnm}=T_{mnij}$ the mapping

$$\begin{aligned} xx &\rightarrow 1,\\ yy &\rightarrow 2,\\ zz &\rightarrow 3,\\ yz, zy &\rightarrow 4,\\ xz, zx &\rightarrow 5,\\ xy, yx &\rightarrow 6. \end{aligned} \tag{A.24}$$

reduces the $3\times3\times3\times3$ tensor to a 6×6 matrix.

Appendix B

Quantum Input–Output Theory

Physical systems do not exist in isolation but we often consider them as such to create a tractable problem for analysis. Careful consideration of what to consider the "system", containing the interesting degrees of freedom and what to consider the environment (everything else) is crucial in providing an accurate description of dynamics. However, there are many problems for which the environment cannot be ignored. One solution is to approximate the environment as a "heat bath", and consider its action on the system as a random perturbative force, an idea originally used to describe the classical motion of a Brownian particle in a viscous fluid [144]. Such an idealization has been successful in describing otherwise complicated systems, and further gives rise to the fluctuation–dissipation theorem [145], in that such a random force is responsible for both the erratic motion of a particle at rest and the drag on the particle in motion. We show here the quantum analogue of these ideas, following the treatments by [146–150].

B.1 Quantum Langevin Equation

This discussion is geared toward writing an equation describing the dynamics of a cavity (the system) coupled to an exterior electromagnetic field (the bath). We begin by idealizing the bath as set of independent harmonic oscillators with the bath Hamiltonian given by

$$\hat{H}_{\text{bath}} = \hbar \sum_{q} \omega_q \hat{b}_q^\dagger \hat{b}_q, \tag{B.1}$$

where q is the quantum number labeling the bath mode and $\hat{b}$ is the typical boson annihilation operator satisfying the canonical commutation relation $[\hat{b}_q, \hat{b}_{q'}^\dagger] = \delta_{qq'}$. No particular structure is ascribed to system Hamiltonian, $\hat{H}_{\text{sys}}$, only that it has a system operator $\hat{d}$ that interacts with the

heat bath linearly via

$$\hat{H}_{\text{int}} = i\hbar \sum_q \kappa_q (\hat{d} - \hat{d}^\dagger)(\hat{b}_q + \hat{b}_q^\dagger), \tag{B.2}$$

with some quantum number dependent coupling κ_q, so the total Hamiltonian can be written as

$$\hat{H} = \hat{H}_{\text{sys}} + \hat{H}_{\text{bath}} + \hat{H}_{\text{int}}. \tag{B.3}$$

Rotating Wave Approximation. We first assume that in the absence of $\hat{H}_{\text{int}}$, the time evolution of $\hat{d}$ is simply $\hat{d}(t) = \hat{d}e^{-i\omega_o t}$ where $\omega_o \gg 1$ is the resonant frequency of the system. To shift to an interaction picture with respect to the free evolution of only the system and the bath, we apply the unitary transformation

$$\hat{U}(t) = e^{-\frac{i}{\hbar}(\hat{H}_{\text{bath}} + \hat{H}_{\text{sys}})t}, \tag{B.4}$$

so that using (A.16) and (A.17), the interaction Hamiltonian is now

$$H_{\text{int}} \to \hat{U}^\dagger H_{\text{int}} \hat{U} = i\hbar \sum_q \kappa_q \left(\hat{d}e^{-i\omega_o t} - \hat{d}^\dagger e^{i\omega_o t}\right)\left(\hat{b}_q e^{-i\omega t} + \hat{b}_q^\dagger e^{i\omega t}\right). \tag{B.5}$$

We can make the continuum approximation

$$\sum_q \kappa_q \to \int_0^\infty d\omega \, \frac{dq}{d\omega} \kappa_q = \int_0^\infty d\omega \, \kappa(\omega), \tag{B.6}$$

where the mode density terms have been absorbed into $\kappa(\omega)$, giving

$$H_{\text{int}} = i\hbar \int_0^\infty d\omega \kappa(\omega) \left(\hat{d}\hat{b}(\omega)e^{-i(\omega_o+\omega)t} - \hat{b}^\dagger(\omega)\hat{d}^\dagger e^{i(\omega_o+\omega)t} + \hat{d}\hat{b}^\dagger(\omega)e^{-i(\omega_o-\omega)t} - \hat{b}(\omega)\hat{d}^\dagger e^{i(\omega_o-\omega)t}\right). \tag{B.7}$$

where $\hat{b}(\omega)$ satisfies $[\hat{b}(\omega), \hat{b}^\dagger(\omega')] = \delta(\omega - \omega')$. We now have terms proportional to $e^{\pm i(\omega+\omega_o)t}$ and $e^{\pm i(\omega-\omega_o)t}$. The former are rapidly oscillating when compared to the latter, having a vanishing cycle average on the $1/\omega_o$ timescale and can be neglected—the rotating wave approximation. For a more physical argument, if we consider $\hat{d}$ to be a boson annihilation operator of a cavity mode, we see that the terms $\hat{d}\hat{b}$ and $\hat{b}^\dagger\hat{d}^\dagger$ respectively represent the simultaneous destruction and simultaneous creation of a bath and system quanta, violating energy conservation. Either reasoning allows the

interaction term to be rewritten,

$$\hat{H}_{\text{int}} = i\hbar \sum_q \kappa_q \left(\hat{d}\hat{b}_q^\dagger - \hat{b}_q \hat{d}^\dagger \right). \tag{B.8}$$

The Heisenberg equations of motion for some operator $\hat{O}$ is given by $\dot{\hat{O}}(t) = -\frac{i}{\hbar}[\hat{O}, \hat{H}]$ so we have immediately

$$\dot{\hat{b}}_q(t) = -i\omega_q \hat{b}_q(t) + \kappa_q \hat{d}(t), \tag{B.9}$$

and for some other system operator $\hat{a}$,

$$\dot{\hat{a}}(t) = -\frac{i}{\hbar}[\hat{a}, \hat{H}_{\text{sys}}] + \sum_q \kappa_q \left([\hat{a}, \hat{d}]\hat{b}_q^\dagger(t) - \hat{b}_q(t)[\hat{a}, \hat{d}^\dagger] \right). \tag{B.10}$$

We would like an independent expression for $\dot{\hat{a}}$ so we first solve (B.9) using (A.18) to obtain

$$\hat{b}_q(t) = e^{-i\omega_q(t-t_0)}\hat{b}_q(t_0) + \kappa_q \int_{t_0}^{t} dt'\, e^{-i\omega_q(t-t')}\hat{d}(t'), \tag{B.11}$$

where $\hat{b}_q$ has some initial value $\hat{b}_q(t_0)$ at time $t_0 < t$. Direct substitution into (B.10) yields

$$\begin{aligned}\dot{\hat{a}}(t) = -\frac{i}{\hbar}[\hat{a}, \hat{H}_{\text{sys}}] &+ \sum_q \kappa_q \left(e^{i\omega_q(t-t_0)}[\hat{a}, \hat{d}]\hat{b}_q^\dagger(t_0) - e^{-i\omega_q(t-t_0)}\hat{b}_q(t_0)[\hat{a}, \hat{d}^\dagger] \right) \\ &+ \sum_q \kappa_q^2 \int_{t_0}^{t} dt' \, \left(e^{i\omega_q(t-t')}[\hat{a}, \hat{d}]\hat{d}^\dagger(t') - e^{-i\omega_q(t-t')}\hat{d}(t')[\hat{a}, \hat{d}^\dagger] \right).\end{aligned} \tag{B.12}$$

First Markov Approximation. We again make the continuum approximation so the last term becomes

$$\begin{aligned}\sum_q \kappa_q^2 (\cdots) &\to \int_0^\infty d\omega\, \kappa(\omega)^2 \int_{t_0}^{t} dt' \, \left(e^{i\omega(t-t')}[\hat{a}, \hat{d}]\hat{d}^\dagger(t') - e^{-i\omega(t-t')}\hat{d}(t')[\hat{a}, \hat{d}^\dagger] \right) \\ &= \int_{-\infty}^\infty d\omega\, \kappa(\omega + \omega_o)^2 \int_{t_0}^{t} dt' \, \left(e^{i(\omega+\omega_o)(t-t')}[\hat{a}, \hat{d}]\hat{d}^\dagger(t') - e^{-i(\omega+\omega_o)(t-t')}\hat{d}(t')[\hat{a}, \hat{d}^\dagger] \right),\end{aligned} \tag{B.13}$$

where the substitution of $\omega \to \omega + \omega_o$ allows the lower limit of the integral to be closely approximated by $-\infty$ for $\omega_o \gg 1$. We assume that the coupling constant is frequency independent, and define

$$\kappa(\omega) = \sqrt{\frac{\gamma}{2\pi}}, \tag{B.14}$$

so that

$$\int_{-\infty}^{\infty} d\omega\, \kappa(\omega+\omega_o)^2 \int_{t_0}^{t} e^{\pm i\omega(t-t')} \to \frac{\gamma}{2\pi}\int_{t_0}^{t}\delta(t-t'). \tag{B.15}$$

This immediately allows (B.12) to be integrated (with the help of identities from Appendix A.2 and the continuum approximation) giving the quantum Langevin equation

$$\dot{\hat{a}}(t) = -\frac{i}{\hbar}[\hat{a},\hat{H}_{\text{sys}}] - \left(\left(\frac{\gamma}{2}\hat{d}(t)+\sqrt{\gamma}\hat{b}_{\text{in}}(t)\right)[\hat{a},\hat{d}^\dagger] - [\hat{a},\hat{d}]\left(\frac{\gamma}{2}\hat{d}^\dagger(t)+\sqrt{\gamma}\hat{b}^\dagger_{\text{in}}(t)\right)\right), \tag{B.16}$$

having defined an input field operator

$$\hat{b}_{\text{in}}(t) \equiv \frac{1}{\sqrt{2\pi}}\int_{-\infty}^{\infty} d\omega\, e^{-i\omega(t-t_0)}\hat{b}(\omega,t_0), \tag{B.17}$$

satisfying the canonical commutation relation

$$[\hat{b}_{\text{in}}(t),\hat{b}^\dagger_{\text{in}}(t')] = \frac{1}{2\pi}\int_{-\infty}^{\infty} d\omega \int_{-\infty}^{\infty} d\omega'\, e^{-i\omega(t-t_0)}e^{i\omega'(t'-t_0)}[\hat{b}(\omega,t_0),\hat{b}^\dagger(\omega',t_0)] = \delta(t-t'). \tag{B.18}$$

We note that in making this approximation, we remove the dependence of (B.12) on past values of the system operator $\hat{d}$, meaning future values of $\hat{a}$ depend only on the values of system operators in the present. This is equivalent to assuming the heat bath is strictly Markovian without memory, hence its namesake.

A similar analysis can be carried out for the case of an initial condition at $t_1 > t$. Analogous to (B.11),

$$\hat{b}_q(t) = e^{-i\omega_q(t-t_1)}\hat{b}_q(t_1) - \kappa_q\int_{t_1}^{t} dt'\, e^{-i\omega_q(t-t')}\hat{d}(t'), \tag{B.19}$$

and defining an output field operator

$$\hat{b}_{\text{out}}(t) \equiv \frac{1}{\sqrt{2\pi}}\int_{-\infty}^{\infty} d\omega\, e^{-i\omega(t-t_1)}\hat{b}(\omega,t_1), \tag{B.20}$$

the time-reversed quantum Langevin equation can be written as

$$\dot{\hat{a}}(t) = -\frac{i}{\hbar}[\hat{a},\hat{H}_{\text{sys}}] - \left(\left(-\frac{\gamma}{2}\hat{d}(t)+\sqrt{\gamma}\hat{b}_{\text{out}}(t)\right)[\hat{a},\hat{d}^\dagger] - [\hat{a},\hat{d}]\left(-\frac{\gamma}{2}\hat{d}^\dagger(t)+\sqrt{\gamma}\hat{b}^\dagger_{\text{out}}(t)\right)\right). \tag{B.21}$$

Equating (B.11) and (B.19), and integrating over ω in the continuum limit,

$$\begin{aligned}\frac{1}{\sqrt{2\pi}}\int_{-\infty}^{\infty} d\omega\, \hat{b}(\omega,t) &= \hat{b}_{\rm in}(t) + \frac{\sqrt{\gamma}}{2}\hat{d}(t) \\ &= \hat{b}_{\rm out}(t) - \frac{\sqrt{\gamma}}{2}\hat{d}(t),\end{aligned}$$

we have (by interpreting the $\hat{b}_{\rm in}$ and $\hat{b}_{\rm out}$ respectively as the inputs and outputs to the system) the boundary equation

$$\hat{b}_{\rm out}(t) - \hat{b}_{\rm in}(t) = \sqrt{\gamma}\hat{d}(t). \tag{B.22}$$

B.2 Input–Output Operator Correlations

To extract measurable physics, we must now make some assumptions about the state of the system so that quantum mechanical expectation values can be extracted. We assume that initially (at $t = t_0$), the system and bath are independent and non-interacting and that the bath operators satisfy

$$\langle \hat{b}(\omega,t_0)\rangle = 0, \tag{B.23}$$

$$\langle \hat{b}(\omega,t_0)\hat{b}(\omega',t_0)\rangle = 0, \tag{B.24}$$

$$\langle \hat{b}^\dagger(\omega,t_0)\hat{b}^\dagger(\omega',t_0)\rangle = 0, \tag{B.25}$$

$$\langle \hat{b}^\dagger(\omega,t_0)\hat{b}(\omega',t_0)\rangle = n_b(\omega)\delta(\omega-\omega'), \tag{B.26}$$

with $\langle\cdots\rangle$ indicating ensemble average. If the bath modes are independent and the density operator of each mode is diagonal in the number basis (random phase assumption), then the latter will be satisfied. We have immediately from (B.17)

$$\langle \hat{b}_{\rm in}(t)\rangle = 0, \tag{B.27}$$

$$\langle \hat{b}_{\rm in}(t)\hat{b}_{\rm in}(t')\rangle = 0, \tag{B.28}$$

$$\langle \hat{b}^\dagger_{\rm in}(t)\hat{b}^\dagger_{\rm in}(t')\rangle = 0. \tag{B.29}$$

More interestingly, we consider

$$\begin{aligned}\langle \hat{b}^\dagger_{\rm in}(t)\hat{b}_{\rm in}(t')\rangle &= \frac{1}{2\pi}\int_{-\infty}^{\infty} d\omega \int_{-\infty}^{\infty} d\omega'\, e^{i\omega(t-t_0)}e^{-i\omega'(t'-t_0)}\langle \hat{b}^\dagger(\omega,t_0)\hat{b}(\omega',t_0)\rangle \\ &= \int_{-\infty}^{\infty} d\omega\, e^{i\omega(t-t')}n_b(\omega) \\ &= n_b(\Omega)\delta(t-t'),\end{aligned} \tag{B.30}$$

where we assume that we are concerned with a small bandwidth $\delta\Omega$ about some large frequency Ω so that $n_b(\omega) \approx n_b(\Omega)$. Using the commutation relations for $\hat{b}(\omega)$ and $\hat{b}^\dagger(\omega)$, we also have

$$\langle \hat{b}_{\text{in}}(t)\hat{b}^\dagger_{\text{in}}(t')\rangle = (n_b(\Omega)+1)\delta(t-t'). \tag{B.31}$$

B.3 Single Mode Cavity Coupled to a Thermal Bath

For the special case of a thermal bath of bosons at equilibrium temperature T, coupled to a single mode cavity with resonant frequency Ω, we have $\hat{H}_{\text{sys}} = \hbar\Omega\hat{a}^\dagger\hat{a}$ and $n_b = 1/(e^{\hbar\Omega/k_BT}-1)$. The system interacts with the bath via the annihilation operator $\hat{a}$ so we immediately have the quantum Langevin equations

$$\dot{\hat{a}} = -i\Omega\hat{a} - \frac{\gamma}{2}\hat{a} - \sqrt{\gamma}\hat{b}_{\text{in}}(t), \tag{B.32}$$

$$\dot{\hat{a}}^\dagger = i\Omega\hat{a}^\dagger - \frac{\gamma}{2}\hat{a}^\dagger - \sqrt{\gamma}\hat{b}_{\text{in}}(t). \tag{B.33}$$

If we define the vector notation $\hat{\mathbf{O}} = [\hat{O}\ \hat{O}^\dagger]^T$ then Fourier transforming the Langevin equations shows a relation between the input and internal field of

$$\hat{\mathbf{a}}(\omega) = \frac{\sqrt{\gamma}}{\gamma/2 - i(\omega-\Omega)}\,\hat{\mathbf{a}}_{\text{in}}(\omega), \tag{B.34}$$

recovering the expected Lorentzian intensity transmission function of width $\gamma/2$. In the frequency domain, we also have correlation functions of the bath given by

$$\begin{aligned}\langle \hat{b}^\dagger_{\text{in}}(\omega)\hat{b}_{\text{in}}(\omega')\rangle &= \frac{1}{2\pi}\int_{-\infty}^{\infty} dt \int_{-\infty}^{\infty} dt\, e^{i\omega t}e^{i\omega' t'}\langle \hat{b}^\dagger_{\text{in}}(t)\hat{b}_{\text{in}}t')\rangle \\ &= n_b\delta(\omega+\omega') \qquad \text{(B.35)}\\ \langle \hat{b}_{\text{in}}(\omega)\hat{b}^\dagger_{\text{in}}(\omega')\rangle &= (n_b+1)\delta(\omega+\omega'). \qquad \text{(B.36)}\end{aligned}$$

Using (B.22) to eliminate the internal field, the transfer function between the input and output field is

$$\hat{\mathbf{a}}_{\text{out}}(\omega) = \frac{i(\omega-\Omega)+\gamma/2}{i(\omega-\Omega)-\gamma/2}\,\hat{\mathbf{a}}_{\text{in}}(\omega). \tag{B.37}$$

Appendix C

Rotated Photoelastic Tensor

Credit for this section goes to Seán Meenehan. If the coordinate system of the crystal unit cell is not aligned with the cavity coordinate system, we can apply a rotation transformation to the photoelastic tensor to align the two. From a practical standpoint, the silicon wafers used in the fabrication process are (100) wafers, so we are only concerned with in-plane rotation transformations of the form

$$\boldsymbol{R}(\theta) = \begin{bmatrix} \cos(\theta) & -\sin(\theta) & 0 \\ \sin(\theta) & \cos(\theta) & 0 \\ 0 & 0 & 1 \end{bmatrix}. \tag{C.1}$$

The rotated photoelastic tensor is given by

$$p'_{ijkl}(\theta) = R_{iq}(\theta)R_{jr}(\theta)R_{ks}(\theta)R_{lt}(\theta)p_{qrst}, \tag{C.2}$$

where the unrotated photoelastic tensor is given by (3.44). The elements of $\boldsymbol{p}'$ in the contracted index notation of (3.43) are

$$p'_{11} = p'_{22} = \frac{1}{4}(p_{11}(3+\cos(4\theta)) + (p_{12}+2p_{44})(1-\cos(4\theta))), \tag{C.3}$$

$$p'_{33} = p_{11}, \tag{C.4}$$

$$p'_{12} = p'_{21} = \frac{1}{4}(p_{12}(3+\cos(4\theta)) + (p_{11}-2p_{44})(1-\cos(4\theta))), \tag{C.5}$$

$$p'_{13} = p'_{23} = p'_{31} = p'_{32} = p_{12}, \tag{C.6}$$

$$p'_{44} = p'_{55} = p_{44}, \tag{C.7}$$

$$p'_{66} = \frac{1}{4}(2p_{44}(1+\cos(4\theta)) + (p_{11}-p_{12})(1-\cos(4\theta))), \tag{C.8}$$

$$p'_{16} = p'_{61} = \frac{1}{4}\sin(4\theta)(2p_{44}+p_{12}-p_{11}), \tag{C.9}$$

$$p'_{26} = p'_{62} = \frac{1}{4}\sin(4\theta)(p_{11}-p_{12}-2p_{44}). \tag{C.10}$$

Appendix D

Experimental Setup Details

D.1 Equipment Listing

Key	Description	Company	Model Number
–	1,520–1,570 nm tunable laser	New Focus	Velocity TLB-6328
–	optical fiber	Thorlabs	SMF-28e
–	2×2 90/10 fiber optic coupler	Thorlabs	10202A
λ-meter	wavemeter	High Finesse	WS6/200
FPC	manual fiber polarization controller	Thorlabs	FPC030
EOM	lithium niobate electro-optic amplitude modulator	EOSpace	AX-0K5-10-PFA-PFAP
VOA	variable optical attenuator	JDS Uniphase	HA9
D1	125 MHz InGaAs photodetector	New Focus	1811
–	C+L band circulator	New Focus	CIR10BN32N-P
RF-SG	microwave signal generator	Agilent	E8257D-520
LI	lock-in amplifier	SRS	SR830
SWn	2×2 fiber switch	JDSU	SN22+107D0FA
–	dual stage optical isolator	OEQuest	ISO-15-D-03
EDFA	erbium-doped fiber amplifier	Amonics	AEDFA-18
D2	broadband 12 GHz photodetector	New Focus	1554-B
RSA	real-time spectrum analyzer	Tektronix	RSA3408B
D3	nanosecond InGaAs photodetector	New Focus	1623
PM	optical power meter	Newport	1936-C

Table D.1: **Detailed equipment listing.** Full list of equipment used in the experimental setup, shown in Figure 5.1.

D.2 JDSU Switches

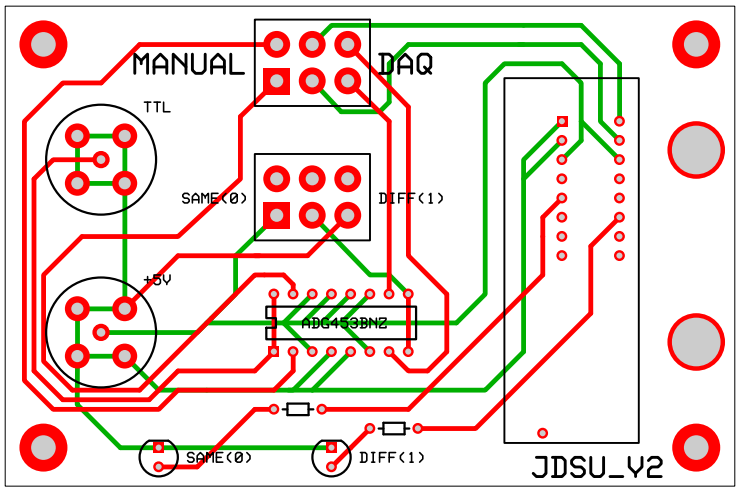

Figure D.1: **JDSU switch controller PCB schematic.** The schematic for a two layer PCB measuring 3.8 in × 2.5 in for controlling a JDSU SN Series 2 × 2 switch (model number SN22+XXXXXXX) either manually or via a TTL signal. Red indicates the top copper layer, green indicates the bottom copper layer, light gray indicates through-holes, and black indicates the top silkscreen layer. The two large holes on the right side are for securing the board to an optical table with a 1 in hole spacing. A list of components is given by Table D.2.

Qty.	Description	Manufacturer	Part Number
1	JDSU SN-SERIES 2×2 SWITCH	JDSU	SN22+XXXXXXX
1	IC SWITCH QUAD SPST 16DIP	Analog Devices Inc.	ADG453BNZ
2	SWITCH TOGGLE DPDT .4VA PC MNT	E-Switch	100AWDP1T1B4M2RE
1	LED 5MM BLUE CLEAR 470NM 30DEG	Cree Inc.	C503B-BCN-CV0Z0461
1	LED 5MM RED DIFFUSED	Lumex Inc.	SSL-LX5093ID
2	RES 1.0K OHM 1/6W 5% CARBON FILM	Yageo	CFR-12JB-1K0
4	STANDOFF M/F HEX M3 BRASS 10MM	Harwin Inc.	R30-3001002
4	NUT HEX METRIC M 3 ZINC	B&F Fastener Supply	MHNZ 003
1	IC SOCKET 16PIN MS TIN/TIN .300	Mill-Max Mfg Corp	110-44-316-41-001000
2	CONN SOCKET BNC STR 50 OHM PCB	TE Connectivity	5-1634503-1

Table D.2: **JDSU switch controller parts list.** Full list of required components for the switch controller in Figure D.1.

D.3 Electro-optic Amplitude Modulator

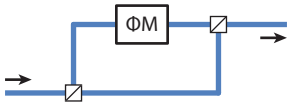

Figure D.2: **Electro-optic amplitude modulator model.** The equivalent optical circuit for an electro-optic amplitude modulator operated in the linear regime (half-max point), modeled as two ideal 50/50 beamsplitters with a phase modulator (ΦM) in one of the paths.

For an amplitude modulator biased (V_{bias}) to operate in the linear regime, modeled as Figure D.2, with a sinusoidal modulation frequency, ω, a modulation index, β, and an input field amplitude, α_{in}, the output field amplitude, α_{out}, is given by

$$\alpha_{\text{out}}(t) = \frac{\alpha_{\text{in}}(t)}{2}\left(1 + e^{i(\beta \sin \omega t \pm \pi/2)}\right), \tag{D.1}$$

where the sign of $\pm$ depends on the measured sign of $d|\alpha_{\text{out}}|^2/dV_{\text{bias}}$. For $\beta \ll 1$, this can be approximated as

$$\begin{aligned}\alpha_{\text{out}}(t) &\approx \frac{\alpha_{\text{in}}(t)}{2}\left(1 \pm i\left(1 + i\beta \sin \omega t\right)\right) \\ &= \frac{\alpha_{\text{in}}(t)}{2}\left((1 \pm i) \pm i\frac{\beta}{2}e^{i\omega t} \mp i\frac{\beta}{2}e^{-i\omega t}\right).\end{aligned} \tag{D.2}$$

D.4 Laser Frequency Stabilization

Maintaining a constant laser frequency, ω_ℓ, and cavity detuning, Δ, is a crucial part of any experiment involving optical cavities, with the fluctuations in both required to be much smaller than the optical cavity linewidth, κ. We accomplish this with a two-part locking scheme. The absolute frequency of the laser is fixed by splitting off a small amount of laser power (∼10%) to be measured by a wavemeter (WM in Figure 5.1). The measurement is read by a USB attached computer running a software locking program that outputs a control signal to the laser wavelength piezo via a National Instruments DAQ (NI PCI-6251 with BNC-2110 breakout box), resulting in stability to approximately ±5 MHz. To lock the laser wavelength to a particular detuning from the optical cavity, Δ, we have two established methods, explored below.

D.4.1 Lock-in Method

As detailed in Section 5.2, driving an electro-optic amplitude modulator (EOM in Figure 5.1) with an amplitude modulated (at ω_{LI}) RF carrier of frequency Δ_p, will yield a reflected signal from the

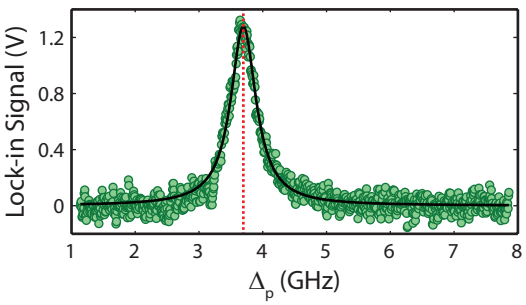

Figure D.3: **Cavity reflection signal.** The amplitude ($\sqrt{X^2+Y^2}$) of the reflected, modulated (at ω_{LI}) probe signal as a function of probe detuning, Δ_p, measured by a lock-in amplifier (LI in Figure 5.1). This is the EIT-like signal in the wide regime, as detailed in Section 5.2. The fit to (D.3) is shown in black, with the dotted red line indicating the detuning, Δ.

cavity, $R(\Delta_p)$, as measured by the lock-in amplifier, of

$$R(\Delta_p) = \frac{A}{(|\Delta| - \Delta_p)^2 + (\kappa/2)^2}, \tag{D.3}$$

where A is the proportionality constant. We can fit the signal measured by the lock-in using this model, allowing $|\Delta|$ to be determined (the sign can be determined by optical characterization of ω_o and knowledge of the laser wavelength). The lock point of the wavelength control loop can then be adjusted to achieve the desired detuning. In practice, the uncertainty in the detuning is dominated by fluctuations of the optical cavity and the resolution of the lock-in measurement. The former can be reduced by averaging the signal of multiple probe scans before fitting. The latter is set by the modulation frequency, $\omega_{\mathrm{LI}} \approx 100$ kHz for the measurements in Section 5.4, which for a 1 s frequency sweep of Δ_p between 1 GHz and 8 GHz with an integration time of 1 ms per point (∼100 lock-in cycles), limits the resolution to ∼10 MHz. For higher drive powers at room temperature, additional noise related to the thermal relaxation time of the nanobeams (on the order of kilohertz to megahertz) is present in the signal. These effects are mitigated at cryogenic temperatures and a noticeable improvement in signal quality results.

D.4.2 Network Analyzer Method

The lock-in method above, depending on the signal quality, can be quite slow, requiring ∼10 s per detuning measurement, and ∼1 minute to lock to a particular detuning (in the worst case). It also suffers from low-frequency cavity noise polluting the signal, and low signal levels since the measurement is done on reflection. Using a vector network analyzer (VNA) sensitive to Δ_p (as opposed to $\omega_{\mathrm{LI}} \ll \Delta_p$) on transmission alleviates many of these issues, and features significantly faster detuning locking (∼10 s). Figure D.4 depicts a simplified experimental setup implementing this locking scheme.

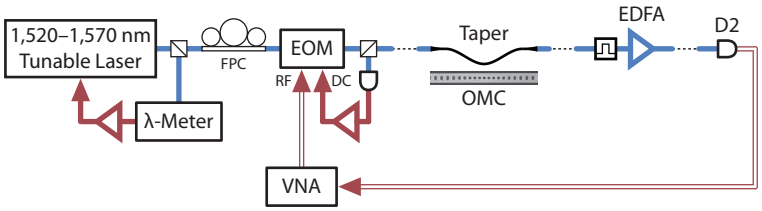

Figure D.4: **Simplified experimental setup with VNA.** The lock-in amplifier measuring a low-frequency signal on reflection is replaced by a vector network analyzer (VNA) to measure the cavity response as a function of probe detuning, Δ_p, on transmission. The EDFA is a requirement as the broadband detector, D2, has significantly lower transimpedance gain compared to D1.

In the derivation for the reflection spectra seen by the lock-in amplifier, we could neglect the more off-resonant modulator sideband since it is strongly suppressed by the cavity frequency response. However, on transmission, neither sideband is strongly suppressed. Since only one of the sidebands passes through the cavity for a given detuning (acquiring a phase and amplitude shift), unlike the reflection case, their mixing will not produce a simple Lorentzian lineshape as a function of probe detuning, Δ_p. We derive the expected signal shape here. The cavity frequency response on transmission for a detuned probe, $t_\pm(\Delta_p)$ (given by (2.39) and (2.40)), assuming $|\Delta - \omega_m| > \gamma$, is

$$t_\pm(\Delta_p) \approx 1 - \frac{\kappa_e/2}{i(\Delta \mp \Delta_p) + \kappa/2} \equiv t(\Delta_p), \tag{D.4}$$

where we choose the appropriate sign in the expression for $t(\Delta_p)$ depending on $\mathrm{sgn}(\Delta)$. Using the model for an electro-optic amplitude modulator from Section D.3, the output field amplitude from the cavity, α_{out}, is proportional to

$$\alpha_{\mathrm{out}} \propto (1 \pm i)\, t(0) \pm i\frac{\beta}{2} e^{i\Delta_p t} t(-\Delta_p) \mp i\frac{\beta}{2} e^{-i\Delta_p t} t(\Delta_p). \tag{D.5}$$

The measured signal on D2 in Figure D.4 is thus

$$\begin{aligned} |\alpha_{\mathrm{out}}|^2 &\propto |1 \pm i|^2 |t(0)|^2 + \mathcal{O}(\beta^2) \\ &\quad + \left(\mp\frac{i\beta}{2}(1 \pm i) t^*(-\Delta_p) t(0) \mp \frac{i\beta}{2}(1 \mp i) t(\Delta_p) t^*(0) \right) e^{-i\Delta_p t} \\ &\quad + \left(\pm\frac{i\beta}{2}(1 \mp i) t(-\Delta_p) t^*(0) \pm \frac{i\beta}{2}(1 \pm i) t^*(\Delta_p) t(0) \right) e^{i\Delta_p t} \\ &= |1 \pm i|^2 |t(0)|^2 + 2|A| \cos(\Delta_p t - \arg\{A\}), \end{aligned} \tag{D.6}$$

where

$$A'(\Delta_p, \Delta, \beta) = \mp\frac{i\beta}{2}(1 \pm i) t^*(-\Delta_p) t(0) \mp \frac{i\beta}{2}(1 \mp i) t(\Delta_p) t^*(0), \tag{D.7}$$

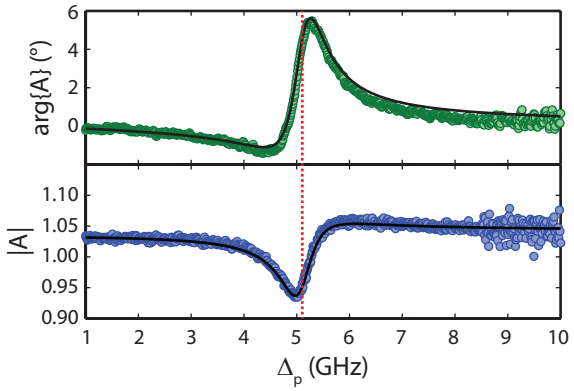

Figure D.5: **Example VNA signal.** Normalized phase (green ○) and amplitude (blue ○) quadratures as measured by the VNA for $\Delta > 0$ (so $t(\Delta_p) = t_+(\Delta_p)$). The phase quadrature is fit using (D.9) and the same set of fit parameters is used to plot the theoretical $|A|$, showing good correspondence to the measured data. The fitted detuning is given as the dotted red line, and we note that it does not coincide with either peak.

and the VNA signal for the phase and amplitude quadrature are modeled by $\arg\{A'\}$ and $|A'|$ respectively.

In practice, we noticed deviation of the measured signal from the derived model, which was attributed to an imbalance in the beamsplitter arms and a phase difference in the probe sidebands. To correct for this, we phenomenologically insert two fitting constants, α and θ, so that we have instead

$$A'(\Delta_p, \Delta, \beta) \to A'(\Delta_p, \Delta, \beta, \alpha, \theta) = \mp\frac{i\beta}{2}(\alpha \pm e^{i\theta})t^*(-\Delta_p)t(0) \mp \frac{i\beta}{2}(\alpha \mp e^{i\theta})t(\Delta_p)t^*(0). \tag{D.8}$$

A far detuned scan of Δ_p allows A' to be normalized by $A'(\Delta_p, \infty, \beta, \alpha, \theta)$ yielding the normalized expression

$$\begin{aligned} A(\Delta_p, \Delta, \alpha, \theta) &= \frac{A'(\Delta_p, \Delta, \beta, \alpha, \theta)}{A'(\Delta_p, \infty, \beta, \alpha, \theta)} \\ &= \frac{(\alpha \pm e^{i\theta})t^*(-\Delta_p)t(0) + (\alpha \mp e^{i\theta})t(\Delta_p)t^*(0)}{(\alpha \pm e^{i\theta}) + (\alpha \mp e^{i\theta})}, \end{aligned} \tag{D.9}$$

which crucially no longer depends on β, and $\arg\{A\}$ exactly models the normalized phase signal from the VNA (without a proportionality constant).

An example of this detuning fitting is given by Figure D.5 where we have fit the measured phase quadrature using $\arg\{A\}$ (having independently measured κ and κ_e, and normalized the signal with a far detuned scan of Δ_p) and plotted $|A|$ against the measured amplitude quadrature (without adjusting any fitting parameters).

D.5 Continuous Flow Liquid Helium Cryostat

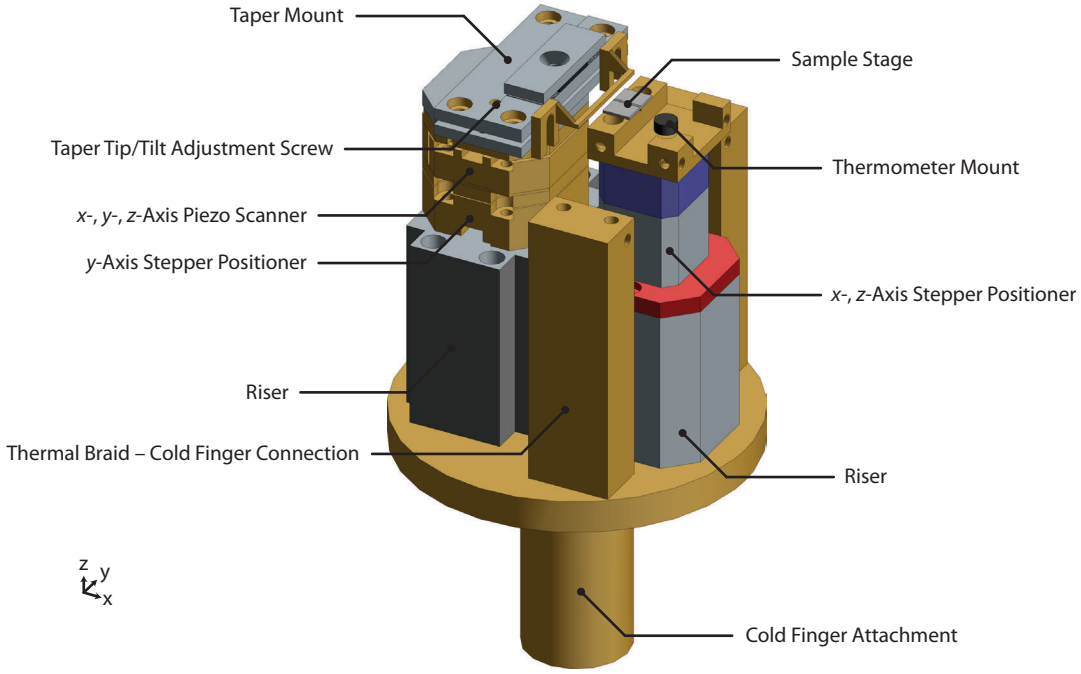

Figure D.6: **Schematic of cryostat stage stack.** Schematic of the stage stack mounted on the ST-500 cryostat cold finger. The cold finger connection and base plate are gold plated copper and nearly all other components are copper with the exception of the taper mount being aluminum and the stages being titanium. Credit for the technical drawing goes to Alex Krause and Ryan Camacho.

For this work, we use an ST-500 Microscopy Cryostat from Janis Research Company in conjunction with a stage stack (schematically shown in Figure D.6) and vacuum can with radiation shield (Figure D.7), capable of achieving ∼4 K at the cold finger and ∼6 K at the sample stage. However, mechanical mode thermometry indicates that the sample itself only cools to ∼18 K (at the time of the main result in Section 5.4), likely due to poor thermalization and blackbody radiation entering through the viewing port of the vacuum can.

The stepper positioners are made by Attocube (model ANPx101). They are used for sub-nanometer positioning of the taper in the $\hat{y}$ direction, and of the sample stage in the $\hat{x}$ and $\hat{z}$ direction, with a ∼5 mm range. All three axes are controlled with an Attocube ANC 150 piezo step controller. For fine positioning of the fiber taper probe, we use an Attocube ANSxyz100 piezo scanner, capable of nearly continuous fine positioning over ∼20 µm in all three directions at cryogenic temperatures.

Significant improvement to the final sample temperature (to ∼10 K) was achieved by replacing the originally aluminum risers with copper ones, attaching copper thermal braids to the sample mount, adding a copper clip to the sample mount to apply direct pressure to the sample, taping

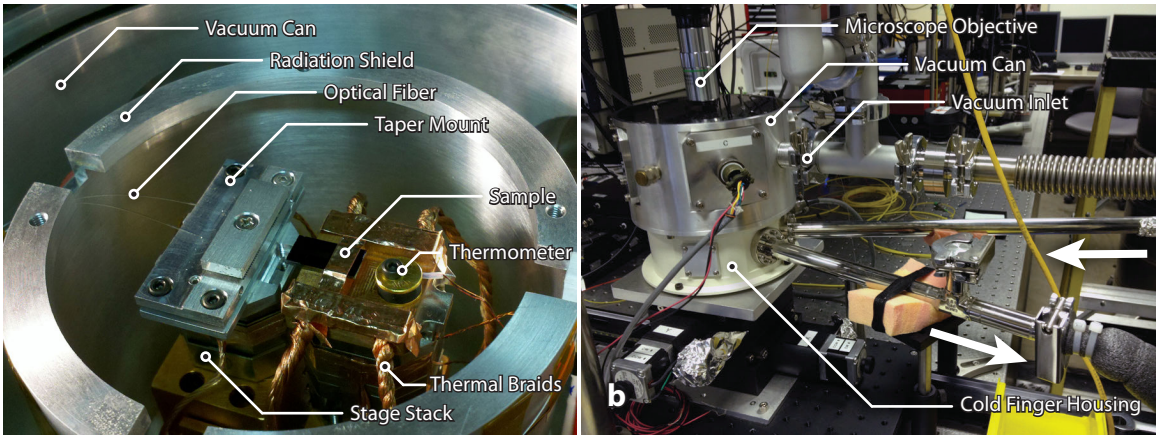

Figure D.7: **Cryostat pictures. a**, An overhead view of the cryostat setup, showing the positioning of the stage stack from Figure D.6 in relation to the radiation shield and exterior vacuum can. From this view, the copper thermal braids connecting the sample mount to the cold finger through copper blocks can be seen. In the image, the sample is secured to the copper stage using copper tape, but we have since added a copper sample clip for better thermalization. **b**, The entire cryostat setup showing the vacuum can sitting on top of the cold finger housing, with helium flow directions indicated with the white arrows. Above the cryostat, we have a microscope objective to position the fiber taper for coupling.

both the optical fiber (leading to the dimpled taper) and the stage wires to the outside of the radiation shield using copper tape (keeping them far from the inside of the vacuum can), reducing the size of the microscopy hole in the radiation shield, and covering the hole with a 1/8" thick, 1–3/4" diameter IR filter (from ESCO products).

D.6 Dimpled Fiber Taper

The dimpled fiber taper has greatly expedited the fabrication–characterization cycle of device design by providing an efficient (capable of near unity transmission contrast when coupling to an optical mode), nearly lossless (<0.05 dB end-to-end loss possible), and flexible (controllable transmission contrast between near vanishing and near unity through careful positioning via nanopositioners) method of coupling to an optical microcavity. An additional, significant advantage is that the scheme imposes no additional complications on the fabrication procedure. A microscope image of a 5G device coupled to the laser drive via a dimpled fiber taper is shown in Figure D.8.

D.7 Instrument Control

We note that much of the instrument control was done via MATLAB and the Instrument Control Toolbox [151]. The wavemeter feedback software was written by myself in .NET (C#) with libraries from National Instruments to interface with the General Purpose Interface Bus (GPIB) network.

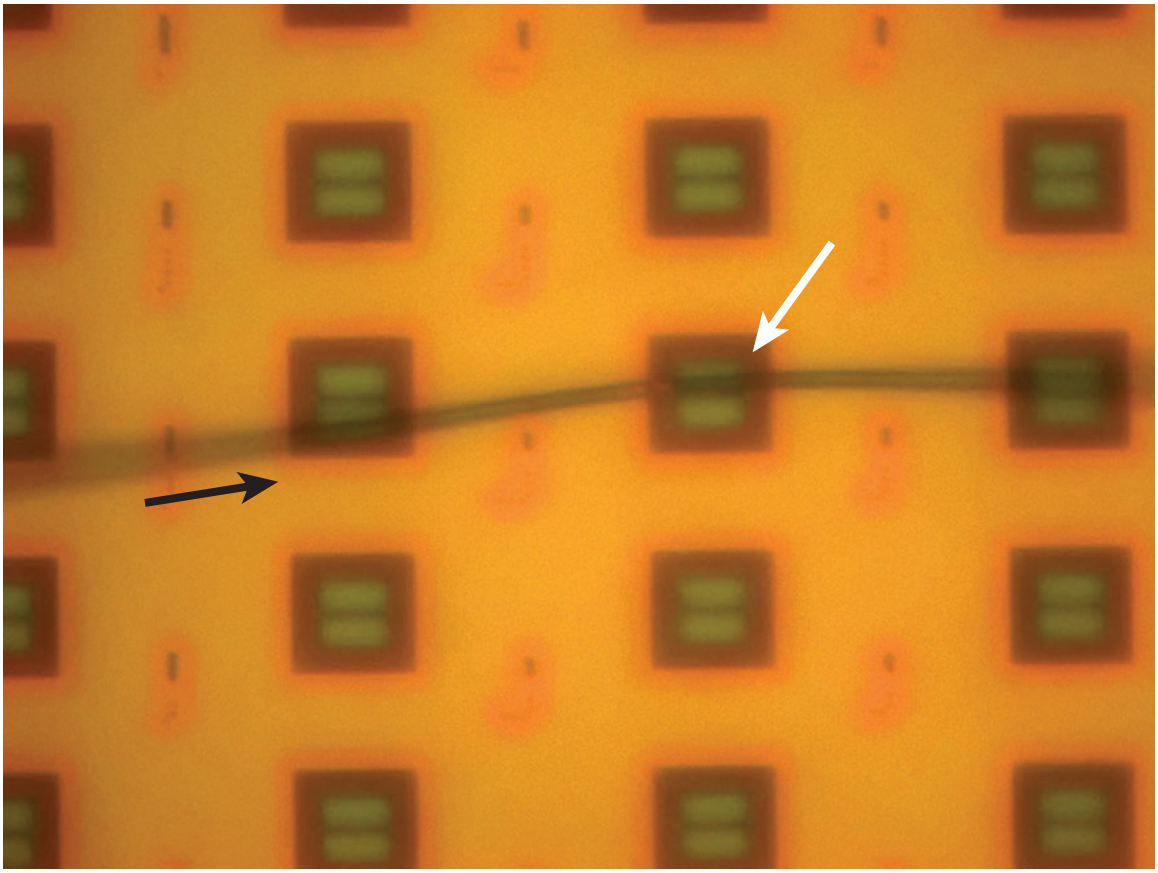

Figure D.8: **Taper coupling in the cryostat.** We see here a dimpled fiber taper (with laser propagation direction indicated with a black arrow) couple evanescently to a 5G device (indicated with a white arrow). The taper is positioned using a combination of nanosteppers and nanoscanners (described in Section D.5). We note from this image that the region of the taper that is touching the silicon is to the left of the device (discolored region in the dimple) and that the taper is at a slight angle to compared to the nanobeams. This is intentional. The asymmetric touch minimizes the optical loss to the light leaving the cavity, which conversely maximizes the measured signal-to-noise ratio. The relative tilt allows for better control of the taper coupling. In practice, if the nanobeam and taper are too parallel, the taper tends to be drawn into the nanobeam, resulting in significant degradation to both optical and mechanical quality factors. The way we have touched in the figure allows part of the taper to be firmly planted to the side of the nanobeam (in the phononic shield region), while maintaining a sufficient distance from the optical cavity (the taper starts curving upwards as we move passed the discolored part to the right) so not to perturb the optical field adversely.

Appendix E

Silicon Material Properties

T [K]	n	T [K]	n	T [K]	n
5	–	100	3.45579	210	3.46876
10	–	110	3.45661	220	3.47025
15	–	120	3.45754	230	3.47178
20	–	130	3.45858	240	3.47338
30	3.45289	140	3.45969	250	3.47503
40	3.45302	150	3.46087	260	3.47675
50	3.45322	160	3.46208	270	3.47851
60	3.45353	170	3.46332	280	3.48030
70	3.45396	180	3.46461	290	3.48212
80	3.45449	190	3.46595	300	3.48394
90	3.45510	200	3.46733	310	3.48575

Table E.1: **Temperature-dependent refractive index.** Normalized data for $\lambda = 1{,}500$ nm from [119]. Data for $T < 30$ K could not be found.

T [K]	$\frac{dn}{dT}$ [K^{-1}]	T [K]	$\frac{dn}{dT}$ [K^{-1}]	T [K]	$\frac{dn}{dT}$ [K^{-1}]
5	–	100	7.773×10^{-5}	210	1.465×10^{-4}
10	–	110	8.743×10^{-5}	220	1.513×10^{-4}
15	–	120	9.650×10^{-5}	230	1.561×10^{-4}
20	–	130	1.048×10^{-4}	240	1.611×10^{-4}
30	5.853×10^{-6}	140	1.124×10^{-4}	250	1.660×10^{-4}
40	1.611×10^{-5}	150	1.189×10^{-4}	260	1.708×10^{-4}
50	2.640×10^{-5}	160	1.245×10^{-4}	270	1.755×10^{-4}
60	3.670×10^{-5}	170	1.294×10^{-4}	280	1.801×10^{-4}
70	4.698×10^{-5}	180	1.337×10^{-4}	290	1.847×10^{-4}
80	5.725×10^{-5}	190	1.379×10^{-4}	300	1.893×10^{-4}
90	6.756×10^{-5}	200	1.421×10^{-4}	310	1.939×10^{-4}

Table E.2: **Temperature-dependent thermo-optic coefficient.** Normalized data for $\lambda = 1{,}500$ nm from [119]. Data for $T < 30$ K could not be found.

T [K]	γ	T [K]	γ	T [K]	γ
5	0.3291	100	0.1862	210	0.3714
10	0.2833	110	0.2077	220	0.3831
15	0.2524	120	0.2291	230	0.3943
20	0.2276	130	0.2502	240	0.4047
30	0.1860	140	0.2700	250	0.4137
40	0.1566	150	0.2882	260	0.4232
50	0.1386	160	0.3028	270	0.4334
60	0.1288	170	0.3171	280	0.4428
70	0.1296	180	0.3319	290	0.4491
80	0.1422	190	0.3457	300	0.4556
90	0.1626	200	0.3590	310	0.4643

Table E.3: **Temperature-dependent Grüneisen coefficient.** Normalized data from [98], calculated using TOEC and SOEC.

T [K]	$\alpha \left[\frac{10^{-6}}{\mathrm{K}}\right]$	T [K]	$\alpha \left[\frac{10^{-6}}{\mathrm{K}}\right]$	T [K]	$\alpha \left[\frac{10^{-6}}{\mathrm{K}}\right]$
5	0.0000675	100	−0.3390	210	1.565
10	0.000480	110	−0.2122	220	1.715
15	0.001220	120	−0.0570	230	1.855
20	−0.00290	130	0.1186	240	1.986
30	−0.05290	140	0.3060	250	2.108
40	−0.1640	150	0.4975	260	2.223
50	−0.2930	160	0.6890	270	2.331
60	−0.4000	170	0.8775	280	2.432
70	−0.4620	180	1.0610	290	2.526
80	−0.4720	190	1.2376	300	2.618
90	−0.4290	200	1.4060	310	2.702

Table E.4: **Temperature-dependent thermal expansivity.** Normalized data from [152].

T [K]	$\kappa \left[\frac{\mathrm{W}}{\mathrm{m}\cdot\mathrm{K}}\right]$	T [K]	$\kappa \left[\frac{\mathrm{W}}{\mathrm{m}\cdot\mathrm{K}}\right]$	T [K]	$\kappa \left[\frac{\mathrm{W}}{\mathrm{m}\cdot\mathrm{K}}\right]$
5	420	100	925	210	234
10	1524	110	757	220	217
15	2498	120	638	230	203
20	3188	130	553	240	193
30	3571	140	490	250	184
40	3240	150	436	260	177
50	2696	160	388	270	172
60	2163	170	347	280	167
70	1770	180	311	290	161
80	1446	190	280	300	155
90	1155	200	255	310	148

Table E.5: **Temperature-dependent thermal conductivity.** Normalized data from [153].

T [K]	c_s [m/s]	T [K]	c_s [m/s]	T [K]	c_s [m/s]
5	–	100	9171.0	210	9151.8
10	–	110	9170.1	220	9149.4
15	–	120	9169.0	230	9146.9
20	–	130	9167.6	240	9144.4
30	–	140	9166.0	250	9142.1
40	–	150	9164.4	260	9139.9
50	–	160	9162.6	270	9137.5
60	–	170	9160.6	280	9135.0
70	–	180	9158.4	290	9132.5
80	9172.8	190	9156.2	300	9129.9
90	9171.9	200	9154.0	310	–

Table E.6: **Temperature-dependent speed of sound.** Normalized data for [110] longitudinal waves in silicon from [154].

T [K]	C_V $\left[\frac{10^6 \cdot \mathrm{J}}{\mathrm{kg} \cdot \mathrm{K}}\right]$	T [K]	C_V $\left[\frac{10^6 \cdot \mathrm{J}}{\mathrm{kg} \cdot \mathrm{K}}\right]$	T [K]	C_V $\left[\frac{10^6 \cdot \mathrm{J}}{\mathrm{kg} \cdot \mathrm{K}}\right]$
5	–	100	0.4739	210	1.3461
10	–	110	0.5733	220	1.3945
15	–	120	0.6722	230	1.4387
20	–	130	0.7686	240	1.4790
30	–	140	0.8609	250	1.5159
40	–	150	0.9477	260	1.5497
50	–	160	1.0287	270	1.5806
60	–	170	1.1035	280	1.6090
70	–	180	1.1723	290	1.6356
80	0.2778	190	1.2355	300	1.6611
90	0.3755	200	1.2933	310	1.6866

Table E.7: **Heat capacity between 80 K and 300 K.** Normalized data from [154].

T [K]	C_V $\left[\frac{\mathrm{J}}{\mathrm{mol} \cdot \mathrm{K}}\right]$	T [K]	C_V $\left[\frac{\mathrm{J}}{\mathrm{mol} \cdot \mathrm{K}}\right]$	T [K]	C_V $\left[\frac{\mathrm{J}}{\mathrm{mol} \cdot \mathrm{K}}\right]$
5	–	100	7.0908	210	–
10	–	110	–	220	–
15	0.0310	120	–	230	–
20	0.1020	130	–	240	–
30	0.5100	140	–	250	–
40	1.3000	150	–	260	–
50	2.3000	160	–	270	–
60	3.4900	170	–	280	–
70	4.6600	180	–	290	–
80	5.6600	190	–	300	–
90	6.4400	200	–	310	–

Table E.8: **Atomic heat capacity between 15 K and 100 K.** Normalized data from [155].

Appendix F

COMSOL 3.5a Functions

COMSOL Multiphysics 3.5a is a powerful finite element method simulation tool used to do many of the optical and mechanical simulations presented above. While the native function set is quite extensive, numerous helper functions have been written to augment its functionality. The most important and often used ones are listed here.

F.1 Geometry Indices

COMSOL does not provide a simple function for accessing geometry indices by their coordinates. When scripting simulations, it is immensely helpful to be able to do so.

```
function bnd = bndindex(g,p0,varargin)
% bnd = bndindex(g,p0,n)
% bnd = bndindex(g,p0,p1,p2)
% Returns the indices of the faces that are coplanar with the specified plane.
% Planes are specified by (p0,n) or (p0,p1,p2) where px are points in the plane and n is a
    normal vector to the plane. p0 is the reference point.
n = [];
tol = 1e-10;
if(length(varargin)==1)
    n = varargin{1};
else
    n = cross(varargin{1}-p0,varargin{2}-p0);
end
if(dot(n,n)==0)
    error('Normal not specified correctly.');
end
p = cell2mat(geominfo(g,'out','xx','par',num2cell(num2cell([1:geominfo(g,'out','no','0d',0)]))))
    ;
vx = p(:,:,1)-p0(1);
vy = p(:,:,2)-p0(2);
vz = p(:,:,3)-p0(3);
inplane = find(abs(vx*n(1)+vy*n(2)+vz*n(3))<max(abs(vx*n(1)+vy*n(2)+vz*n(3)))*tol);
adj = geominfo(g,'out','adj','0dp',[2;0]);
bnd = find(sum(adj{1}(:,inplane),2)==sum(adj{1},2))';
```

```
function vtx = boxindex(g,dim,dx,dy,dz,varargin)
```

```
% vtx = boxindex(g,dim,dx,dy,dz,[options])
% pos: 3x1 vector (default [0 0 0]), specifying the anchor point of the bounding box
% base: ('center','corner') (default 'center'), specifying where the anchor point is relative to the bounding box
% Returns the indices the geometry elements of dimension dim inside a bounding box of size (dx,dy,dz), anchored at pos.

S.pos = [0 0 0];
S.base = 'center';
for k=1:2:length(varargin); if (isfield(S,lower(varargin{k}))); S.(lower(varargin{k})) = varargin{k+1}; end; end;
if(strcmp(S.base,'corner')); S.pos = S.pos+[dx,dy,dz]/2; end;

p = cell2mat(geominfo(g,'out','xx','par',num2cell(num2cell([1:geominfo(g,'out','no','Od',0)]))));
vx = p(:,:,1);
vy = p(:,:,2);
vz = p(:,:,3);
inbox = find(abs(vx-S.pos(1))<=dx/2+1e-12&abs(vy-S.pos(2))<=dy/2+1e-12&abs(vz-S.pos(3))<=dz/2+1e-12);
adj = geominfo(g,'out','adj','Odp',[dim;0]);
vtx = find(abs(sum(adj{1}(:,inbox),2))==abs(sum(adj{1},2)))';

% sometimes comsol inserts the complete geometry as the first element
if(dim==3)
    vtx(vtx==1) = [];
    vtx = vtx-1;
end
```

```
function vtx = vtxindex(g,bndindex)
% vtx = vtxindex(g,bndindex)
% Returns the indices of the vertices that outline the boundary element with index bndindex

adj = geominfo(g,'out','adj','Odp',[2;0]);
vtx = find(adj{1}(bndindex,:));
```

```
function bnd = bndexterior(g)
% bnd = bndexterior(g)
% Returns the indices of the exterior boundaries.

adj = geominfo(g,'out','adj','odp',[3;2]);
adj = adj{1};
bnds = {};
for k=2:size(adj,1)
    bnds{k-1} = find(adj(k,:)~=0);
end
commonbnds = [];
for k=1:length(bnds)
    for m=setdiff(1:length(bnds),k)
        commonbnds = [ commonbnds intersect(bnds{k},bnds{m}) ];
    end
end
commonbnds = unique(commonbnds);

bnd = 1:flgeomnbs(g);
bnd(commonbnds) = [];
```

F.2 Perturbation Theory

To compute the optomechanical coupling rate of an optical and mechanical mode, it is necessary to generate two solution objects (one for each). One-to-one mapping of the solutions on to each other is often not possible because of the disparate meshing (optical simulations require an air box while mechanical simulations do not), so helper functions were written to perform this projection. Often we want to find the coupling rate of many mechanical modes to a single optical mode so some speedup can be obtained by caching the optical solution. We include the example function `measure_g` to demonstrate this.

```
function a = oint_bnd_prep(xx,yy,zz,n)
global GLOBAL_ofem;
global GLOBAL_ebnd GLOBAL_ebnd_c;

nn = find(abs(xx)<3e-6&abs(yy)<2e-6);
a = zeros(size(xx));

if(~isempty(nn)); a(nn) = postinterp(GLOBAL_ofem,['(' num2str(str2double(n)^2-1) '*epsilon0_rfw*
    normtE_rfw^2-' num2str(1/str2double(n)^2-1) '/epsilon0_rfw*(abs(nx*Dx_rfw)^2+abs(ny*Dy_rfw)
    ^2+abs(nz*Dz_rfw)^2))'],[xx(nn);yy(nn);zz(nn)],'edim',2); end;
a(isnan(a)) = 0;
GLOBAL_ebnd{GLOBAL_ebnd_c} = a;
GLOBAL_ebnd_c = GLOBAL_ebnd_c+1;
```

```
function a = oint_sub_prep(xx,yy,zz)
global GLOBAL_ofem;
global GLOBAL_ex GLOBAL_ey GLOBAL_ez GLOBAL_exy GLOBAL_exz GLOBAL_eyz;
global GLOBAL_ex_c GLOBAL_ey_c GLOBAL_ez_c GLOBAL_exy_c GLOBAL_exz_c GLOBAL_eyz_c;

nn = find(abs(xx)<3e-6&abs(yy)<2e-6);
a = zeros(size(xx));

if(~isempty(nn)); a(nn) = postinterp(GLOBAL_ofem,'epsilon0_rfw*abs(Ex)^2',[xx(nn);yy(nn);zz(nn)
    ],'edim',3); end;
a(isnan(a)) = 0;
GLOBAL_ex{GLOBAL_ex_c} = a;
GLOBAL_ex_c = GLOBAL_ex_c+1;

if(~isempty(nn)); a(nn) = postinterp(GLOBAL_ofem,'epsilon0_rfw*abs(Ey)^2',[xx(nn);yy(nn);zz(nn)
    ],'edim',3); end;
a(isnan(a)) = 0;
GLOBAL_ey{GLOBAL_ey_c} = a;
GLOBAL_ey_c = GLOBAL_ey_c+1;

if(~isempty(nn)); a(nn) = postinterp(GLOBAL_ofem,'epsilon0_rfw*abs(Ez)^2',[xx(nn);yy(nn);zz(nn)
    ],'edim',3); end;
a(isnan(a)) = 0;
GLOBAL_ez{GLOBAL_ez_c} = a;
GLOBAL_ez_c = GLOBAL_ez_c+1;

if(~isempty(nn)); a(nn) = postinterp(GLOBAL_ofem,'2*epsilon0_rfw*real(Ex*conj(Ey))',[xx(nn);yy(
    nn);zz(nn)],'edim',3); end;
a(isnan(a)) = 0;
GLOBAL_exy{GLOBAL_exy_c} = a;
```

```
GLOBAL_exy_c = GLOBAL_exy_c+1;

if(~isempty(nn)); a(nn) = postinterp(GLOBAL_ofem,'2*epsilon0_rfw*real(Ex*conj(Ez))',[xx(nn);yy(nn);zz(nn)],'edim',3); end;
a(isnan(a)) = 0;
GLOBAL_exz{GLOBAL_exz_c} = a;
GLOBAL_exz_c = GLOBAL_exz_c+1;

if(~isempty(nn)); a(nn) = postinterp(GLOBAL_ofem,'2*epsilon0_rfw*real(Ey*conj(Ez))',[xx(nn);yy(nn);zz(nn)],'edim',3); end;
a(isnan(a)) = 0;
GLOBAL_eyz{GLOBAL_eyz_c} = a;
GLOBAL_eyz_c = GLOBAL_eyz_c+1;
```

```
function a = oint_run(~,~,~,id)
cid = [id '_c'];
eval(sprintf('global %s;',id));
eval(sprintf('global %s;',cid));
a = eval(sprintf('%s{%s};',id,cid));
eval(sprintf('%s = %s+1;',cid,cid));
```

```
function [ g S ] = measure_g(ofem,mfem,ind)
% [ g S ] = measure_g(ofem,mfem,ind)
% Computes the optomechanical coupling rate between an RF Module/Electromagnetic Waves solution object and a Strutural Mechanics Module/Solid, Stress-Strain solution object.
% It is assumed there is only one optical mode in ofem, while the mechanical modes in mfem can be chosen with the vector variable ind.
% Returns the computed optomechanical coupling rate g, and an object S containing a breakdown of the individual contributions in the first order perturbation theory for moving boundaries and photoelastic effect.

% constants
p11 = -0.101;
p12 = 0.0094;
p44 = -0.051;
c = 299792458;
hbar = 1.05457148e-34;

% globals
global GLOBAL_ofem;
global GLOBAL_ebnd GLOBAL_ebnd_c;
global GLOBAL_ex GLOBAL_ey GLOBAL_ez GLOBAL_exy GLOBAL_exz GLOBAL_eyz;
global GLOBAL_ex_c GLOBAL_ey_c GLOBAL_ez_c GLOBAL_exy_c GLOBAL_exz_c GLOBAL_eyz_c;
GLOBAL_ofem = ofem;

% fem constants
rho = sscanf(mfem.lib.mat{sscanf(mfem.appl{1}.equ.rho,'mat%i')}.variables.rho,'%f[kg/m^3]')*10^15;
n = ofem.appl{1}.equ.n{end};

% prepare ofem integrals
GLOBAL_ebnd = {};
[GLOBAL_ex GLOBAL_ey GLOBAL_ez GLOBAL_exy GLOBAL_exz GLOBAL_eyz] = deal({},{},{},{},{},{});
GLOBAL_ebnd_c = 1;
[GLOBAL_ex_c GLOBAL_ey_c GLOBAL_ez_c GLOBAL_exy_c GLOBAL_exz_c GLOBAL_eyz_c] = deal(1,1,1,1,1,1);
display('prepping bnd integral...');
postint(mfem,['oint_bnd_prep(x,y,z,''' num2str(n) ''')'],'edim',2);
```

```
display('prepping sub integral...');
postint(mfem,'oint_sub_prep(x,y,z)','edim',3);

% running integrals
Ibnd = [];
Ip11 = [];
Ip12 = [];
Ip44 = [];
for N = ind;
    display(['processing solution #' num2str(N) '...']);
    GLOBAL_ebnd_c = 1;
    [GLOBAL_ex_c GLOBAL_ey_c GLOBAL_ez_c GLOBAL_exy_c GLOBAL_exz_c GLOBAL_eyz_c] = deal
        (1,1,1,1,1,1);
    Ibnd(end+1) = postint(mfem,'(u*nx+v*ny+w*nz)*oint_run(x,y,z,''GLOBAL_ebnd'')','edim',2,'
        solnum',N);
    Ip11(end+1) = postint(mfem,'ex_smsld*oint_run(x,y,z,''GLOBAL_ex'')+ey_smsld*oint_run(x,y,z,'
        'GLOBAL_ey'')+ez_smsld*oint_run(x,y,z,''GLOBAL_ez'')','edim',3,'solnum',N);
    Ip44(end+1) = postint(mfem,'exy_smsld*oint_run(x,y,z,''GLOBAL_exy'')+exz_smsld*oint_run(x,y,
        z,''GLOBAL_exz'')+eyz_smsld*oint_run(x,y,z,''GLOBAL_eyz'')','edim',3,'solnum',N);
end
for N = ind;
    display(['processing solution #' num2str(N) '...']);
    [GLOBAL_ex_c GLOBAL_ey_c GLOBAL_ez_c GLOBAL_exy_c GLOBAL_exz_c GLOBAL_eyz_c] = deal
        (1,1,1,1,1,1);
    Ip12(end+1) = postint(mfem,'(ey_smsld+ez_smsld)*oint_run(x,y,z,''GLOBAL_ex'')+(ex_smsld+
        ez_smsld)*oint_run(x,y,z,''GLOBAL_ey'')+(ex_smsld+ey_smsld)*oint_run(x,y,z,''GLOBAL_ez''
        )','edim',3,'solnum',N);
end
Iesq = postint(ofem,'normE_rfw^2*epsilon_rfw');

% measure omega_m
display('finding omega_m...');
omega_m = mfem.sol.lambda(ind)*1i;

% measure d_max
display('finding max displacement...')
d_max = [];
for N = ind
    d_max(end+1) = postmax(mfem,'abs(disp_smsld)','solnum',N,'edim',2);
end

% measure m_eff (assuming x, y, and z symmetry planes are present and the simulation volume is
    1/8th of the true volume)
display('finding m_eff...');
dsq_int = postint(mfem,'abs(disp_smsld)^2','solnum',ind);
m_eff = 8*rho*dsq_int./d_max.^2; % mass in pg

% measure f_o
f_o = abs(imag(ofem.sol.lambda))/2/pi;

% compute x_zpf
x_zpf = sqrt(hbar./(2.*m_eff.*1e-12.*1e-3.*omega_m));

% compute g
g_bnd = -x_zpf.*f_o.*(Ibnd./Iesq./d_max./2);
g_str = -x_zpf.*f_o.*(-n^4.*(p11*Ip11+p12*Ip12+p44*Ip44)./Iesq./d_max./2);
g = g_bnd + g_str;

```

```
% store variables
S.g_bnd = g_bnd;
S.g_str = g_str;
S.g = g;
S.x_zpf = x_zpf;
S.f_o = f_o;
S.f_m = omega_m/2/pi;
S.m_eff = m_eff;
S.Ip11 = Ip11;
S.Ip12 = Ip12;
S.Ip44 = Ip44;
```

F.3 Miscellaneous

```
function fem = extractsolution(fem,n)
% fem = extractsolution(fem,n)
% To save disk space and loading efficiency, we extract the solution we care about (indexed by n
    ) into a new fem solution structure.

fem.sol = asseminit(fem,'init',fem.sol,'solnum',n,'blocksize','auto')
```

Appendix G

Publications

A. H. Safavi-Naeini, J. Chan, J. T. Hill, T. P. M. Alegre, A. Krause, and O. Painter, "Observation of quantum motion of a nanomechanical resonator," *Phys. Rev. Lett.* **108**, 033602– (2012).

J. Chan, T. P. M. Alegre, A. H. Safavi-Naeini, J. T. Hill, A. Krause, S. Gröblacher, M. Aspelmeyer, and O. Painter, "Laser cooling of a nanomechanical oscillator into its quantum ground state," *Nature* **478**, 89–92 (2011).

A. H. Safavi-Naeini, T. P. M. Alegre, J. Chan, M. Eichenfield, M. Winger, Q. Lin, J. T. Hill, D. Chang, and O. Painter, "Electromagnetically induced transparency and slow light with optomechanics," *Nature* **472**, 69–73 (2011).

M. Eichenfield, J. Chan, R. M. Camacho, K. J. Vahala, and O. Painter, "Optomechanical crystals," *Nature* **462**, 78–82 (2009).

M. Eichenfield, J. Chan, A. H. Safavi-Naeini, K. J. Vahala, and O. Painter, "Modeling dispersive coupling and losses of localized optical and mechanical modes in optomechanical crystals," *Opt. Express* **17**, 20078–20098 (2009).

R. M. Camacho, J. Chan, M. Eichenfield, and O. Painter, "Characterization of radiation pressure and thermal effects in a nanoscale optomechanical cavity," *Opt. Express* **17**, 15726–15735 (2009).

M. Eichenfield, R. Camacho, J. Chan, K. J. Vahala, and O. Painter, "A picogram- and nanometre-scale photonic-crystal optomechanical cavity," *Nature* **459**, 550–555 (2009).

J. Chan, M. Eichenfield, R. Camacho, and O. Painter, "Optical and mechanical design of a "zipper" photonic crystal optomechanical cavity," *Opt. Express* **17**, 3802–3817 (2009).

Bibliography

[1] J. Kepler, *De Cometis Libelli Tres* (Augsburg, 1619).

[2] C. Hakfoort, *Optics in the Age of Euler: Conceptions of the Nature of Light, 1700–1795* (Cambridge University Press, 1995), revised edition.

[3] J. C. Maxwell, *A Treatise on Electricity and Magnetism*, Vol. 2 (Clarendon Press, Oxford, 1873).

[4] O. Reynolds, "On certain dimensional properties of matter in the gaseous state. Part I. Experimental researches on thermal transpiration of gases through porous plates and on the laws of transpiration and impulsion, including an experimental proof that gas is not a continuous plenum. Part II. On an extension of the dynamical theory of gas, which includes the stresses, tangential and normal, caused by a varying condition of gas, and affords an explanation of the phenomena of transpiration and impulsion," *Royal Society of London Philosophical Transactions Series I* **170**, 727–845 (1879).

[5] J. C. Maxwell, "On stresses in rarified gases arising from inequalities of temperature," *Philosophical Transactions of the Royal Society of London* **170**, 231–256 (1879).

[6] P. Lebedev, "Untersuchungen über die Druckkräfte des Lichtes," *Ann. Phys.* **6**, 433–458 (1901).

[7] E. F. Nichols and G. F. Hull, "About radiation pressure," *Ann. Phys.* **12**, 225–263 (1903).

[8] E. F. Nichols and G. F. Hull, "The pressure due to radiation," *Proc. Am. Acad. Arts Sci.* **38**, 559–599 (1903).

[9] M. Saha, "On radiation-pressure and the quantum theory," *Astrophysical Journal* **50**, 220 (1919).

[10] A. H. Compton, "A quantum theory of the scattering of x-rays by light elements," *Phys. Rev.* **21**, 483–502 (1923).

[11] V. B. Braginsky and Y. I. Vorontsov, "Quantum-mechanical limitations in macroscopic experiments and modern experimental technique," *Sov. Phys. Usp.* **17**, 644–650 (1975).

[12] V. Braginsky and A. Manukin, *Measurement of Weak Forces in Physics Experiments* (University of Chicago Press, 1977).

[13] C. Caves, K. Thorne, R. Drever, V. D. Sandberg, and M. Zimmermann, "On the measurement of a weak classical force coupled to a quantum-mechanical oscillator," *Reviews of Modern Physics* **52**, 341–392 (1980).

[14] C. M. Caves, "Quantum-mechanical radiation-pressure fluctuations in an interferometer," *Phys. Rev. Lett.* **45**, 75–79 (1980).

[15] C. Fabre, M. Pinard, S. Bourzeix, A. Heidmann, E. Giacobino, and S. Reynaud, "Quantum-noise reduction using a cavity with a movable mirror," *Phys. Rev. A* **49**, 1337–1343 (1994).

[16] S. Mancini and P. Tombesi, "Quantum noise reduction by radiation pressure," *Phys. Rev. A* **49**, 4055–4065 (1994).

[17] G. J. Milburn, K. Jacobs, and D. F. Walls, "Quantum-limited measurements with the atomic force microscope," *Phys. Rev. A* **50**, 5256–5263 (1994).

[18] M. Pinard, C. Fabre, and A. Heidmann, "Quantum-nondemolition measurement of light by a piezoelectric crystal," *Phys. Rev. A* **51**, 2443–2449 (1995).

[19] S. Bose, K. Jacobs, and P. L. Knight, "Preparation of nonclassical states in cavities with a moving mirror," *Phys. Rev. A* **56**, 4175–4186 (1997).

[20] S. Mancini, D. Vitali, and P. Tombesi, "Optomechanical cooling of a macroscopic oscillator by homodyne feedback," *Phys. Rev. Lett.* **80**, 688–691 (1998).

[21] F. Diedrich, J. C. Bergquist, W. M. Itano, and D. J. Wineland, "Laser cooling to the zero-point energy of motion," *Phys. Rev. Lett.* **62**, 403– (1989).

[22] P.-F. Cohadon, A. Heidmann, and M. Pinard, "Cooling of a mirror by radiation pressure," *Phys. Rev. Lett.* **83**, 3174–3177 (1999).

[23] O. Arcizet, P.-F. Cohadon, T. Briant, M. Pinard, and A. Heidmann, "Radiation-pressure cooling and optomechanical instability of a micromirror," *Nature* **444**, 71–74 (2006).

[24] S. Gigan, H. R. Böhm, M. Paternostro, F. Blaser, G. Langer, J. B. Hertzberg, K. C. Schwab, D. Bäuerle, M. Aspelmeyer, and A. Zeilinger, "Self-cooling of a micromirror by radiation pressure," *Nature* **444**, 67–70 (2006).

[25] A. Schliesser, P. Del'Haye, N. Nooshi, K. J. Vahala, and T. J. Kippenberg, "Radiation pressure cooling of a micromechanical oscillator using dynamical backaction," *Phys. Rev. Lett.* **97**, 243905 (2006).

[26] A. Abramovici, W. E. Althouse, R. W. P. Drever, Y. Grsel, S. Kawamura, F. J. Raab, D. Shoemaker, L. Sievers, R. E. Spero, K. S. Thorne, R. E. Vogt, R. Weiss, S. E. Whitcomb, and M. E. Zucker, "LIGO: The Laser Interferometer Gravitational-Wave Observatory," *Science* **256**, 325–333 (1992).

[27] D. Ramos, E. Gil-Santos, V. Pini, J. M. Llorens, M. Fernández-Regúlez, A. San Paulo, M. Calleja, and J. Tamayo, "Optomechanics with silicon nanowires by harnessing confined electromagnetic modes," *Nano Lett.* **12**, 932–937 (2012).

[28] P. J. Mohr, B. N. Taylor, and D. B. Newell, "CODATA recommended values of the fundamental physical constants: 2006," *Journal of Physical and Chemical Reference Data* **37**, 1187–1284 (2008).

[29] I. Wilson-Rae, N. Nooshi, W. Zwerger, and T. J. Kippenberg, "Theory of ground state cooling of a mechanical oscillator using dynamical back-action," *Phys. Rev. Lett.* **99**, 093901 (2007).

[30] J.-M. Courty, A. Heidmann, and M. Pinard, "Quantum limits of cold damping with optomechanical coupling," *Eur. Phys. J. D* **17**, 399–408 (2001).

[31] F. Marquardt, J. P. Chen, A. A. Clerk, and S. M. Girvin, "Quantum theory of cavity-assisted sideband cooling of mechanical motion," *Phys. Rev. Lett.* **99**, 093902 (2007).

[32] T. J. Kippenberg and K. J. Vahala, "Cavity opto-mechanics," *Opt. Express* **15**, 17172–17205 (2007).

[33] C. Genes, D. Vitali, P. Tombesi, S. Gigan, and M. Aspelmeyer, "Ground-state cooling of a micromechanical oscillator: comparing cold damping and cavity-assisted cooling schemes," *Phys. Rev. A* **77**, 033804 (2008).

[34] D. J. Wineland and W. M. Itano, "Laser cooling of atoms," *Phys. Rev. A* **20**, 1521–1540 (1979).

[35] A. Naik, O. Buu, M. D. LaHaye, A. D. Armour, A. A. Clerk, M. P. Blencowe, and K. C. Schwab, "Cooling a nanomechanical resonator with quantum back-action," *Nature* **443**, 193–196 (2006).

[36] D. Kleckner and D. Bouwmeester, "Sub-kelvin optical cooling of a micromechanical resonator," *Nature* **444**, 75–78 (2006).

[37] T. Corbitt, Y. Chen, E. Innerhofer, H. Müller-Ebhardt, D. Ottaway, H. Rehbein, D. Sigg, S. Whitcomb, C. Wipf, and N. Mavalvala, "An all-optical trap for a gram-scale mirror," *Phys. Rev. Lett.* **98**, 150802 (2007).

[38] M. Poggio, C. L. Degen, H. J. Mamin, and D. Rugar, "Feedback cooling of a cantilever's fundamental mode below 5 mK," *Phys. Rev. Lett.* **99**, 017201 (2007).

[39] K. R. Brown, J. Britton, R. J. Epstein, J. Chiaverini, D. Leibfried, and D. J. Wineland, "Passive cooling of a micromechanical oscillator with a resonant electric circuit," *Phys. Rev. Lett.* **99**, 137205 (2007).

[40] S. Gröblacher, S. Gigan, H. R. Böhm, A. Zeilinger, and M. Aspelmeyer, "Radiation-pressure self-cooling of a micromirror in a cryogenic environment," *Europhys. Lett.* **81**, 54003 (2008).

[41] A. Schliesser, R. Rivière, G. Anetsberger, O. Arcizet, and T. J. Kippenberg, "Resolved-sideband cooling of a micromechanical oscillator," *Nature Phys.* **4**, 415–419 (2008).

[42] J. D. Thompson, B. M. Zwickl, A. M. Jayich, F. Marquardt, S. M. Girvin, and J. G. E. Harris, "Strong dispersive coupling of a high-finesse cavity to a micromechanical membrane," *Nature* **452**, 72–75 (2008).

[43] A. Vinante, M. Bignotto, M. Bonaldi, M. Cerdonio, L. Conti, P. Falferi, N. Liguori, S. Longo, R. Mezzena, A. Ortolan, G. A. Prodi, F. Salemi, L. Taffarello, G. Vedovato, S. Vitale, and J.-P. Zendri, "Feedback cooling of the normal modes of a massive electromechanical system to submillikelvin temperature," *Phys. Rev. Lett.* **101**, 033601 (2008).

[44] J. D. Teufel, J. W. Harlow, C. A. Regal, and K. W. Lehnert, "Dynamical backaction of microwave fields on a nanomechanical oscillator," *Phys. Rev. Lett.* **101**, 197203 (2008).

[45] S. Gröblacher, J. B. Hertzberg, M. R. Vanner, S. Gigan, K. C. Schwab, and M. Aspelmeyer, "Demonstration of an ultracold micro-optomechanical oscillator in a cryogenic cavity," *Nature Phys.* **5**, 485–488 (2009).

[46] A. Schliesser, O. Arcizet, R. Rivière, G. Anetsberger, and T. J. Kippenberg, "Resolved-sideband cooling and position measurement of a micromechanical oscillator close to the Heisenberg uncertainty limit," *Nature Phys.* **5**, 509–514 (2009).

[47] Y.-S. Park and H. Wang, "Resolved-sideband and cryogenic cooling of an optomechanical resonator," *Nature Phys.* **5**, 489–493 (2009).

[48] A. D. O'Connell, M. Hofheinz, M. Ansmann, R. C. Bialczak, M. Lenander, E. Lucero, M. Neeley, D. Sank, H. Wang, M. Weides, J. Wenner, J. M. Martinis, and A. N. Cleland, "Quantum ground state and single-phonon control of a mechanical resonator," *Nature* **464**, 697–703 (2010).

[49] T. Rocheleau, T. Ndukum, C. Macklin, J. B. Hertzberg, A. A. Clerk, and K. C. Schwab, "Preparation and detection of a mechanical resonator near the ground state of motion," *Nature* **463**, 72–75 (2010).

[50] R. Rivière, S. Deléglise, S. Weis, E. Gavartin, O. Arcizet, A. Schliesser, and T. J. Kippenberg, "Optomechanical sideband cooling of a micromechanical oscillator close to the quantum ground state," *Phys. Rev. A* **83**, 063835 (2011).

[51] J. D. Teufel, T. Donner, D. Li, J. W. Harlow, M. S. Allman, K. Cicak, A. J. Sirois, J. D. Whittaker, K. W. Lehnert, and R. W. Simmonds, "Sideband cooling of micromechanical motion to the quantum ground state," *Nature* **475**, 359–363 (2011).

[52] J. Chan, T. P. M. Alegre, A. H. Safavi-Naeini, J. T. Hill, A. Krause, S. Gröblacher, M. Aspelmeyer, and O. Painter, "Laser cooling of a nanomechanical oscillator into its quantum ground state," *Nature* **478**, 89–92 (2011).

[53] E. Verhagen, S. Deléglise, S. Weis, A. Schliesser, and T. J. Kippenberg, "Quantum-coherent coupling of a mechanical oscillator to an optical cavity mode," (2011).

[54] C. Genes, A. Mari, D. Vitali, and P. Tombesi, "Quantum effects in optomechanical systems," *Adv. At. Mol. Opt. Phys.* **57**, 33–86 (2009).

[55] M. Aspelmeyer, S. Gröblacher, K. Hammerer, and N. Kiesel, "Quantum optomechanics—throwing a glance," *J. Opt. Soc. Am. B* **27**, A189–A197 (2010).

[56] J. Chan, M. Eichenfield, R. Camacho, and O. Painter, "Optical and mechanical design of a "zipper" photonic crystal optomechanical cavity," *Opt. Express* **17**, 3802–3817 (2009).

[57] M. Eichenfield, R. Camacho, J. Chan, K. J. Vahala, and O. Painter, "A picogram- and nanometre-scale photonic-crystal optomechanical cavity," *Nature* **459**, 550–555 (2009).

[58] A. G. Krause, M. Winger, T. D. Blasius, Q. Lin, and O. Painter, "A microchip optomechanical accelerometer," *arXiv:1203.5730* (2012).

[59] M. Eichenfield, J. Chan, R. M. Camacho, K. J. Vahala, and O. Painter, "Optomechanical crystals," *Nature* **462**, 78–82 (2009).

[60] M. Eichenfield, J. Chan, A. H. Safavi-Naeini, K. J. Vahala, and O. Painter, "Modeling dispersive coupling and losses of localized optical and mechanical modes in optomechanical crystals," *Opt. Express* **17**, 20078–20098 (2009).

[61] M. Trigo, A. Bruchhausen, A. Fainstein, B. Jusserand, and V. Thierry-Mieg, "Confinement of acoustical vibrations in a semiconductor planar phonon cavity," *Phys. Rev. Lett.* **89**, 227402 (2002).

[62] A. H. Safavi-Naeini and O. Painter, "Design of optomechanical cavities and waveguides on a simultaneous bandgap phononic-photonic crystal slab," *Opt. Express* **18**, 14926–14943 (2010).

[63] T. P. M. Alegre, A. Safavi-Naeini, M. Winger, and O. Painter, "Quasi-two-dimensional optomechanical crystals with a complete phononic bandgap," *Opt. Express* **19**, 5658–5669 (2011).

[64] S. Johnson, "MIT Photonic-Bands 1.4.2," (2003).
http://ab-initio.mit.edu/wiki/

[65] "COMSOL Multiphysics 3.5a," (2008).
http://www.comsol.com/

[66] M. Borselli, T. J. Johnson, and O. Painter, "Measuring the role of surface chemistry in silicon microphotonics," *App. Phys. Lett.* **88**, 131114 (2006).

[67] M. Borselli, T. J. Johnson, and O. Painter, "Accurate measurement of scattering and absorption loss in microphotonic devices," *Opt. Lett.* **32**, 2954–2956 (2007).

[68] P. Barclay, K. Srinivasan, and O. Painter, "Nonlinear response of silicon photonic crystal microresonators excited via an integrated waveguide and fiber taper," *Opt. Express* **13**, 801–820 (2005).

[69] C. P. Michael, M. Borselli, T. J. Johnson, C. Chrystal, and O. Painter, "An optical fiber-taper probe for wafer-scale microphotonic device characterization," *Opt. Express* **15**, 4745–4752 (2007).

[70] K. Srinivasan and O. Painter, "Optical fiber taper coupling and high-resolution wavelength tuning of microdisk resonators at cryogenic temperatures," *App. Phys. Lett.* **90**, 031114 (2007).

[71] R. Ghobadi, A. R. Bahrampour, and C. Simon, "Quantum optomechanics in the bistable regime," *Phys. Rev. A* **84**, 033846 (2011).

[72] M. Bhattacharya and P. Meystre, "Trapping and cooling a mirror to its quantum mechanical ground state," *Phys. Rev. Lett.* **99**, 073601– (2007).

[73] A. H. Safavi-Naeini and O. Painter, "Proposal for an optomechanical traveling wave phonon-photon translator," *New J. Phys.* **13**, 013017 (2011).

[74] H.-A. Bachor and T. C. Ralph, *A Guide to Experiments in Quantum Optics* (Wiley-VCH, 2004), 2nd edition.

[75] X. Sun, K. Y. Fong, C. Xiong, W. H. P. Pernice, and H. X. Tang, "GHz optomechanical resonators with high mechanical Q factor in air," *Opt. Express* **19**, 22316–22321 (2011).

[76] A. H. Safavi-Naeini, T. P. M. Alegre, M. Winger, and O. Painter, "Optomechanics in an ultrahigh-Q slotted 2D photonic crystal cavity," *Appl. Phys. Lett.* **97**, 181106 (2010).

[77] S. G. Johnson, M. Ibanescu, M. A. Skorobogatiy, O. Weisberg, J. D. Joannopoulos, and Y. Fink, "Perturbation theory for Maxwell's equations with shifting material boundaries," *Phys. Rev. E* **65**, 066611– (2002).

[78] D. K. Biegelsen, "Photoelastic tensor of silicon and the volume dependence of the average gap," *Phys. Rev. Lett.* **32**, 1196–1199 (1974).

[79] J. D. Joannopoulos, S. G. Johnson, J. N. Winn, and R. D. Meade, *Photonic Crystals: Molding the Flow of Light* (Princeton University Press, 2008), 2nd edition.

[80] K. Sakoda, *Optical Properties of Photonic Crystals* (Springer, 2005).

[81] R. Shankar, *Principles of Quantum Mechanics* (Springer, 1994), 2nd edition.

[82] R. E. Camley, B. Djafari-Rouhani, L. Dobrzynski, and A. A. Maradudin, "Transverse elastic waves in periodically layered infinite and semi-infinite media," *Phys. Rev. B* **27**, 7318–7329 (1983).

[83] M. S. Kushwaha, P. Halevi, L. Dobrzynski, and B. Djafari-Rouhani, "Acoustic band structure of periodic elastic composites," *Phys. Rev. Lett.* **71**, 2022–2025 (1993).

[84] Z.-G. Huang, *Acoustic Waves—From Microdevices to Helioseismology* (InTech, 2011), chap. 1, pp. 4–20.

[85] R. F. Harrington, *Time-Harmonic Electromagnetic Fields* (IEEE Press, 1961).

[86] P. Y. Amnon Yariv, *Optical Waves in Crystals* (Wiley-Interscience, 1983).

[87] D. K. Biegelsen, "Frequency dependence of the photoelastic coefficients of silicon," *Phys. Rev. B* **12**, 2427–2431 (1975).

[88] MathWorks, "MATLAB 2010b," (2010). http://www.mathworks.com/products/matlab/

[89] P. B. Deotare, M. W. McCutcheon, I. W. Frank, M. Khan, and M. Lončar, "High quality factor photonic crystal nanobeam cavities," *Applied Physics Letters* **94**, 121106 (2009).

[90] Y. Akahane, T. Asano, B.-S. Song, and S. Noda, "High-Q photonic nanocavity in a two-dimensional photonic crystal," *Nature* **425**, 944–947 (2003).

[91] J. A. Nelder and R. Mead, "A simplex method for function minimization," *The Computer Journal* **7**, 308–313 (1965).

[92] J. C. Lagarias, J. A. Reeds, M. H. Wright, and P. E. Wright, "Convergence properties of the Nelder-Mead simplex method in low dimensions," *SIAM Journal of Optimization* **9**, 112–147 (1998).

[93] P. Mohanty, D. A. Harrington, K. L. Ekinci, Y. T. Yang, M. J. Murphy, and M. L. Roukes, "Intrinsic dissipation in high-frequency micromechanical resonators," *Phys. Rev. B* **66**, 085416 (2002).

[94] A. Akhieser, *J. Phys (Moscow)* **1**, 277 (1939).

[95] L. Landau and G. Rumer, "Absorption of sound in solids," *Phys. Z. Sowjetunion* **11**, 18 (1937).

[96] R. Tabrizian, M. Rais-Zadeh, and F. Ayazi, "Effect of phonon interactions on limiting the f.Q product of micromechanical resonators," in *Solid-State Sensors, Actuators and Microsystems Conference, 2009. TRANSDUCERS 2009. International* pp. 2131–2134 (2009).

[97] T. O. Woodruff and H. Ehrenreich, "Absorption of sound in insulators," *Phys. Rev.* **123**, 1553–1559 (1961).

[98] J. Philip and M. A. Breazeale, "Third-order elastic constants and Grüneisen parameters of silicon and germanium between 3 and 300 °K," *J. Appl. Phys.* **54**, 752–757 (1983).

[99] R. Lifshitz and M. L. Roukes, "Thermoelastic damping in micro- and nanomechanical systems," *Phys. Rev. B* **61**, 5600–5609 (2000).

[100] A. Duwel, R. N. Candler, T. W. Kenny, and M. Varghese, "Engineering MEMS resonators with low thermoelastic damping," *J. Microelectromech. S.* **15**, 1437–1445 (2006).

[101] J. Chan, A. H. Safavi-Naeini, J. T. Hill, S. Meenehan, M. Eichenfield, and O. Painter, "Designing high-Q nanobeam cavities with large optomechanical coupling," In preparation.

[102] D. B. Fenner, D. K. Biegelsen, and R. D. Bringans, "Silicon surface passivation by hydrogen termination: A comparative study of preparation methods," *Journal of Applied Physics* **66**, 419–424 (1989).

[103] H. Kobayashi, Y. Yamashita, Y. Nakato, T. Komeda, and Y. Nishioka, "Interface states at ultrathin oxide/Si(111) interfaces obtained from x-ray photoelectron spectroscopy measurements under biases," *Applied Physics Letters* **69**, 2276–2278 (1996).

[104] I. M. P. Aarts, B. Hoex, A. H. M. Smets, R. Engeln, W. M. M. Kessels, and M. C. M. van de Sanden, "Direct and highly sensitive measurement of defect-related absorption in amorphous silicon thin films by cavity ringdown spectroscopy," *Applied Physics Letters* **84**, 3079–3081 (2004).

[105] T. K. Liang and H. K. Tsang, "Role of free carriers from two-photon absorption in Raman amplification in silicon-on-insulator waveguides," *Applied Physics Letters* **84**, 2745–2747 (2004).

[106] R. Jones, H. Rong, A. Liu, A. Fang, M. Paniccia, D. Hak, and O. Cohen, "Net continuous wave optical gain in a low loss silicon-on-insulator waveguide by stimulated Raman scattering," *Opt. Express* **13**, 519–525 (2005).

[107] Y. Liu and H. K. Tsang, "Time dependent density of free carriers generated by two photon absorption in silicon waveguides," *Appl. Phys. Lett.* **90**, 211105–3 (2007).

[108] A. C. Turner-Foster, M. A. Foster, J. S. Levy, C. B. Poitras, R. Salem, A. L. Gaeta, and M. Lipson, "Ultrashort free-carrier lifetime in low-loss silicon nanowaveguides," *Opt. Express* **18**, 3582–3591 (2010).

[109] T. J. Johnson, *Silicon Microdisk Resonators for Nonlinear Optics and Dynamics*, Ph.D. thesis, California Institute of Technology (2009).

[110] M. Morita, T. Ohmi, E. Hasegawa, M. Kawakami, and M. Ohwada, "Growth of native oxide on a silicon surface," *Journal of Applied Physics* **68**, 1272–1281 (1990).

[111] S. Hunklinger, "Phonons in amorphous materials," *J. Phys. Colloques* **43**, 461–474 (1982).

[112] R. O. Pohl, X. Liu, and E. Thompson, "Low-temperature thermal conductivity and acoustic attenuation in amorphous solids," *Rev. Mod. Phys.* **74**, 991–1013 (2002).

[113] R. Vacher, E. Courtens, and M. Foret, "Anharmonic versus relaxational sound damping in glasses. II. Vitreous silica," *Phys. Rev. B* **72**, 214205 (2005).

[114] A. Yagi and S. Kawaji, "Effects of nitrogen annealing on electron scatterings in Si–SiO_2 interface," *Solid-State Electronics* **22**, 261–263 (1979).

[115] H. Wong and Y. C. Cheng, "A new growth model of thin silicon oxide in dry oxygen," *Journal of Applied Physics* **64**, 893–897 (1988).

[116] A. D. Yablon, *Optical Fiber Fusion Splicing* (Springer, 2005).

[117] A. H. Safavi-Naeini, T. P. M. Alegre, J. Chan, M. Eichenfield, M. Winger, Q. Lin, J. T. Hill, D. Chang, and O. Painter, "Electromagnetically induced transparency and slow light with optomechanics," *Nature* **472**, 69–73 (2011).

[118] S. Weis, R. Rivière, S. Deléglise, E. Gavartin, O. Arcizet, A. Schliesser, and T. J. Kippenberg, "Optomechanically induced transparency," *Science* **330**, 1520–1523 (2010).

[119] B. J. Frey, D. B. Leviton, and T. J. Madison, "Temperature-dependent refractive index of silicon and germanium," in *Proc. SPIE* **6273**, 62732J (2006).

[120] A. H. Safavi-Naeini, J. Chan, J. T. Hill, S. Gröblacher, H. Miao, F. Khalili, Y. Chen, M. Aspelmeyer, and Oskar, "Laser phase noise in sideband-resolved optomechanical cooling and thermometry," In preparation.

[121] E. Desurvire, D. Bayart, B. Desthieux, and S. Bigo, *Erbium-Doped Fiber Amplifiers, Device and System Developments* (Wiley-Interscience, 2002).

[122] A. A. Clerk, M. H. Devoret, S. M. Girvin, F. Marquardt, and R. J. Schoelkopf, "Introduction to quantum noise, measurement, and amplification," *Rev. Mod. Phys.* **82**, 1155–1208 (2010).

[123] D. Vitali, S. Gigan, A. Ferreira, H. R. Böhm, P. Tombesi, A. Guerreiro, V. Vedral, A. Zeilinger, and M. Aspelmeyer, "Optomechanical entanglement between a movable mirror and a cavity field," *Phys. Rev. Lett.* **98**, 030405 (2007).

[124] U. Akram, N. Kiesel, M. Aspelmeyer, and G. J. Milburn, "Single-photon optomechanics in the strong coupling regime," *New J. Phys.* **12**, 083030 (2010).

[125] K. Stannigel, P. Rabl, A. S. Sørensen, P. Zoller, and M. D. Lukin, "Optomechanical transducers for long-distance quantum communication," *Phys. Rev. Lett.* **105**, 220501 (2010).

[126] D. Chang, A. H. Safavi-Naeini, M. Hafezi, and O. Painter, "Slowing and stopping light using an optomechanical crystal array," *New J. Phys.* **13**, 023003 (2011).

[127] P. Rabl, "Photon blockade effect in optomechanical systems," *Phys. Rev. Lett.* **107**, 063601 (2011).

[128] D. Marcuse, "Mode conversion caused by surface imperfections of a dielectric slab waveguide," *Bell System Technical Journal* **48**, 3187 (1969).

[129] M. L. Dakss, L. Kuhn, P. F. Heidrich, and B. A. Scott, "Grating coupler for efficient excitation of optical guided waves in thin films," *Appl. Phys. Lett.* **16**, 523–525 (1970).

[130] D. Taillaert, P. Bienstman, and R. Baets, "Compact efficient broadband grating coupler for silicon-on-insulator waveguides," *Opt. Lett.* **29**, 2749–2751 (2004).

[131] D. Taillaert, F. V. Laere, M. Ayre, W. Bogaerts, D. V. Thourhout, P. Bienstman, and R. Baets, "Grating couplers for coupling between optical fibers and nanophotonic waveguides," *Japanese Journal of Applied Physics* **45**, 6071–6077 (2006).

[132] G. Roelkens, D. Vermeulen, D. Van Thourhout, R. Baets, S. Brision, P. Lyan, P. Gautier, and J.-M. Fedeli, "High efficiency diffractive grating couplers for interfacing a single mode optical fiber with a nanophotonic silicon-on-insulator waveguide circuit," *Appl. Phys. Lett.* **92**, 131101–131103 (2008).

[133] D. Vermeulen, S. Selvaraja, P. Verheyen, G. Lepage, W. Bogaerts, P. Absil, D. Van Thourhout, and G. Roelkens, "High-efficiency fiber-to-chip grating couplers realized using an advanced CMOS-compatible Silicon-On-Insulator platform," *Opt. Express* **18**, 18278–18283 (2010).

[134] Y. Tang, Z. Wang, L. Wosinski, U. Westergren, and S. He, "Highly efficient nonuniform grating coupler for silicon-on-insulator nanophotonic circuits," *Opt. Lett.* **35**, 1290–1292 (2010).

[135] M. Antelius, K. B. Gylfason, and H. Sohlström, "An apodized SOI waveguide-to-fiber surface grating coupler for single lithography silicon photonics," *Opt. Express* **19**, 3592–3598 (2011).

[136] F. Van Laere, G. Roelkens, M. Ayre, J. Schrauwen, D. Taillaert, D. Van Thourhout, T. F. Krauss, and R. Baets, "Compact and highly efficient grating couplers between optical fiber and nanophotonic waveguides," *J. Lightwave Technol.* **25**, 151–156 (2007).

[137] E. Dulkeith, S. J. McNab, and Y. A. Vlasov, "Mapping the optical properties of slab-type two-dimensional photonic crystal waveguides," *Phys. Rev. B* **72**, 115102– (2005).

[138] B. E. A. Saleh and M. C. Teich, *Fundamentals of Photonics* (John Wiley and Sons, 1991).

[139] U. Gavish, Y. Levinson, and Y. Imry, "Detection of quantum noise," *Phys. Rev. B* **62**, R10637–R10640 (2000).

[140] A. H. Safavi-Naeini, J. Chan, J. T. Hill, T. P. M. Alegre, A. Krause, and O. Painter, "Observation of quantum motion of a nanomechanical resonator," *Phys. Rev. Lett.* **108**, 033602–(2012).

[141] R. N. Bracewell, *The Fourier Transform and Its Applications* (McGraw-Hill, 2000), 3rd edition.

[142] G. B. Arfken and H. J. Weber, *Mathematical Methods for Physicists* (Academic Press, 2005), 6th edition.

[143] P. Helnwein, "Some remarks on the compressed matrix representation of symmetric second-order and fourth-order tensors," *Computer Methods in Applied Mechanics and Engineering* **190**, 2753–2770 (2001).

[144] P. Langevin, "Sur la théorie du mouvement brownien," *C. R. Acad. Sci.* **146**, 530–533 (1908).

[145] H. B. Callen and T. A. Welton, "Irreversibility and generalized noise," *Phys. Rev.* **83**, 34–40 (1951).

[146] C. W. Gardiner and M. J. Collett, "Input and output in damped quantum systems: Quantum stochastic differential equations and the master equation," *Phys. Rev. A* **31**, 3761–3774 (1985).

[147] C. W. Gardiner and P. Zoller, *Quantum Noise: A Handbook of Markovian and Non-Markovian Quantum Stochastic Methods with Applications to Quantum Optics* (Springer, 2004).

[148] M. O. Scully and M. S. Zubairy, *Quantum Optics* (Cambridge University Press, 1997).

[149] D. F. Walls and G. J. Milburn, *Quantum Optics* (Springer, 2008).

[150] L. Mandel and E. Wolf, *Optical Coherence and Quantum Optics* (Cambridge University Press, 1995).

[151] MathWorks, "Instrument Control Toolbox," (2010). http://www.mathworks.com/products/instrument/

[152] C. A. Swenson, "Recommended values for the thermal expansivity of silicon from 0 to 1000 K," *J. Phys. Chem. Ref. Data* **12**, 179–182 (1983).

[153] C. J. Glassbrenner and G. A. Slack, "Thermal conductivity of silicon and germanium from 3°K to the melting point," *Phys. Rev.* **134**, A1058–A1069 (1964).

[154] S. D. Lambade, G. G. Sahasrabudhe, and S. Rajagopalan, "Temperature dependence of acoustic attenuation in silicon," *Phys. Rev. B* **51**, 15861–15866 (1995).

[155] N. Pearlman and P. H. Keesom, "The atomic heat of silicon below 100°K," *Phys. Rev.* **88**, 398–405 (1952).